

The Pennsylvania State University
The Graduate School
College of Earth and Mineral Sciences

**MECHANISMS OF SINTERING AND SECOND PHASE
FORMATION IN BAYER ALUMINA**

A Dissertation in
Materials Science and Engineering
by
Tobias Frueh

© 2017 Tobias Frueh

Submitted in Partial Fulfillment
of the Requirements
for the Degree of

Doctor of Philosophy

December 2017

The dissertation of Tobias Frueh was reviewed and approved* by the following:

Gary L. Messing

Distinguished Professor of Ceramic Science and Engineering
Dissertation Advisor, Chair of Committee

James H. Adair

Professor of Materials Science and Engineering, Biomedical Engineering and
Pharmacology

John R. Hellmann

Professor of Materials Science and Engineering
Associate Dean for Graduate Education and Research

Douglas E. Wolfe

Associate Professor of Materials Science and Engineering
Department Head, Advanced Coatings at the Applied Research Laboratory
Senior Scientist

Charles E. Compson

Global Technical Director, CPO
Almatis, Inc.
Special Member

*Signatures are on file in the Graduate School.

Abstract

The vast majority of industrial Al_2O_3 applications use powders derived from Bayer feedstocks with purity levels of 99.0 - 99.9%. This dissertation explores how the extrinsic powder chemistry of Bayer alumina influences densification, microstructure evolution, and fundamental sintering mechanisms.

To determine how grain-boundary composition affects the sintering of MgO-free Bayer Al_2O_3 , dilatometry and sintering kinetics experiments of samples with Na_2O and SiO_2 concentrations up to 1029 ppm 603 ppm, respectively, were performed. It was shown that Na_2O and SiO_2 form a nanometer thick siliceous grain boundary film. The estimated viscosities (20 - 400 Pa·s) indicate that diffusion greatly depends on the composition of the liquid grain-boundary phase, and densification strongly depends on the $\text{Na}_2\text{O}/\text{SiO}_2$ ratio in the samples. For low $\text{Na}_2\text{O}/\text{SiO}_2$ ratios, densification of Bayer Al_2O_3 at 1525°C is controlled by diffusion of Al^{3+} through the grain-boundary liquid, whereas for high $\text{Na}_2\text{O}/\text{SiO}_2$ ratios, densification can be governed by either the interface reaction of Al_2O_3 or diffusion of Al^{3+} . Increasing Na_2O in SiO_2 -doped samples increases diffusion of Al^{3+} and Al_2O_3 solubility in the liquid, and thus densification increases by 1-2.5%. Based on these findings, it is concluded that Bayer Al_2O_3 densification is controlled by the Na_2O to SiO_2 ratio.

The stages at which MgO influences densification of Al_2O_3 were identified by comparing dilatometry measurements and sintering kinetics of MgO-free and 380 ppm MgO-doped Bayer Al_2O_3 powder. Using high-resolution TEM it was shown that MgO reduces the grain boundary thickness during final stage sintering. It was shown by EDS that MgO increases the solubility of SiO_2 in Al_2O_3 grains near the boundaries. First-principles DFT calculations demonstrated that the co-dissolution of MgO and SiO_2 in Al_2O_3 is thermodynamically favored over the dissolution of MgO or SiO_2 individually in Al_2O_3 . For the first time, it was experimentally demonstrated that removal of SiO_2 from the grain boundary during final stage sintering is a key process by which MgO enhances the sintering of Al_2O_3 .

A physical model that describes the dynamic development of grain boundary chemistry and thickness from initial to final stage sintering as a function of chemical and physical powder parameters was developed. The liquid glass phase initially accumulates in the particle contacts due to capillarity and during densification the glass phase distribution changes due to the formation of grain boundaries and grain growth, leading to a dynamic change in grain boundary thickness during densification. Grain boundary thicknesses measured from high-resolution TEM images agree well with predicted film thicknesses. The model shows that the grain boundary thickness is determined by either the concentration of the glass phase in the sample or by an equilibrium film thickness, which is controlled by a balance between attractive and repulsive interparticle forces. Variations in powder chemistry, such as changing the $\text{Na}_2\text{O}/\text{SiO}_2$ ratio or changing the MgO concentration, can affect the grain boundary thickness by influencing the interparticle force balance or by changing the amount of glass phase in the grain boundaries.

The formation of $\beta\text{-Al}_2\text{O}_3$ ($\text{Na}_2\text{O}\cdot11\text{Al}_2\text{O}_3$) is sometimes observed during sintering of Bayer Al_2O_3 , and the conditions and mechanisms of formation were investigated. Formation kinetics showed that the majority of $\beta\text{-Al}_2\text{O}_3$ grains form between 0 and 1 hour at 1525°C , at densities $>90\%$. The amount of $\beta\text{-Al}_2\text{O}_3$ increases with increasing Na_2O and MgO concentrations, and decreases with increasing SiO_2 concentration. SiO_2 increases the solubility of Na_2O in the grain boundaries by forming a glassy film, and thereby counteracts the formation of $\beta\text{-Al}_2\text{O}_3$. At final sintering stage SiO_2 is removed from the grain boundaries because SiO_2 and MgO form a solid solution in $\alpha\text{-Al}_2\text{O}_3$, which leads to the supersaturation of grain boundaries and the nucleation and growth of $\beta\text{-Al}_2\text{O}_3$.

The Master Sintering Curve (MSC) approach and the factors affecting its accuracy were explored for analyzing the complete sintering profile of Bayer Al_2O_3 . MSC analysis is sensitive to shrinkage anisotropy, which can be accounted for by directional shrinkage measurements, and to powder chemistry and forming technique effects that result in mechanistic changes that cannot be sufficiently described by MSC analysis. It is concluded that Q should not be interpreted as the sintering activation energy, or used to interpret mechanistic differences between powders since Q includes several mechanisms that influence densification throughout the sintering cycle. Despite these limitations, the MSC approach is a useful and practical tool for predicting the effects of thermal load (i.e. time and temperature) on densification of a specific powder and forming process.

Table of Contents

List of Figures	viii
List of Tables	xiv
Acknowledgments	xv
Chapter 1	
Introduction	1
1.1 Motivation	1
1.2 Sintering of Ceramics	2
1.3 Effects of Impurities and Dopants on the Sintering of Al_2O_3	4
1.3.1 MgO in Ultrahigh Purity Al_2O_3	4
1.3.2 Effects of Impurities during sintering of Al_2O_3	5
1.3.3 Effects of MgO on Liquid Phase Sintering of Al_2O_3	6
1.3.4 Grain Boundaries During Sintering of Al_2O_3	7
1.4 Sintering of Bayer Alumina	10
1.4.1 The Bayer Process	10
1.4.2 Influence of Na_2O and SiO_2 on the Sintering Behavior of Al_2O_3	11
Chapter 2	
The Effects of Na_2O and SiO_2 on Liquid Phase Sintering of Bayer Al_2O_3	17
2.1 Introduction	17
2.2 Experimental	18
2.3 Results	19
2.3.1 Effects of Na_2O -doping	19
2.3.2 Effects of $\text{Na}_2\text{O}/\text{SiO}_2$ co-doping	20
2.4 Discussion	21
2.5 Summary	26

Chapter 3	
Powder Chemistry Effects on the Sintering Behavior of MgO-doped Bayer Alumina	39
3.1 Introduction	39
3.2 Experimental	41
3.3 Computational Methodology	42
3.4 Sintering and Microstructure Analysis	44
3.5 Mechanistic Interpretation	47
3.6 Summary and Conclusion	53
Chapter 4	
Dynamic development of nanometer scale grain boundaries during liquid phase sintering	69
4.1 Introduction	69
4.2 Experiment	71
4.3 Grain boundary thickness in MgO-free alumina	72
4.4 The equilibrium film thickness model	74
4.5 Calculation of the theoretical Equilibrium Film Thicknesses	75
4.6 High-resolution TEM	79
4.7 The effect of changes in powder chemistry	80
4.7.1 Na ₂ O/SiO ₂ ratio	80
4.7.2 MgO-doped Bayer alumina	81
4.8 Conclusion	81
Chapter 5	
Second phase formation in Bayer alumina	95
5.1 Introduction	95
5.2 Experimental	96
5.3 Results	97
5.4 Interpretation and mechanisms of β -Al ₂ O ₃ formation	99
5.5 Summary	102
Chapter 6	
A Critique of the Master Sintering Curve Analysis of Sintering Processes	116
6.1 Introduction	116
6.2 Experimental Procedure	119
6.3 Results and Discussion	121
6.3.1 The effect of forming on Q	121
6.3.2 MSC at high densities	123

6.3.3	Quantification of the MSC shape	124
6.3.4	Influence of powder chemistry	125
6.3.5	Limitations of the MSC analysis	125
6.3.6	Practical use of the MSC analysis	127
6.4	Summary	128
Chapter 7		
Summary and Future Work		141
7.1	Summary	141
7.1.1	The Effects of Na ₂ O and SiO ₂ on Liquid Phase Sintering of Bayer Al ₂ O ₃	141
7.1.2	Powder Chemistry Effects on the Sintering of MgO-doped Specialty Al ₂ O ₃	142
7.1.3	Dynamic development of nanometer scale grain boundaries during liquid phase sintering	143
7.1.4	Second phase formation in Bayer alumina	144
7.1.5	A Critique of Master Sintering Curve Analysis of Sintering Processes	145
7.2	Future work	145
Bibliography		148

List of Figures

1.1 Segregation and precipitation map of MgO-doped alumina based on the results in the literature [1]	14
1.2 SIMS maps of Al ₂ O ₃ doped with 500 ppm MgO (a) and 1000 ppm SiO ₂ (b). Samples were sintered for 8 h at 1650°C [2].	15
1.3 SIMS maps of Al ₂ O ₃ co-doped with 500 ppm MgO and 1000 ppm SiO ₂ and sintered at 1650°C for 8h. (a) shows the distribution of SiO ₂ , (b) the distribution of MgO in the same samples [2].	16
2.1 SEM image of as-received chemically purified Bayer Al ₂ O ₃ powder used in this study.	30
2.2 Dilatometer curves of as-received and singly Na ₂ O-doped samples heated at 10°C/min to 1525°C.	31
2.3 Densification kinetics of Bayer Al ₂ O ₃ doped with different Na ₂ O concentrations and sintered at 1525°C.	32
2.4 Microstructures of as-received and singly 529 ppm Na ₂ O doped samples after 30 min, 3 h and 8 h at 1525°C.	33
2.5 Dilatometer curves of as-received, singly SiO ₂ -doped, and Na ₂ O/SiO ₂ co-doped Bayer Al ₂ O ₃ heated at 10°C/min to 1525°C.	34
2.6 Densification kinetics of Bayer Al ₂ O ₃ doped with different concentrations of Na ₂ O and SiO ₂ at 1525°C.	35
2.7 Microstructures of Bayer Al ₂ O ₃ doped with a) 603 ppm SiO ₂ and b) 529 ppm Na ₂ O and 603 ppm SiO ₂ after heating at 1525°C for 8h.	36
2.8 Micrographs of a sample doped with 1029 ppm Na ₂ O after sintering at 1525°C for 3 h. The micrographs were recorded using a) a secondary electron detector and b) a backscattered electron detector. The arrows point at the platelet shaped β -alumina grains that form in samples doped with Na ₂ O. The samples were not thermally etched.	37

2.9	Liquidus projection of the Al_2O_3 - SiO_2 - Na_2O ternary phase diagram. The red solid lines are isoplethal cuts representing the samples investigated in this study. The red dashed line is the 1525°C isotherm where α - Al_2O_3 and liquid are in equilibrium. The blue dash-dot line and green dotted line are eutectic lines at which α - Al_2O_3 and liquid is in equilibrium with β - Al_2O_3 or mullite, respectively.	38
3.1	SEM image of 380 ppm MgO-doped Bayer alumina powder used in this work.	57
3.2	Dilatometer curves of a) 380 ppm MgO-doped and b) MgO-free [3] Bayer alumina samples with different $\text{Na}_2\text{O}/\text{SiO}_2$ levels heated at 10°C/min to 1525°C.	58
3.3	Densification kinetics of Bayer processed alumina containing different amounts Na_2O and SiO_2 and a) 380 ppm MgO sintered at 1450°C, b) 380 ppm MgO sintered at 1525°C, and c) 2 ppm MgO sintered at 1525°C [3].	59
3.4	Microstructures of 380 ppm MgO-doped Bayer alumina samples with different Na_2O and SiO_2 concentrations sintered at 1525°C for 8 h.	60
3.5	Sintering trajectories (grain size vs. relative density) for 380 ppm MgO-doped Bayer alumina samples with different Na_2O and SiO_2 concentrations.	61
3.6	Grain boundary of a sample containing 529 ppm Na_2O , 603 ppm SiO_2 , and 2 ppm MgO after 3 h at 1525°C.	62
3.7	Grain boundaries of samples containing 560 ppm Na_2O , 582 ppm SiO_2 , and 380 ppm MgO after a) 0 h and b) 3 h at 1525°C.	63
3.8	EDS of grain boundaries of samples containing 560 ppm Na_2O , 582 ppm SiO_2 , and 380 ppm MgO after a) 0 h and b) 3 h at 1525°C showing the Si distribution. After 0 h Si shows a stronger segregation to the grain boundaries than after 3 h.	64
3.9	EDS line scan across a grain boundary of a sample containing 560 ppm Na_2O , 582 ppm SiO_2 , and 380 ppm MgO after sintering at 1525°C for a) 0 h and b) 3 h.	65
3.10	Comparison of the formation energy of α - Al_2O_3 with an Mg-cluster (E_{Form}^{Mg}), Si-cluster (E_{Form}^{Si}) and Mg+Si-cluster (E_{Form}^{Mg+Si}) as a function of temperature. The formation energy difference (ΔE_{Form}) between the structures was calculated from Eq. 3.9 to compare the formation energy values and show that it is energetically favorable to form Mg+Si-clusters over Si-clusters and Mg-clusters.	66

3.11 EDS maps of different oxides in 380 ppm MgO-doped Bayer alumina samples after sintering at 1525°C for a-d) 0 h and e-h) 3 h. a) and e) show the distribution of Mg, b) and f) show the distribution of Fe, c) and g) show the distribution of Na, and d) and h) show the distribution of Ca.	67
3.12 Na ₂ O concentration (ICP measurements) of 380 ppm MgO-doped Bayer alumina samples with 560 ppm Na ₂ O as a) function of sintering temperature and b) as a function of sintering time at 1525°C.	68
4.1 Increase in concentration of liquid phase as a function of temperature for MgO-free powder samples with 529 ppm Na ₂ O and different SiO ₂ concentrations.	83
4.2 Relative density as a function of temperature and hold time determined from dilatometry for MgO-free powder samples with 529 ppm Na ₂ O and different SiO ₂ concentrations.	84
4.3 Liquid phase concentration as a function of relative density for MgO-free powder samples with 529 ppm Na ₂ O and different SiO ₂ concentrations.	85
4.4 Grain size - density trajectories as a function of Na ₂ O and SiO ₂ concentration for MgO-free alumina.	86
4.5 Change in Na/Al ion ratio in the liquid phase during sintering of samples with Na ₂ O/SiO ₂ ratios > 0.5.	87
4.6 Development of the electrostatic potential as a function of relative density. For MgO-free powder samples with 529 ppm Na ₂ O and different SiO ₂ concentrations.	88
4.7 Contributions to the equilibrium film thickness as a function of film thickness for MgO-free powder samples with 529/603 ppm Na ₂ O/SiO ₂ at a relative density of 93%.	89
4.8 Calculated equilibrium film thickness for MgO-free powder samples at different chemistries as a function of relative density.	90
4.9 Calculated grain boundary thicknesses as a function of relative density for MgO-free powder samples. The trajectories labeled with 529/603 ppm Na ₂ O/SiO ₂ , 529/203 ppm Na ₂ O/SiO ₂ , and 529 ppm Na ₂ O/SiO ₂ were calculated based on the liquid phase concentration and sintering stage. The equilibrium film thickness was calculated based on Clarke's model. The calculated grain boundary thicknesses are compared to measured grain boundary thicknesses (data points a: 1000/1000 ppm Na ₂ O/SiO ₂ , b) 529/603 ppm Na ₂ O/SiO ₂ , c) 529/203 ppm Na ₂ O/SiO ₂ after heating at 1525°C for 3 h).	91

4.10	TEM images of MgO-free powder samples with a) 529/203 ppm Na ₂ /SiO ₂ , b) 529/603 ppm Na ₂ /SiO ₂ , c) 1000/1000 ppm Na ₂ /SiO ₂ , and d) 29/103 ppm Na ₂ /SiO ₂ after sintering at 1525°C for 3 h	92
4.11	TEM image of a MgO-free powder sample with 29/603 ppm Na ₂ O/SiO ₂	93
4.12	TEM images of MgO-doped (380 ppm) powder samples with a) 60/82 ppm Na ₂ O/SiO ₂ , b) 60/582 ppm Na ₂ O/SiO ₂ , and c) 560/582 ppm Na ₂ O/SiO ₂ . After heating at 1525°C for 3 h	94
5.1	Micrographs of MgO-doped Bayer doped with 560 ppm Na ₂ O and 82 ppm SiO ₂ after 3 h at 1525°C obtained using a) a secondary electron detector and b) a backscattered electron detector.	105
5.2	a) XRD pattern and b) zoomed-in XRD pattern of a sample with 1060 ppm Na ₂ O, 82 ppm SiO ₂ , and 380 ppm MgO after sintering at 1525°C for 5 h. All observed peaks except for one (*) can be assigned to either α -Al ₂ O ₃ or β -Al ₂ O ₃	106
5.3	Micrographs showing β -Al ₂ O ₃ grains (red circles) in MgO-doped Bayer alumina samples with 82 ppm SiO ₂ and 560 ppm Na ₂ O after sintering at 1525°C for a) 0 h, b) 1 h, and c) 8 h.	107
5.4	Kinetics of β -Al ₂ O ₃ formation for different powder chemistries of MgO-doped powder samples.	108
5.5	Micrographs showing β -Al ₂ O ₃ grains (red circles) in MgO-doped Bayer alumina samples with 82 ppm SiO ₂ and a) 185 ppm Na ₂ O, b) 560 ppm Na ₂ O, and c) 1060 ppm Na ₂ O after sintering at 1525°C for 3 h.	109
5.6	Formation of β -Al ₂ O ₃ a function of Na ₂ O concentration in MgO-doped Bayer alumina.	110
5.7	Formation of β -Al ₂ O ₃ in MgO-doped powder samples a function of a) SiO ₂ concentration for different Na ₂ O concentrations, and b) Na ₂ O/SiO ₂ ratio. In b) the black diamonds are samples with 82 ppm SiO ₂ and the blue squares are samples with 182 and 582 ppm SiO ₂	111
5.8	Micrographs showing β -Al ₂ O ₃ grains (red circles) in MgO-doped Bayer alumina samples with a) 185/182 ppm Na ₂ O/SiO ₂ and b) 560/182 ppm Na ₂ O/SiO ₂ after sintering at 1525°C for 3 h.	112
5.9	Formation of β -Al ₂ O ₃ in MgO-free powder samples as a function of a) MgO concentration (29 ppm Na ₂ O) and b) Na ₂ O concentration (2 ppm MgO) after 3 h at 1525°C.	113

5.10	Micrographs showing β -Al ₂ O ₃ grains (red circles) in Bayer alumina samples with a) 1002 ppm MgO, 1000 ppm SiO ₂ , 29 ppm Na ₂ O, b) 2 ppm MgO, 1000 ppm SiO ₂ , 1029 ppm Na ₂ O, c) 1002 ppm MgO, 1000 ppm SiO ₂ , 1029 ppm Na ₂ O after 3 h at 1525°C.	114
5.11	Micrograph showing β -Al ₂ O ₃ grains (red circles) in an ultra high purity powder sample with 502 ppm Na ₂ O, 2 ppm MgO, and 11 ppm SiO ₂ after sintering at 1525°C for 3 h.	115
6.1	Dilatometry curves of non-aqueous slip cast CT3000 LS SG samples heated at a) 5°C/min, b) 10°C/min, and c) 20°C/min to 1525°C measured parallel to (z-direction) and perpendicular to (x/y-direction) the capillary force acting during slip casting.	130
6.2	Development of the shrinkage anisotropy factor for shrinkage, <i>k</i> , during densification of non-aqueous slip cast samples as a function of relative density for CT3000 LS SG samples heated at different rates.	131
6.3	Development of the relative density corrected for shrinkage anisotropy as a function of temperature for non-aqueous slip cast CT3000 LS SG samples heated at different rates.	132
6.4	Mean residuals of the MSCs assuming different values for <i>Q</i> for non-aqueous slip cast CT3000 LS SG samples.	133
6.5	MSCs of CT3000 LS SG samples prepared by non-aqueous slip casting using a) the <i>Q</i> -value obtained by accounting for shrinkage anisotropy (<i>Q</i> =550 kJ/mol) and b) using <i>Q</i> -value when shrinkage anisotropy was uncorrected for (<i>Q</i> = 625 kJ/mol).	134
6.6	MSCs and <i>Q</i> -values of CT3000LS-SG samples obtained from the minimum mean residuals for samples prepared by different forming techniques and accounting for shrinkage anisotropy.	135
6.7	a) Densification of dry pressed CT3000 LS SG samples at different heating rates, b) mean residuals as a function of <i>Q</i> , and c) MSC for <i>Q</i> = 700 kJ/mol obtained from the minimum mean residuals, showing divergence at densities >90%.	136
6.8	<i>Q</i> -values for dry pressed CT3000 LS SG samples as a function of relative density obtained from iso-density analysis.	137
6.9	Development of the microstructural parameters, summarized in the <i>C</i> parameter, as a function of relative density for dry pressed CT3000 LS SG samples.	138
6.10	MSCs and <i>Q</i> -values for CT3000 LS SG samples prepared by non-aqueous slip casting with different Na ₂ O concentrations.	139

6.11 Equivalent time/temperature diagram for CT3000 LS SG samples prepared by non-aqueous slip casting heated at 10°C/min. The contours may be used to predict heat treatments requirements to achieve a desired density.	140
---	-----

List of Tables

2.1	Physical and chemical characteristics of the as-received Bayer Al ₂ O ₃ powder used in this study.	28
2.2	Calculated compositions and amounts of liquid in as-received, singly doped and co-doped samples at 1525°C ($\alpha = \alpha\text{-Al}_2\text{O}_3$, $\beta = \beta\text{-Al}_2\text{O}_3$, L = liquid, M = mullite).	29
3.1	Physical and chemical characteristics of the as-received 380 ppm MgO-doped Bayer alumina powder used in this study.	54
3.2	Calculated compositions and amounts of liquid in 380 ppm MgO-doped Bayer alumina samples of different chemistries at 1450°C and 1525°C.	55
3.3	Lattice parameters and equilibrium energy (E_0) compared to previous first-principles and experimental values.	56
5.1	Physical and chemical characteristics of the alumina powder used in this study.	103
5.2	Estimated amount of $\beta\text{-Al}_2\text{O}_3$ in MgO-doped Bayer alumina samples after 3 h at 1525°C.	104
6.1	Q values obtained by MSC analysis for different alumina powders. .	129

Acknowledgments

The completion of graduate school and this dissertation could not have been possible without the support from many people that I would like to thank now. First, I would like to thank Prof. Gary Messing for guiding this research and helping me develop as a scientist. I learned a lot from Prof. Messing and I will always be indebted to him for his time, patience, and experience. I would like to thank my dissertation committee, Prof. James Adair, Prof. Douglas Wolfe, Prof. John Hellmann and Dr. Charles Compson for their time, constructive criticism and advice. I would like to thank Dr. Charles Compson and Dr. Joe Atria from Almatis, Inc. for funding this research and for many discussions that contributed substantially to the quality of this research. The staff of the Materials Characterization Laboratory was always supportive and helpful and I enjoyed working with them. Specifically, I would like to thank Joshua Maier and Haiying Wang for preparing my samples for TEM, and Dr. Jennifer Gray for spending many hours at the TEM with me. I would like to thank the past and present members of the Messing Research Group, (Dr. Elizabeth Kupp, Jesse Matson, Alexandra Wadja, Elisabeth Roch, Ryan Sommerhuber, Dr. Nuerxida Pulati, Marie Arnoult, Yi Yuan, Dr. Yunfei Chang, Beecher Watson, Rebecca Walton, Michael Brova, Anna Hofer, Kuo-Hao Lee, Jie Wu, Howard Payne, Dr. Raul Bermejo) for a great time in the lab and in the office, and many great discussions. It was an honor to get to work with so many great people. I want to thank the staff, faculty, and students of the Penn State Materials Science and Engineering Department for always being helpful and for creating a positive and great work environment. I want to thank all the friends I made at Penn State over the past few years, within and outside the Department of Materials Science (Christopher Rotella, Lyndsey Denis, Daniel Schuman, Tim Lichtenstein, Ethan Kahn, Nathan Smith, Tim Pillsbury, and many more). I am proud that I can call them my friends. I would like to thank my significant other, Cassie Marker for her support. She also contributed significantly to this dissertation by performing the first-principles DFT calculations, which I could not have done without her. Finally, I want to thank my family. My parents, grandparents, uncle, and brother always

supported and encouraged me, even when I decided to move half way across the globe for grad school. I am very grateful for their constant support.

Chapter 1

Introduction

1.1 Motivation

With an estimated total market of 2.8 million tons per year, specialty aluminas for non-metallurgical applications are arguably the most extensively used material in the field of ceramics. They are used in large volume applications such as high temperature refractories, technical ceramics, high voltage insulators, and functional fillers. The majority of Al_2O_3 applications use synthetic or specialty aluminas derived from Bayer feedstocks (Bayer aluminas), such as aluminum trihydrate ($\text{Al}(\text{OH})_3$), smelter grade Al_2O_3 and others. Bayer aluminas are typically 99.0 - 99.9% pure and contain Na_2O , CaO , Fe_2O_3 , and SiO_2 impurities that originate from the bauxite ore and/or Bayer process reagents (e.g., NaOH). The vast majority of research on the sintering of Al_2O_3 , however, focuses on ultrahigh purity ($\geq 99.99\%$) aluminas derived from specialty feedstocks, such as ammonium alum ($\text{NH}_4\text{Al}(\text{SO}_4)_2 \cdot 12\text{H}_2\text{O}$), boehmite ($\gamma\text{-AlOOH}$) and aluminum chloride (AlCl_3). Due to the higher cost involved in producing the high purity chemicals and to maintain the purity during subsequent processes to obtain ultrahigh-purity aluminas, these powders are typically one to two orders of magnitude more expensive than Bayer aluminas. Therefore, for many industrial applications aluminas derived from the Bayer process constitute an overwhelming majority of the global market share of over 90%.

While ultrahigh purity aluminas provide the purest platform from which to conduct fundamental sintering research, that research does not usually explore the types and amounts of impurities typical of Bayer aluminas. Commercial Bayer

Al_2O_3 powders exist in a range of reactive grades that differ in the amount and types of these impurities, and additionally to impurities the manufacturer commonly adds MgO to commercial alumina powders since it is known for its beneficial effect during sintering. A fundamental understanding of the mechanisms of densification, grain growth and second phase formation is key for predicting and tailoring the sintering behavior and microstructure evolution of Bayer alumina powders based on their chemistry, and will provide valuable information to industrial users.

The purpose of this dissertation is to develop a fundamental, in-depth understanding about how the chemistry of commercial Bayer alumina powder affects sintering mechanisms, densification, grain growth, and the formation of second phases. Specifically, this dissertation will focus on investigating the effects and cross effects of MgO , Na_2O and SiO_2 on densification and microstructure evolution of Bayer aluminas, and provide insight into the fundamental mechanisms that are responsible for changes in sintering behavior. Furthermore, a model is developed to describe the dynamic development of grain boundaries during densification as a function of powder chemistry. It is crucial to understand the structure and chemistry of grain boundaries during sintering, as grain boundary diffusion is the dominant mechanism for mass transport. The methodology developed to analyze densification, microstructure evolution, sintering mechanisms, and grain boundaries during densification will serve as an example for investigating and tailoring the mechanisms of sintering in ceramic powders as a function of powder chemistry. Finally, the Master Sintering Curve approach is evaluated as a tool to identify powder chemistry effects on the sintering of Bayer alumina in a fundamental, predictive way.

1.2 Sintering of Ceramics

Sintering is the heat treatment of a particle mass, or high surface area powder, that results in a strength increase, reduction in surface area and, usually, densification. Sintering is used to fabricate bulk ceramic components and powder metallurgical parts [4], and can be divided into two main types; solid state sintering and liquid phase sintering. The difference between these two types of sintering is the absence or presence of a liquid phase, respectively, which results in fundamental differences in sintering mechanisms.

The sintering process can be divided into three stages; initial, intermediate, and final stage sintering [4]. Initial stage sintering accounts for the first few percent of densification, during which particles rearrange as a result of capillarity and contacts between particles form. The majority of densification occurs from \sim 65 to \sim 92% relative density occurs and is termed intermediate stage sintering. During this stage the microstructure is characterized by pore channels along the grain edges. Little to no grain growth occurs during intermediate stage sintering since the presence of pore channels limits the mobility of grain boundaries. Intermediate stage solid state sintering is governed by densifying mechanisms, such as grain boundary and volume diffusion. In the presence of a liquid phase, grain boundary diffusion occurs by a solution-precipitation mechanism, where material from the particle - grain boundary interface dissolves into the liquid grain boundary phase, diffuses through the liquid grain boundary phase, and precipitates at sites of highest negative curvature, which is usually at the particle necks. In solid state sintering this diffusion process occurs by solid-state diffusion along the grain boundaries. At densities $>$ 92% the pore channels that have formed during intermediate sintering close and form isolated pores on grain boundaries, which are eliminated during final stage sintering until full density is reached. Grain growth sets in after the closing of the pore channels at densities $>$ 92% since grain boundaries with isolated pores are more mobile than grain boundaries with pore channels. As long as the mobility of the grain boundaries do not exceed the mobility of the pores, full density can be obtained. However, in many ceramic systems abnormal grain growth sets in at some point during sintering, and a limited number of grains grow abnormally fast, which results in a bimodal grain size distribution. Microstructures exhibit a few large grains, which are surrounded by a fine-grained matrix with grains that are orders of magnitude smaller than the large grains. The fast growth of these grains is due to a higher mobility of the grain boundaries of the large grains, which is much faster than the mobility of the pores. In this case pores cannot be removed fast enough from these grain boundaries, get trapped in the grains and remain in the final microstructure. Hence, the final density of a ceramic is often limited by the onset of abnormal grain growth.

1.3 Effects of Impurities and Dopants on the Sintering of Al₂O₃

1.3.1 MgO in Ultrahigh Purity Al₂O₃

For a long time the performance and application of alumina as a technical ceramic was limited because it is known to exhibit abnormal grain growth. In 1961 Coble discovered that MgO-doping can suppress abnormal grain growth and high-density translucent alumina can be produced this way [5–7]. Since then numerous studies have attempted to understand the underlying mechanisms. Initially Coble proposed four possible mechanisms for the suppression of abnormal grain growth by MgO. As a first possible mechanism he proposed that spinel particles precipitate, pin the grain boundaries and prevent abnormal grain growth. The second mechanism he proposed was a solid-solution pinning mechanism, which assumed that MgO is preferentially adsorbed in the grain boundaries and inhibits abnormal grain growth by lowering the grain boundary mobility. The third proposed mechanism was that MgO could affect the pore shape and thereby increase the effect of pore pinning on grain boundary movement. The fourth proposed mechanism, which was the explanation Coble favored at that time, was that a minimum amount of time is required to nucleate abnormal grains after a critical density is reached, and that MgO increases the densification rate sufficiently to prevent the nucleation of abnormal grains. Since then multiple researchers have found arguments that support all of these mechanisms [8]. Jorgensen and Westbrook [9, 10] showed indirect evidence for MgO segregation to the grain boundaries and explained the effect of MgO on the sintering of Al₂O₃ by a solute pinning mechanism, where MgO influences the diffusion coefficient or surface energy through defect chemistry effects. Johnson and Coble [11] did not find evidence for MgO segregation in their experiments, and proposed that sintering kinetics change due to an increase in diffusion coefficient by the formation of a solid solution of MgO in Al₂O₃, which causes a change in grain growth and pore elimination rate. An alternative model was proposed by Heuer [12], which assumed that MgO increases the pore mobility by increasing the surface diffusivity and, therefore, prevents pore-grain boundary breakaway and abnormal grain growth.

A variety of the mechanisms described above were summarized in a segreg-

tion and precipitation map in unpublished work by Carry, Legros, Bowen, and Lartigue [1] as shown in Figure 1.1. They proposed that when the MgO content in Al_2O_3 exceeds the maximum solubility of MgO in the Al_2O_3 lattice and a critical concentration of MgO in the grain boundaries, the excess MgO and Al_2O_3 form spinel precipitates. Schottky defects are formed below the solubility limit of MgO in the Al_2O_3 crystal, and the increased concentration of point defects facilitates diffusion and hence promotes the sintering by enhancing densification and grain growth. MgO concentrations that exceed the solubility of MgO in the Al_2O_3 lattice segregate to the grain boundaries, and when the solubility of MgO in the Al_2O_3 crystal and grain boundaries is exceeded, spinel precipitates form on the grain boundaries, which reduces the grain boundary mobility by a pinning mechanism, and thus inhibits grain growth. With increasing grain size the required MgO concentration for the formation of spinel decreases, as seen from the segregation and precipitation map in Figure 1.1. The total area of the grain-boundary interface decreases with increasing grain size, and hence the critical concentration of MgO in the Al_2O_3 grain boundaries changes. While this proposed segregation precipitation map explains the observed segregation of MgO to grain boundaries and the precipitation of spinel, the key mechanism by which MgO improves the sintering of alumina cannot be identified. However, the segregation precipitation map implies that several of the described mechanisms may contribute to the effect of MgO on the sintering of alumina.

1.3.2 Effects of Impurities during sintering of Al_2O_3

After it was discovered that ppm levels of MgO are sufficient to drastically affect the sintering behavior of alumina [5–7], there has been high academic and commercial interest in understanding how small concentrations of other dopants or impurities such as Na_2O , CaO , Fe_2O_3 , and SiO_2 affect the sintering kinetics, density and microstructure evolution of alumina. An overwhelming amount of literature exists on how impurities, specifically SiO_2 and CaO , affect the sintering of ultrahigh purity aluminas, and the literature is in agreement that SiO_2 and CaO can form a liquid phase, which allows abnormal and anisotropic grain growth. Bae and Baik [13, 14] showed that there is no abnormal grain growth in Al_2O_3 , as long as the total impurity content is below 10 ppm, and it was realized that abnormal grain

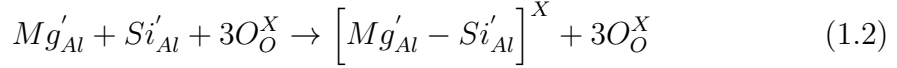
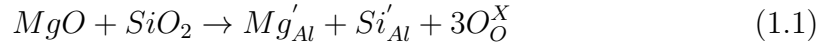
growth during sintering is not intrinsic to alumina, but depends on the presence of trace amounts of impurities on the ppm level, which form a liquid film on grain boundaries [2,8,15,16]. By co-doping of Al_2O_3 with SiO_2 and CaO Bae and Baik [13] were able to show that a liquid forms during sintering as soon as the solubility of SiO_2 and CaO in Al_2O_3 is exceeded. They estimated the solubility of SiO_2 and CaO in Al_2O_3 to be 100 and 20 ppm, and that abnormal grain growth sets in after a critical thickness of the amorphous grain boundary has formed. This implies that impurity contents in commercial alumina powders with purity levels from 99.7 - 99.9% are high enough to form a liquid phase during sintering, if glass-forming impurities are present, as demonstrated by Hansen and Philips [17]. Harmer [18] reported that even in 99.98% pure alumina the impurity level is high enough for the formation of a liquid phase during sintering and it was concluded that abnormal grain growth could only be prevented by adding sintering additives such as MgO .

1.3.3 Effects of MgO on Liquid Phase Sintering of Al_2O_3

Since it was established that abnormal grain growth is due to the presence of glass forming impurities in alumina, the role of MgO in alumina needed to be addressed in the context of these impurities, since MgO prohibits the deleterious effect of small amounts of liquid phase-forming impurities during sintering and facilitates the formation of a dense and homogeneous submicron microstructure. Several reasonable explanations can be found in the literature to explain this positive effect of MgO on the sintering behavior of Al_2O_3 containing small amounts of other impurities [8,19]. Regardless of the presence of other impurities, the solute-pinning mechanism and the pinning-by-particle-precipitation mechanism are commonly accepted interpretations of the role of MgO on sintering of Al_2O_3 [20,21]. Bae and Baik [15] suggested, that MgO acts as a glass modifier in glassy grain boundary films and changes the kinetics of dissolution precipitation mass transport by modifying the viscosity. Additionally, a reduction of the kinetics for dissolution into and precipitation from the liquid phase was considered as a key mechanism for sintering of MgO -doped alumina [8,19].

Handwerker et al. [16] proposed that MgO can increase the solubility of SiO_2 in Al_2O_3 by co-dissolving MgO , since the difference in size and charge of Mg^{2+} and Si^{4+} relative to Al^{3+} in the alumina lattice can compensate each other. This

co-dissolution mechanism is supported by the work by Gavrilov et al. [2], who investigated the distribution of impurities in sintered Al_2O_3 by high-resolution scanning secondary mass spectrometry (SIMS). Figure 1.2 shows the SIMS maps of sintered Al_2O_3 singly doped with (a) 500 ppm MgO and (b) 1000 ppm SiO_2 . Areas of high dopant concentrations appear bright, and in both cases it can be seen that the dopants segregate to the grain boundaries. Furthermore, they showed that if Al_2O_3 is co-doped with 500 ppm MgO and 1000 ppm SiO_2 , both dopants segregate to the grain boundaries, but show a substantially higher MgO and SiO_2 concentration towards the grain center, as shown in the SIMS maps in Figure 1.3. The authors concluded that the solubility of MgO and SiO_2 in Al_2O_3 is increased by co-doping via the following defect compensation mechanism:



A similar reaction was proposed by Coble and Roy [22] to explain a higher solubility of TiO_2 in Al_2O_3 when an equimolar amount of MgO is added. Gavrilov et al. [2] concluded that MgO increases the solubility of glass forming impurities in Al_2O_3 and therefore prevents the formation of a liquid phase during sintering. However, while they showed that there are higher Si and Mg concentrations in the alumina grains, they did not prove that no liquid phase exists in these samples.

1.3.4 Grain Boundaries During Sintering of Al_2O_3

After the importance of grain boundaries for sintering of ceramics with ppm amounts of impurities and dopants was discovered, more recent literature has focused on developing general models based on grain boundary structures and chemistries to explain the sintering behavior and grain growth of ceramics. For example Harmer and his group [23–26] proposed that impurities form thermodynamically stable grain boundary "phases", which they refer to as "complexions". Depending on the thickness of the adsorbed layer, i.e. the grain boundary thickness, they distinguish between six complexions: clean, monolayer, bilayer, multilayer, nanolayer and wetted, which can be either ordered or amorphous and show transitions from one to another during sintering.

According to their model the mobility of the grain boundaries is determined by the type of complexion, which depends on impurity type and concentration, temperature and crystal orientation of adjacent crystals. During densification and grain growth impurities remain in the grain boundaries after the solubility in the crystal is exceeded. Grain boundaries can be sites for supersaturation during sintering because of the reduction of grain boundary area due to grain growth. The authors argue that there are only two possibilities for the excess impurities to reduce the free energy of the system; the formation of a new phase, or the transition to another complexion [24]. The predominance of either events depends on the relative activation energies. Since crystal planes of different orientation have different grain boundary or interface energies different complexions may co-exist in a microstructure. How many and what type of complexions coexist mainly depends on the temperature. Inhomogeneous impurity distribution may also be considered as a reason for the formation of different complexions.

Using this concept the authors interpret the microstructure development of Al_2O_3 with different impurities. CaO impurities in Al_2O_3 can form calcium hexaluminate, which shows epitaxy on the basal planes of $\alpha\text{-}\text{Al}_2\text{O}_3$. The interface energy between the basal planes of $\alpha\text{-}\text{Al}_2\text{O}_3$ and calcium hexaluminate is low and therefore also the activation energy for formation. But for crystal planes with other orientations the activation energy for formation of calcium hexaluminate is high. Therefore, the theory suggests that complexion transitions are preferred on these planes and that the different grain boundary mobilities of the basal planes compared to all other planes lead to anisotropic abnormal grain growth, which is often observed in CaO containing alumina.

SiO_2 in Al_2O_3 does not have a preferred crystal plane on which it can form precipitations with low interfacial energy. The activation energy for precipitation is high for all crystal orientations and, therefore, this system is interpreted to prefer complexion transitions rather than the formation of a new phase. It is stated that complexions with higher grain boundary mobilities form upon heating and that grain growth is enhanced. Dillon and Harmer's [23, 27] interpretation for MgO in Al_2O_3 is that spinel precipitates are formed, and that this system behaves isotropic and exhibits low interface energies on several crystal planes. Therefore, it is stated that the activation energy for precipitation is low as well and that complexion transitions are prevented by the formation of spinel precipitates, or the

precipitations occur uniformly throughout the microstructure.

While this model can fundamentally explain the grain growth behavior in fully dense microstructures, it cannot explain observed differences in densification and how different chemistries, i.e. concentration and ratios of different impurities, and grain boundary structures affect the rate-limiting sintering mechanisms.

A different model, based on the activation energy and the driving force for atoms to cross the grain boundary, was developed by Kang et al. [4, 28, 29] to explain microstructure evolution in ceramics and metals. According to this model grains grow normal and an equiaxed microstructure develops if the critical driving force for grain boundary migration is zero and the grain interface is atomically rough. The critical driving force for grain boundary migration is determined by factors such as temperature, dopant concentration, and oxygen partial pressure, and if the critical driving force is zero then the step free energy, i.e. the additional surface energy created during nucleation and growth of grains (the ledges of the nucleus), has to be zero. If the critical driving force is not zero, then grains grow faceted, and if the maximum driving force, i.e. the driving force for the largest grains to grow, is larger than the critical driving force, then abnormal grain growth occurs. If the maximum driving force is much larger than the critical driving force, i.e. the driving force of many grains is larger than the critical driving force, many grains start growing fast ("abnormally") forming a microstructure that looks like a normally grown microstructure, and this is defined as pseudo-normal grain growth. If the maximum driving force is less than the critical driving force, then grain growth is stagnant, i.e. the microstructure does not change.

Kang et al. [28, 29] investigated a variety of parameters such as partial pressure, temperature, dopants, and impurities for different material systems, but explained the microstructure evolution only qualitatively with the described model, and the majority of observations from experiments were fitted into the model rather than predicted by the model. For example, it is concluded that MgO lowers the step free energy of alumina since the addition of MgO to alumina results in a homogeneous and equiaxed microstructure [30]. However, it is not explained why MgO lowers the step free energy, and why MgO is the only material that lowers the step free energy in that manner. Furthermore the model only takes into account the microstructural evolution in fully dense bodies and does not address densification.

1.4 Sintering of Bayer Alumina

1.4.1 The Bayer Process

The Bayer process is a hydrothermal precipitation process in which bauxite ore is digested in an aqueous solution of caustic soda (NaOH) at temperatures up to 230°C and pressures up to 40 bar. Bauxite consists of a variety of minerals, including gibbsite ($\text{Al}(\text{OH})_3$), boehmite ($\gamma\text{-AlO(OH)}$), diasporite ($\alpha\text{-AlO(OH)}$), goethite (FeO(OH)), haematite (Fe_2O_3), and kaolinite ($\text{Al}_2\text{Si}_2\text{O}_5(\text{OH})_4$). During digestion in NaOH the Al-containing minerals form $\text{NaAl}(\text{OH})_4$, which dissolves as a complex. Fe- and Si-containing minerals and other accessory minerals are insoluble under these conditions and can be separated as red mud. The temperature of the sodium aluminate solution is decreased to $50\text{-}70^\circ\text{C}$ and the addition of $\gamma\text{-Al}(\text{OH})_3$ seed crystals results in the precipitation of $\gamma\text{-Al}(\text{OH})_3$ from the solution. Heat treatment and calcination of the $\gamma\text{-Al}(\text{OH})_3$ at $1100\text{-}1200^\circ\text{C}$ leads to the formation of $\alpha\text{-Al}_2\text{O}_3$.

SiO_2 and Fe_2O_3 are the main components of the Bauxite ore, additionally to Al_2O_3 , and hence low concentrations of SiO_2 and Fe_2O_3 are present in the final powder. Additional SiO_2 impurities may originate from the milling media that is used by the manufacturer to grind the calcined powder to the desired particle size [8, 31]. Na_2O impurities result from the digestion of the bauxite in NaOH and the consequent precipitation of $\text{Al}(\text{OH})_3$ crystals from the $\text{NaAl}(\text{OH})_4$ solution. Small amounts of Na_2O are precipitated within the $\text{Al}(\text{OH})_3$ crystals [31]. To remove NaOH from the powder surface, the $\text{Al}(\text{OH})_3$ is washed after precipitation. However, small amounts of NaOH or rather Na_2O after calcination, remain on the powder surface. Hence, Na_2O impurities are either distributed on the surface, or entrapped in the alumina grains in Bayer process alumina powders. Other impurities such as gallium, calcium and magnesium originate from accessory minerals in the bauxite [8].

1.4.2 Influence of Na₂O and SiO₂ on the Sintering Behavior of Al₂O₃

The Bayer process illustrates that alumina powders obtained by this process inevitably contain trace amounts of impurities, such as Na₂O and SiO₂. Despite the extensive use of Bayer alumina there are relatively few published studies on the effects of Na₂O on its sintering. Sumita and Bowen reported on the effect of adding 1 wt.% Na₂O to a high purity alumina powder (Sumitomo, AKP-HP) [32]. However, they determined that only ~8 ppm Na₂O was present in the alumina after sintering at 1400°C for 2 h, without additional details to explain the large discrepancy between the doping concentration and the amount determined by inductively coupled plasma (ICP) spectrometry after sintering. Smothers and Reynolds [33] investigated the influence of 1 wt.% of different additives on the sintering of 99.3% pure alumina (Alcoa A-11) and showed that Na₂CO₃ or NaF retard sintering and inhibit grain growth.

Cahoon and Christensen [34] reported a deleterious effect of Na₂O on the sintering of alumina as well. They added between 0.03 and 5.9 wt.% Na₂O to their alumina powder (Alcoa A-14, no purity specifications given) and heated the samples in a 5 days cycle (2 days heating, 3 days cooling) to temperatures between 1600°C and 1835°C for 1 h. A very strong retardation of sintering and inhibition of abnormal grain growth was reported for increasing Na₂O concentration. They observed cracking of their samples and inferior compressive strengths and suggested that this deleterious effect might be due to the formation of β - or ξ -Al₂O₃. They also studied the effect of SiO₂ on the sintering of Al₂O₃ and reported a "moderately deleterious effect" of SiO₂. They claim that it strongly inhibits abnormal grain growth at concentrations as low as 0.1% and that this effect is enhanced with increasing SiO₂ content. They reported that the deleterious effect of Na₂O was moderated in Na₂O/SiO₂ co-doped Al₂O₃.

Louet et al. [35] studied the effect of Na₂O and SiO₂ doping on densification and microstructure evolution of a Bayer process alumina (Rhone-Poulenc, P172SB), containing 550 ppm Na₂O, 770 ppm SiO₂, 1010 ppm MgO, 600 ppm CaO and 115 ppm Fe₂O₃. Na₂O and SiO₂ levels were adjusted by adding CH₃COOH-Na and silica gel. When they added Na₂O, the concentrations in the samples after sintering for 2 h at 1540°C, as measured by ICP spectrometry, were less than 50% of the targeted

amount, and they explained this difference by the low vaporization temperature of Na₂O [35]. Louet et al. concluded that Na₂O slows the sintering process and decreases the sintered density from 98 to 97% for Na₂O concentrations of 550 ppm and 1150 ppm, respectively, when sintered at 1540°C for 2h. The authors reported that a high level of Na₂O results in a fine, homogeneous microstructure. They observed a drop in grain size from 4 - 5 μm to 3 μm when exceeding 1000 ppm Na₂O. This work also showed that increasing SiO₂ concentration from 770 ppm to as high as 1500 ppm in the presence of Na₂O does not affect the final density but does cause anisotropic grain growth. Even though one can see an increase in grain size but no abnormal grain growth as the SiO₂ concentration increases in the presented micrographs, the authors state that increasing the SiO₂ concentration has no effect on the average grain size but leads to abnormal grain growth. As noted by the authors, these results are difficult to interpret in terms of Na₂O and SiO₂ effects due to the large number and high concentrations of impurities in the as-received powder.

Compson et al. [31] investigated the effect of SiO₂ and Na₂O concentration on the sintering behavior of alumina. They chose four commercial alumina powders with similar specific surface areas, particle diameter and particle distributions. All powders were 99.8% pure, but showed different concentrations for the single impurities. Particularly, the Na₂O and SiO₂ concentrations varied from 0.02 to 0.1% and 0.01 to 0.04%, respectively. Using dilatometry they showed that the four powders exhibit different shrinkage, sintering and densification behavior in the temperature range from 1150°C to 1500°C. They concluded that SiO₂ has a deleterious effect on the sintering of Al₂O₃, but they could not detect an influence of Na₂O.

This literature survey shows that there is some disagreement about whether ppm levels of Na₂O and SiO₂ have a positive, negative, or no effect on sintering of alumina, and unfortunately none of the literature reports investigated fundamental mechanisms that would explain their observations. While most authors acknowledged the presence of other impurities and dopants, such as MgO, their effect and possible cross effects with other impurities or dopants were not considered. The lack of understanding of this system was the motivation to investigate the fundamental mechanisms that are responsible for changes in sintering behavior as a function of powder chemistry in Bayer process-derived Al₂O₃.

The chapters of this dissertation have either been published, submitted for publication, or will be submitted for publication in peer-reviewed scientific journals. As a result some degree of self-plagiarism was necessary to construct this dissertation.

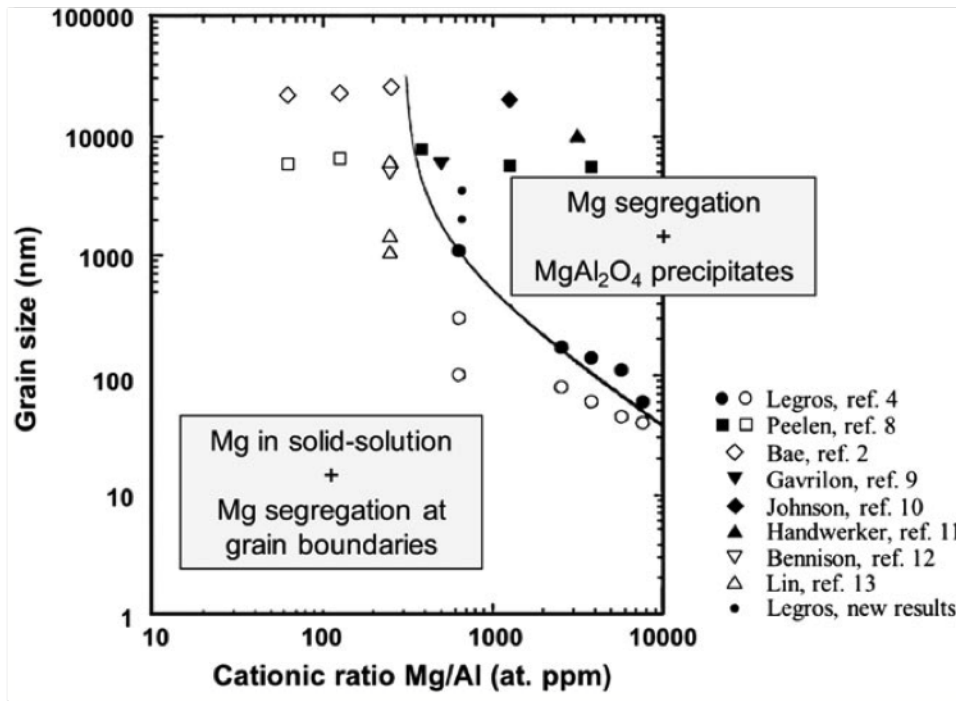


Figure 1.1. Segregation and precipitation map of MgO-doped alumina based on the results in the literature [1].

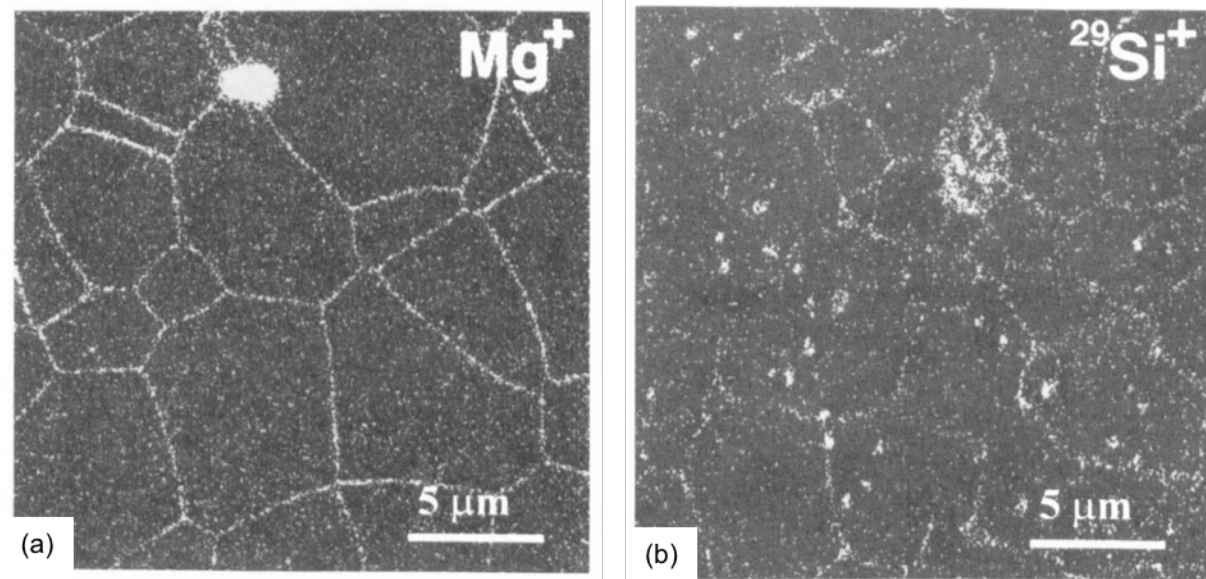


Figure 1.2. SIMS maps of Al_2O_3 doped with 500 ppm MgO (a) and 1000 ppm SiO_2 (b). Samples were sintered for 8 h at 1650°C [2].

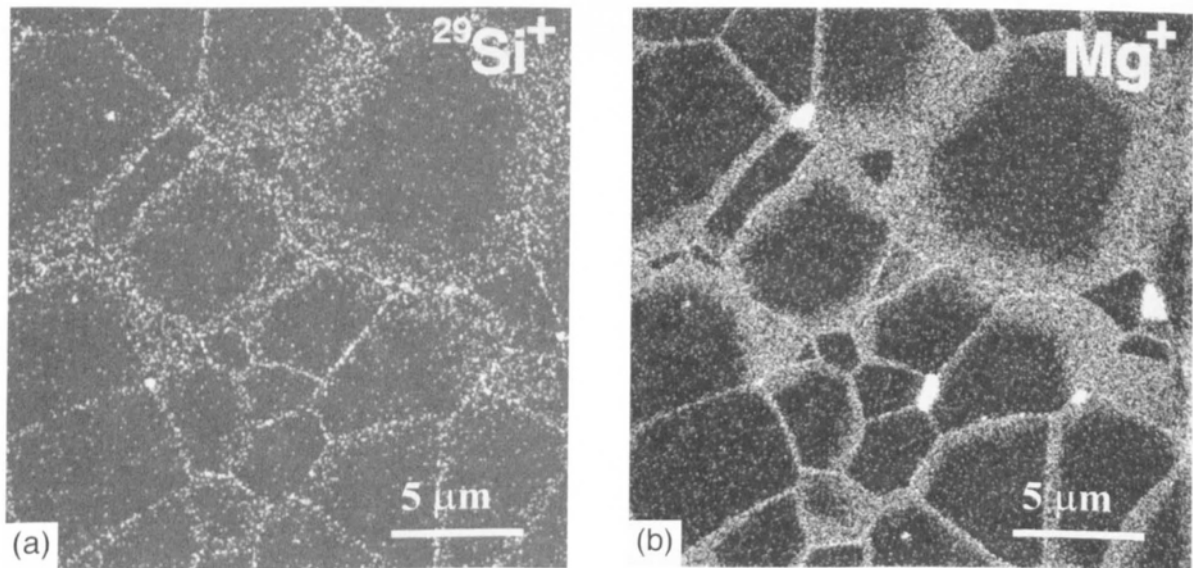


Figure 1.3. SIMS maps of Al_2O_3 co-doped with 500 ppm MgO and 1000 ppm SiO_2 and sintered at 1650°C for 8h. (a) shows the distribution of SiO_2 , (b) the distribution of MgO in the same samples [2].

Chapter 2 |

The Effects of Na₂O and SiO₂

on Liquid Phase Sintering of Bayer

Al₂O₃

2.1 Introduction

Al₂O₃ is arguably the most extensively used and researched ceramic material because it is used in many large volume applications such as high temperature refractories, technical ceramics, high voltage insulators, and functional fillers. The majority of Al₂O₃ applications use synthetic or specialty aluminas derived from Bayer feedstocks, such as aluminum trihydrate (Al(OH)₃), smelter grade Al₂O₃ and others. Bayer process aluminas are typically 99.0 - 99.9% pure and contain Na₂O, CaO, Fe₂O₃, and SiO₂ impurities that originate from the bauxite ore and/or Bayer process reagents (e.g., NaOH). The vast majority of research on the sintering of Al₂O₃, however, focuses on ultra-high purity ($\geq 99.99\%$) aluminas derived from specialty feedstocks, such as ammonium alum (NH₄Al(SO₄)₂·12H₂O), boehmite (γ -AlOOH) and aluminum chloride (AlCl₃). While ultra-high purity aluminas provide the purest platform from which to conduct fundamental sintering research, that research does not usually explore the types and amounts of impurities typical of Bayer aluminas. Commercial Bayer Al₂O₃ powders exist in a range of reactive grades that differ in the amount and types of these impurities. Therefore, the evaluation of specialty reactive aluminas, within the context of previous work on ultra-high purity aluminas, is a valuable contribution to industrial users and bridges

fundamental sintering research with ultra-high purity aluminas.

2.2 Experimental

A chemically purified 0.4 μm median particle size Bayer process Al_2O_3 powder (Almatis, Inc., Leetsdale, PA, USA) with only 2 ppm MgO was used to study the sintering of near MgO -free Bayer Al_2O_3 (Figure 2.1). The powder was chemically purified by the manufacturer so that impurity levels similar to commercial high purity Bayer process aluminas were obtained after doping with Na_2O and/or SiO_2 . The physical and chemical characteristics of the as-received powder are shown in Table 2.1. Chemical analysis of the as-received Al_2O_3 was performed by inductively coupled plasma (ICP) emission spectroscopy (iCap 6000, Thermo Fischer Scientific, Inc., Waltham, MA, USA) after Al_2O_3 samples were acid digested in a microwave digestion unit in a TeflonTM sample holder. It should be noted that the as-received Bayer Al_2O_3 contained impurity levels of 90 ppm Fe_2O_3 , 62 CaO , and 22 ppm TiO_2 . The Na_2O and SiO_2 concentrations reported after doping include the impurity concentrations in the as-received powder (29 ppm Na_2O and 103 ppm SiO_2).

The Al_2O_3 powders were doped with up to 1000 ppm Na_2O using sodium acetate ($\text{NaC}_2\text{H}_3\text{O}_2 \cdot 3\text{H}_2\text{O}$, ACS grade, BDH, West Chester, PA, USA), based on the procedure reported by Louet et al. [35]. The Al_2O_3 powders were dispersed in a solution of sodium acetate dissolved in de-ionized water. The suspension was stirred on a magnetic stir plate for 5 h at room temperature, and held at 80°C for 24 h while stirring until the mixture was too viscous to stir, and then dried at 100°C for 24 h.

Samples were doped with up to 500 ppm SiO_2 by first dissolving tetraethyl orthosilicate (TEOS, $\text{Si}(\text{OC}_2\text{H}_5)_4$, 98%, Aldrich Chemical Company, Inc., Milwaukee, WI, USA) in 200 proof ethanol with a few drops of de-ionized water to hydrolyze the TEOS and immediately mixed at room temperature for 5 h with either the as-received or Na_2O -doped Al_2O_3 powder. The mixture was subsequently stirred at 70°C for an additional 12 h. The powder was then dried at 100°C for 2 h, followed by crushing in a mortar and pestle, and sieving to -106 μm (US Standard 140 mesh).

Samples were prepared for sintering studies by uniaxially dry pressing the powders at 170 MPa and then cold isostatic pressing at 200 MPa (CIP, Autoclave

Engineers, Erie, PA, USA) to obtain cylindrical samples (3.0-3.5 mm long by 12.7 mm diameter or 8.5-10 mm long by 6 mm diameter) with green densities of 59.0% \pm 0.5% of theoretical density. To investigate the sintering process, dry pressed 8.5-10 mm long by 6 mm diameter cylinders were heated at 10°C/min to 1525°C in a thermomechanical analyzer (TMA, Linseis PT1600, Robbinsville, NJ, USA). The kinetics of sintering and grain growth were evaluated on 3.0-3.5 mm long by 12.7 mm diameter samples heated at 10°C/min to 1200 °C then 5°C/min to 1525°C followed by sintering at 1525°C for up to 8 h. The density of three samples of each condition was measured by the Archimedes method according to ASTM standard B962-15 [36] and the average density reported for each sintering time and temperature. For microstructure analysis, samples were first polished to a surface finish of 1 μ m and then thermally etched in air at 1425°C for 40 min. Average grain sizes were measured on SEM (ESEM, Quanta 200, FEI Company, Hillsboro, OR, USA) micrographs using a linear intercept method (ASTM Standard E112-96) [37].

2.3 Results

2.3.1 Effects of Na₂O-doping

The doping experiments were designed to uniformly distribute Na₂O and SiO₂ on the surfaces of the Al₂O₃ particles. Upon heating the dopant NaC₂H₃O₂·3H₂O first dehydrates and then decomposes to form Na₂CO₃ above 385°C [38]. Using a video recorder, we observed that anhydrous sodium acetate melts and rapidly spreads on the surface of an Al₂O₃ substrate at \sim 420°C. Na₂CO₃ melts at 851°C and subsequently decomposes to Na₂O [38]. As a result of the rapid wetting of the Na₂O precursor on the Al₂O₃ substrate we conclude that Na₂O is uniformly distributed on the powder surface by the acetate doping process.

Figure 2.2 shows the shrinkage behavior of Bayer Al₂O₃ doped with different Na₂O concentrations during heating to 1525°C at 10°C/min. The as-received Al₂O₃ (intrinsic impurities: 29 ppm Na₂O, 103 ppm SiO₂) begins to shrink at \sim 1050 °C, whereas shrinkage begins at \sim 1100°C for samples doped with 1029 ppm Na₂O. The difference in density at the beginning of densification continues throughout the heating cycle. However, above \sim 1350°C the densification rate of the Na₂O doped samples surpasses that of the as-received sample. Overall, the Na₂O-doped samples

are 2.5% less dense than the as-received Al_2O_3 after heating to 1525°C.

Figure 2.3 shows the influence of Na_2O concentration on the densification kinetics at 1525°C. Clearly, the degree of densification decreases with increasing Na_2O concentration for up to 30 min with the Na_2O -doped samples being as much as 2% less dense than the as-received Al_2O_3 . However, after ≥ 30 min at 1525°C densification is independent of Na_2O content and all samples are 97.5-98.0% dense after ≥ 3 h.

The microstructures of as-received samples (29 ppm Na_2O) and doped samples with 529 ppm Na_2O sintered for 30 min, 3 h and 8 h at 1525°C are compared in Figure 2.4. It is seen that higher Na_2O concentration does not affect the average grain size for all hold times. Microstructures of as-received samples are predominantly equiaxed with a small number of faceted grains, whereas samples doped with Na_2O appear to have an increasing number of faceted grain boundaries with increasing Na_2O concentration. A few tabular grains of up to $60 \mu\text{m}$ were seen in both as-received and Na_2O -doped samples after 8 h at 1525°C (see Figure 2.4c and 2.4f). Those faceted grains are larger in the as-received powder samples compared to Na_2O -doped samples, whereas the Na_2O -doped samples show more large tabular grains than samples from the as-received powder.

2.3.2 Effects of $\text{Na}_2\text{O}/\text{SiO}_2$ co-doping

As seen in Figure 2.5, the presence of 603 ppm SiO_2 significantly retards densification of as-received alumina. Starting at $\sim 1250^\circ\text{C}$, all of the SiO_2 -doped samples densify less than as-received and singly Na_2O -doped samples. The densification rate of the SiO_2 -doped samples from 1250 to 1525°C is slower than the as-received alumina. SiO_2 reduces the linear shrinkage by $\sim 3.0\%$ and thus the samples are 8.7% less dense than the as-received Al_2O_3 after 8 h at 1525°C.

The densification kinetics of the Al_2O_3 powders doped with different amounts of Na_2O (154 and 529 ppm) and SiO_2 (203 and 603 ppm) are compared in Figure 2.6. It is seen that the addition of SiO_2 significantly reduces sintered density for all hold times. For example, samples containing as much as 603 ppm SiO_2 have densities of 81.5% after 0 h and 93.8% after 8 h at 1525°C, whereas the as-received and singly Na_2O -doped Al_2O_3 samples are 98% dense after 3 h at 1525°C.

Figure 2.6 shows the effect of Na_2O on the densification of SiO_2 -doped samples.

For hold times < 1 h, samples doped with 529 ppm Na₂O and 203 ppm SiO₂ are ~ 1.5% denser than samples doped with 154 ppm Na₂O and 203 ppm SiO₂. A difference in Na₂O concentration does not affect the final density of samples containing 203 ppm SiO₂ (96.5 - 97.0%) after 3 h at 1525°C. For higher SiO₂ concentrations (603 ppm), singly SiO₂ doped samples are 1 - 2.5% less dense than samples co-doped with 529 ppm Na₂O and 603 ppm SiO₂ for all hold times at 1525°C.

The average grain sizes of the as-received and Na₂O-doped samples are nominally the same and increase from 1.6 μm to 2.5 μm after 30 min and 8 h at 1525°C, respectively. There was little grain growth (1.4 μm to 2.1 μm) in singly SiO₂-doped samples (603 ppm) after 30 min and 8 h at 1525°C, respectively. In samples co-doped with 529 ppm Na₂O and 603 ppm SiO₂ the average grain size is 1.6 μm for hold times between 30 min and 8 h at 1525°C. The limited grain growth is attributed primarily to the large fraction of porosity. Micrographs of 603 ppm SiO₂ singly doped and 529 ppm Na₂O and 603 ppm SiO₂ co-doped samples heated for 8 h after heating for 8 h at 1525°C are compared in Figure 2.7. Both samples are only 92-94% dense and thus it was difficult to prepare polished micrographs without some grain pull-out.

2.4 Discussion

To understand the above effects, we first note from the Al₂O₃-Na₂O phase diagram [39] that Na₂O is insoluble in α -Al₂O₃. A few platelet shaped grains with high aspect ratios were observed in the microstructures of sintered Na₂O-doped samples (Figure 2.8). Due to their morphology and literature reports [40–44], it is assumed that these grains are a type of β -Al₂O₃. Four types of β -Al₂O₃ exist; two of them, β -Al₂O₃ (Na₂O·11Al₂O₃) and β'' -Al₂O₃ (Na₂O·5Al₂O₃), form in the binary system Na₂O-Al₂O₃ [45, 46]. The determination of which type of β -Al₂O₃ forms and the conditions of formation were not the subject of this work, so these analyses were not performed.

Sodium aluminate (NaAlO₂) is reported to form at temperatures as low as 900°C, [47] and β'' -Al₂O₃ (Na₂O·5Al₂O₃) can be synthesized at temperatures as low as 1100°C [40, 48, 49]. Therefore, we hypothesize that either sodium aluminate or β'' -Al₂O₃ forms before the onset of densification and that the presence of the

second phases on the surface of the Al₂O₃ particles retards the initial shrinkage of Na₂O-doped samples at \sim 1050°C. However, we did not observe any β -Al₂O₃ type grains in the samples at this temperature. Alternatively, as discussed below, Na₂O may interact with the 103 ppm of intrinsic SiO₂ in the sample.

We hypothesize that the initial grain boundaries in the as-received Al₂O₃ are wetted with the intrinsic impurities such as Na₂O, CaO, TiO₂ and SiO₂. Doping with Na₂O and SiO₂ changes the relative grain boundary chemistries and the properties of the respective grain boundary liquids. In the presence of a grain boundary liquid, densification occurs by a solution-precipitation sintering process, and thus, the rate of densification is controlled by either interface reaction between the grain boundary liquid and Al₂O₃ grains, or by the diffusion of Al³⁺ through the liquid grain boundary film. Al³⁺ diffusion is rate-limiting at 1525°C since it has been shown for molten glass systems that Al³⁺ has lower ionic diffusion rates than O²⁻ [50]. For diffusion-controlled densification, the densification rate is given by [51, 52]

$$\frac{d\left(\frac{\Delta\rho}{\rho}\right)}{dt} = \frac{A\delta D_l C_0 \gamma_{lv} \Omega}{kT} r_s^{-4} \quad (2.1)$$

and for interface reaction-controlled densification, the densification rate is given by

$$\frac{d\left(\frac{\Delta\rho}{\rho}\right)}{dt} = \frac{B K C_0 \gamma_{lv} \Omega}{kT} r_s^{-2} \quad (2.2)$$

where A and B are geometric factors, δ is the thickness of the liquid film, D_l is the diffusion coefficient of Al³⁺ in the liquid, C_o is the equilibrium solute concentration, K the interface reaction constant, γ_{lv} is the liquid surface tension, Ω is the molecular volume of the solid, r_s is the particle radius, k is the Boltzmann constant and T is absolute temperature.

Equations 2.1 and 2.2 can be used to gain insights into the rate-limiting densification mechanisms during liquid phase sintering by evaluating their ratio [51, 52]

$$\alpha = \frac{A\delta D_l}{B K} r_s^{-2} \quad (2.3)$$

In general, for $\alpha > 1$, densification is controlled by the interface reaction, since D_l is relatively high. For $\alpha < 1$, densification is controlled by diffusion, and for $\alpha = 1$ both mechanisms contribute equally to densification [52]. Since the product

of the grain boundary thickness and the diffusion coefficient greatly influences the rate-determining mechanism, δD_l and the interface reaction constant K were examined in more detail.

Due to the main impurities in Bayer aluminas being SiO_2 and Na_2O , the Al_2O_3 - SiO_2 - Na_2O ternary phase diagram [39] was utilized to evaluate the effects of dopant type and concentration on solubility of Al_2O_3 in the grain boundary liquid. It is assumed that the system approaches thermodynamic equilibrium upon holding at 1525°C, and thus the equilibrium composition of the liquid at 1525°C can be calculated from the ternary phase diagram (Figure 2.9). For simplification, we considered only Al_2O_3 , SiO_2 and Na_2O for the analysis, and assumed that all impurities/dopants are located in the grain boundaries. It was stated earlier that Na_2O is not soluble in Al_2O_3 , and it has been reported in the literature that SiO_2 segregates at the grain boundaries in Al_2O_3 [53]. Figure 2.9 shows the liquidus projection of the Al_2O_3 - SiO_2 - Na_2O ternary phase diagram. The red solid lines connecting the Al_2O_3 end member to the Na_2O - SiO_2 side are binary cuts through the ternary (isoplethal sections) and correspond to some of the $\text{Na}_2\text{O}/\text{SiO}_2$ ratios investigated in this study. The red dashed line is the isotherm at 1525°C for the part of the phase diagram where α - Al_2O_3 and liquid are in equilibrium. The blue dash-dot line and the green dotted line are eutectic lines along which β - Al_2O_3 or mullite is stable with α - Al_2O_3 and a liquid. The isotherm and the eutectic lines are important for determining the stable phases and the composition of the liquid in the samples. If a binary cut intersects the isotherm (red dashed line) only α - Al_2O_3 and liquid are stable phases at 1525°C and the intersection point determines the composition of the liquid. If a binary cut intersects one of the two marked eutectic lines (blue dash-dot or green dotted) a third phase (β - Al_2O_3 or mullite) is stable in those samples, and the composition of the liquid at 1525°C is determined by the intersection point of the respective intersected eutectic line with the isotherm at 1525°C.

The Al_2O_3 - SiO_2 - Na_2O phase diagram demonstrates that a small amount of liquid is stable at 1525°C for all compositions investigated. Note that these overall compositions are all very close to the Al_2O_3 end member ($\sim 99.8\%$ Al_2O_3) and Na_2O and SiO_2 are insoluble in Al_2O_3 . Isoplethal sections (red solid lines in Figure 2.9) can be used to determine the stability and equilibrium composition of a liquid since the volume fractions of Na_2O and SiO_2 are known. Lambotte and Chartrand [39]

calculated isoplethal sections of the ternary phase diagram, and based on their calculations, the solubility of Al_2O_3 in the liquid at 1525°C in the samples was estimated based on the respective $\text{Na}_2\text{O}:\text{SiO}_2$ ratios (assuming a constant liquid density of 2.45 g/cm³ [37, 54]). Likewise, the volume fractions of liquid and solid phases can be estimated since the doping and impurity concentrations of SiO_2 and Na_2O are known. Table 2.2 summarizes the stable phases, the liquid compositions, and the total amount of liquid in the as-received and doped samples. Stable liquids at 1525°C are predicted for liquid compositions with $\text{Na}_2\text{O}:\text{SiO}_2$ ratios between 0.25 and 0.5. As described above, for higher Na_2O concentrations in the samples (global $\text{Na}_2\text{O}:\text{SiO}_2$ ratio > 0.5), α - Al_2O_3 , β - Al_2O_3 and a liquid with a $\text{Na}_2\text{O}:\text{SiO}_2$ ratio of 0.5 are stable. For sample compositions with higher SiO_2 concentrations (global $\text{Na}_2\text{O}:\text{SiO}_2$ ratio < 0.25) α - Al_2O_3 , mullite and a liquid with a $\text{Na}_2\text{O}:\text{SiO}_2$ ratio of 0.25 are stable. Since the global $\text{Na}_2\text{O}:\text{SiO}_2$ ratio in most of the samples investigated in this work is either > 0.5 or < 0.25, the liquid in those samples had compositions of 0.5 or 0.25, respectively. As the $\text{Na}_2\text{O}:\text{SiO}_2$ ratio in the liquid increases from 0.25 to 0.5 the solubility of Al_2O_3 in the liquid increases from 18.4 vol.% to 21.6 vol.% [39]. The increased Al_2O_3 solubility leads to higher densification rates and higher densities in $\text{Na}_2\text{O}/\text{SiO}_2$ co-doped samples compared to singly SiO_2 -doped samples, regardless of the rate-limiting process.

Assuming fully dense samples and the liquid volume fractions reported in Table 2.2, we calculated the grain boundary thickness δ using:

$$\delta = 2 \frac{V_g \phi}{S_g (1 - \phi)} \quad (2.4)$$

where ϕ is the liquid volume fraction and V_g and S_g are the volume and the surface area based on the average grain size, respectively. For as-received and singly Na_2O -doped samples the grain boundary thickness is < 0.3 nm for all observed grain sizes. For $\text{Na}_2\text{O}/\text{SiO}_2$ co-doped samples (603 ppm SiO_2) the grain boundary thickness is between 0.8 and 1.8 nm for grain sizes of 1 μm and 2.5 μm , respectively. The calculated grain boundary thickness of singly SiO_2 -doped samples is similar to that of as-received samples, since mullite is predicted to form in the $\text{Al}_2\text{O}_3\text{-SiO}_2\text{-Na}_2\text{O}$ system for low Na_2O concentrations at 1525°C. However, mullite may not form in Bayer process Al_2O_3 due to the presence of other impurities, such as CaO , which, similar to Na_2O , lowers the eutectic temperature and acts as a network modifier

in the glass. Therefore, the grain boundary thicknesses of singly SiO_2 -doped and $\text{Na}_2\text{O}/\text{SiO}_2$ co-doped samples are expected to be similar at ~ 1.8 nm. The amount of liquid in the samples and, therefore, the grain boundary thickness, is governed mainly by the amount of glass forming species in the samples, i.e. SiO_2 .

The diffusion coefficient of Al^{3+} through the liquid grain boundary phase can be calculated with the Eyring relation

$$D_l = \frac{kT}{\eta\lambda} \quad (2.5)$$

where η is the viscosity of the grain boundary liquid and λ is the jump distance of the diffusion species, taken as the ionic diameter of an Al^{3+} (1.07 Å). Using viscosity data (range of 20 - 400 Pa·s) from the literature [55], we estimated the diffusion coefficients to be $\sim 1 \cdot 10^{-7}$ and $\sim 5 \cdot 10^{-9}$ cm 2 /s for $\text{Na}_2\text{O}/\text{SiO}_2$ co-doped and singly SiO_2 -doped samples, respectively.

Although we can calculate values for grain boundary thickness (δ) and viscosity (η), an exact α -ratio cannot be determined using Equation 2.3 because we do not know the interface reaction constant (K). Nevertheless, assuming a reasonable K value from the literature ($K = 5 \cdot 10^{-8}$ m/s) [52] and assuming that the A/B ratio (A and B being geometrical factors) is on the order of 1, we estimated α to be $\sim 10^{-2}$ and ~ 1 for singly SiO_2 -doped samples (603 ppm SiO_2) and $\text{Na}_2\text{O}/\text{SiO}_2$ co-doped samples (529/603 ppm), respectively. Thus, we conclude that at 1525°C densification of Bayer aluminas with low $\text{Na}_2\text{O}/\text{SiO}_2$ concentration ratios is governed by diffusion, whereas densification of Bayer aluminas with high $\text{Na}_2\text{O}/\text{SiO}_2$ concentration ratios can be governed by either diffusion or interface reaction.

The enhanced densification of $\text{Na}_2\text{O}/\text{SiO}_2$ co-doped samples compared to singly SiO_2 -doped is attributed to two factors; the increased solubility of Al_2O_3 in the liquid grain boundary phase, and the enhanced diffusion of Al^{3+} ($\sim 5 \cdot 10^{-9}$ to $\sim 1 \cdot 10^{-7}$ cm 2 /s) through the liquid grain boundary. This effect of enhanced densification of $\text{Na}_2\text{O}/\text{SiO}_2$ co-doped samples compared to singly SiO_2 -doped samples is observed in both the dilatometry curves and the densification kinetics data shown in Figure 2.2 and Figure 2.6, respectively.

It should be noted that a particular challenge for thermal processing studies with soda-based ceramics is Na_2O volatilization at relatively lower temperature than the sintering temperature. Soda by itself is highly volatile at temperatures

< 1000°C and the evaporation of soda from Na₂O containing technical ceramics such as sodium niobates [56] and β -Al₂O₃ during sintering is often reported. For example, β -Al₂O₃ (Na₂O·11Al₂O₃) has an appreciable Na₂O vapor pressure at temperatures > 1400°C [48], and when heated in air to > 1500°C, β -Al₂O₃ converts to α -Al₂O₃ by volatilization of Na₂O [48, 57]. Therefore, Na₂O evaporation from the samples during heating should be considered as samples might have somewhat lower Na₂O concentrations than assumed for the above calculations. Thus, for samples with low Na₂O/SiO₂ ratios, the liquid grain boundary phase may contain somewhat less Na₂O and the grain boundary thickness may be somewhat less than calculated. However, for singly Na₂O-doped samples and for co-doped samples with high Na₂O/SiO₂ ratios (e.g. Na₂O \geq 529 ppm for samples with 603 ppm SiO₂) the composition of the grain boundary liquid and the grain boundary thickness is not expected to change very much if Na₂O volatilizes. Consequently, even with Na₂O volatilization, the proposed sintering mechanisms do not change. The evaporation of Na₂O from Bayer Al₂O₃ samples will be further discussed in more detail in the following chapter.

2.5 Summary

High concentrations of Na₂O in Bayer process Al₂O₃ powders inhibit densification in the initial sintering stage and retard densification up to the final sintering stage compared to powders with low Na₂O concentrations. However, Na₂O shows no adverse effect on the final density after longer hold times (\geq 3 h at 1525°C). The addition of SiO₂ to Bayer process Al₂O₃ powders substantially retards densification, starting at \sim 1250°C, and samples containing as much as 603 ppm SiO₂ are 4% less dense than samples containing 103 ppm SiO₂, even after hold times as long as 8 h at 1525°C. Co-doping with Na₂O and SiO₂ increases densification by 1 - 2.5% relative density relative to singly SiO₂-doped samples. The observed differences in sintering behavior can be explained by a liquid phase sintering model. Diffusion and solubility of Al₂O₃ in the SiO₂-based liquid in the grain boundaries is low at the temperatures used in this study, which explains the substantial retardation of densification by SiO₂. As predicted from the phase diagram Na₂O increases the solubility of Al₂O₃ in the siliceous grain boundary phase. As predicted from viscosity data Na₂O enhances diffusion of Al³⁺ through the liquid grain boundary

phase. Both factors contribute to the enhanced densification rates of samples with high $\text{Na}_2\text{O}/\text{SiO}_2$ ratios compared to samples with low $\text{Na}_2\text{O}/\text{SiO}_2$ ratios.

Table 2.1. Physical and chemical characteristics of the as-received Bayer Al₂O₃ powder used in this study.

BET (m ² /g)	7.4
D ₅₀ (μm)	0.4
D ₉₀ (μm)	1.5
	ICP (ppm)
Al ₂ O ₃	99.96 %
SiO ₂	103
Na ₂ O (total)	29
Fe ₂ O ₃	90
CaO	62
TiO ₂	22
MgO	2

Table 2.2. Calculated compositions and amounts of liquid in as-received, singly doped and co-doped samples at 1525°C ($\alpha = \alpha\text{-Al}_2\text{O}_3$, $\beta = \beta\text{-Al}_2\text{O}_3$, L = liquid, M = mullite).

Global dopant concentration		Global Na ₂ O/SiO ₂ ratio	Na ₂ O:SiO ₂ ratio in liquid	Composition of liquid (mol %)			Amount of liquid (vol. %)	Stable phases
ppm (wt.)	ppm (mol)			Na ₂ O	SiO ₂	Al ₂ O ₃		
Na ₂ O/SiO ₂	Na ₂ O/SiO ₂							
As-received 29/103	48/175	0.27	0.25	17.9	63.4	19.7	0.03%	$\alpha + L$
154/103- 1029/103	253/175- 1693/175	1.45-9.67	0.5	26.1	52.3	21.6	0.03%	$\alpha + L + \beta$
29/603	48/1023	0.05	0.25	16.3	65.3	18.4	0.03%	$\alpha + L + M$
154/603	253/1023	0.25	0.25	16.3	65.3	18.4	0.16%	$\alpha + L$
279/603	459/1023	0.45	0.45	24.5	54.6	20.8	0.19%	$\alpha + L$
529/603	870/1023	0.85	0.5	26.1	52.3	21.6	0.22%	$\alpha + L + \beta$
1029/603	1693/1023	1.65	0.5	26.1	52.3	21.6	0.22%	$\alpha + L + \beta$

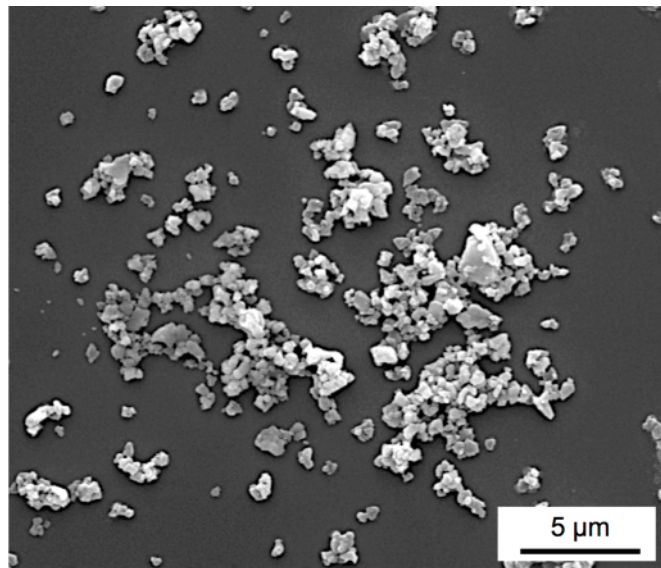


Figure 2.1. SEM image of as-received chemically purified Bayer Al_2O_3 powder used in this study.

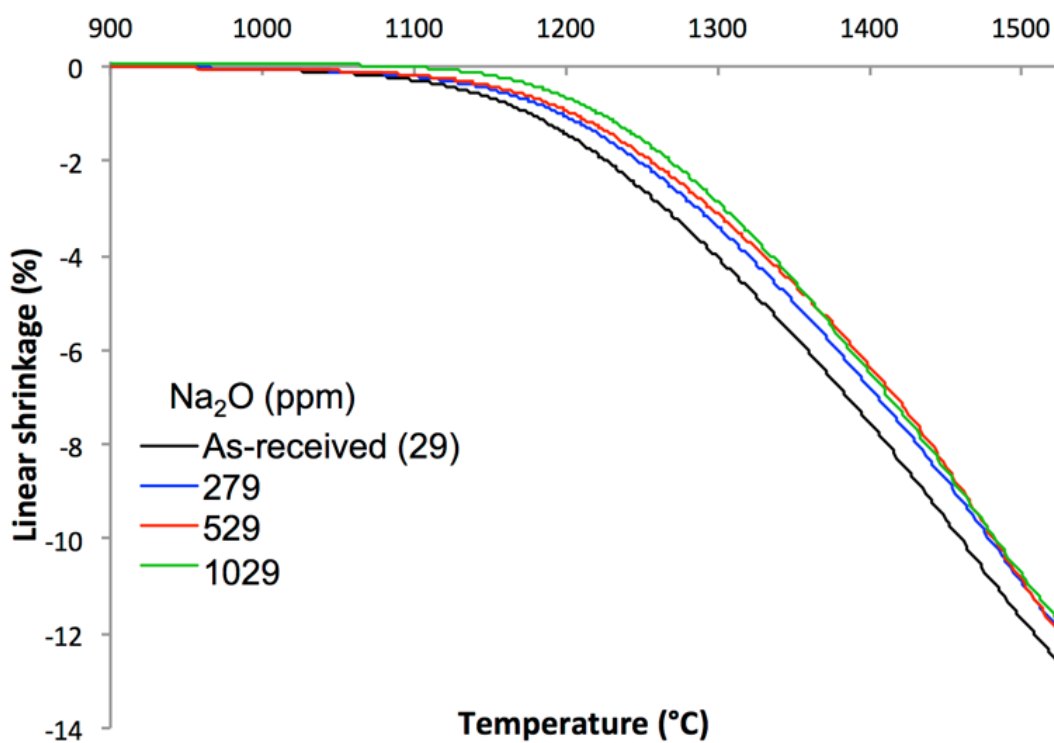


Figure 2.2. Dilatometer curves of as-received and singly Na_2O -doped samples heated at $10^{\circ}\text{C}/\text{min}$ to 1525°C .

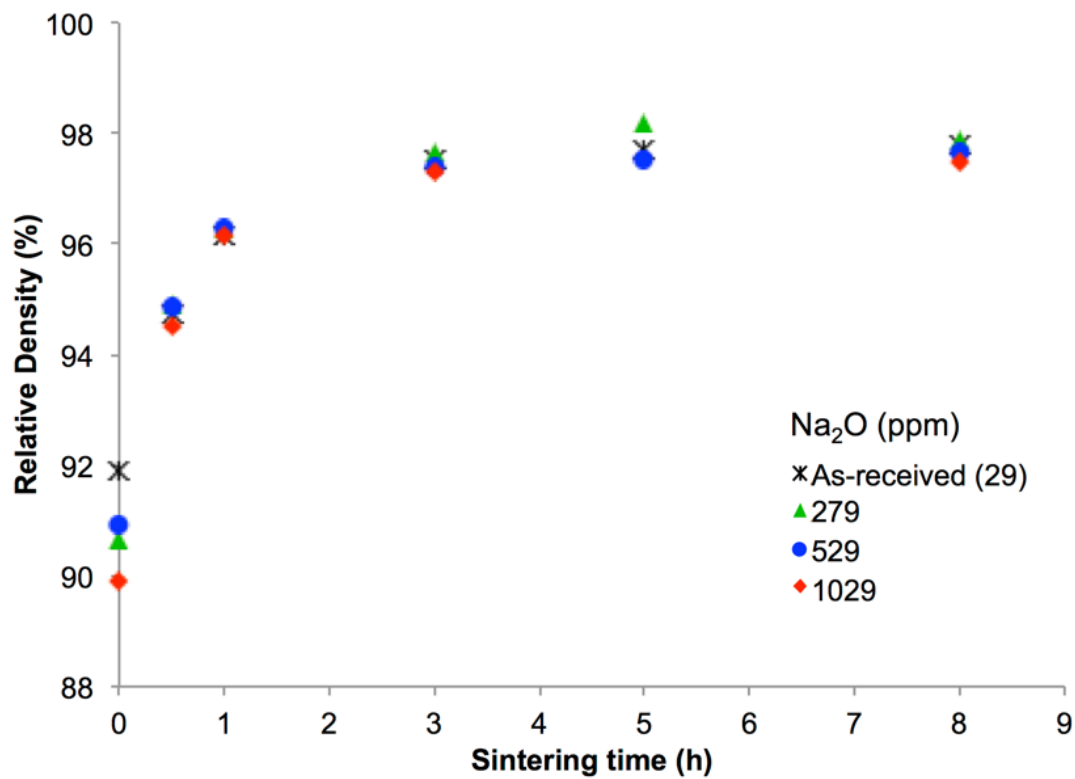


Figure 2.3. Densification kinetics of Bayer Al_2O_3 doped with different Na_2O concentrations and sintered at 1525°C .

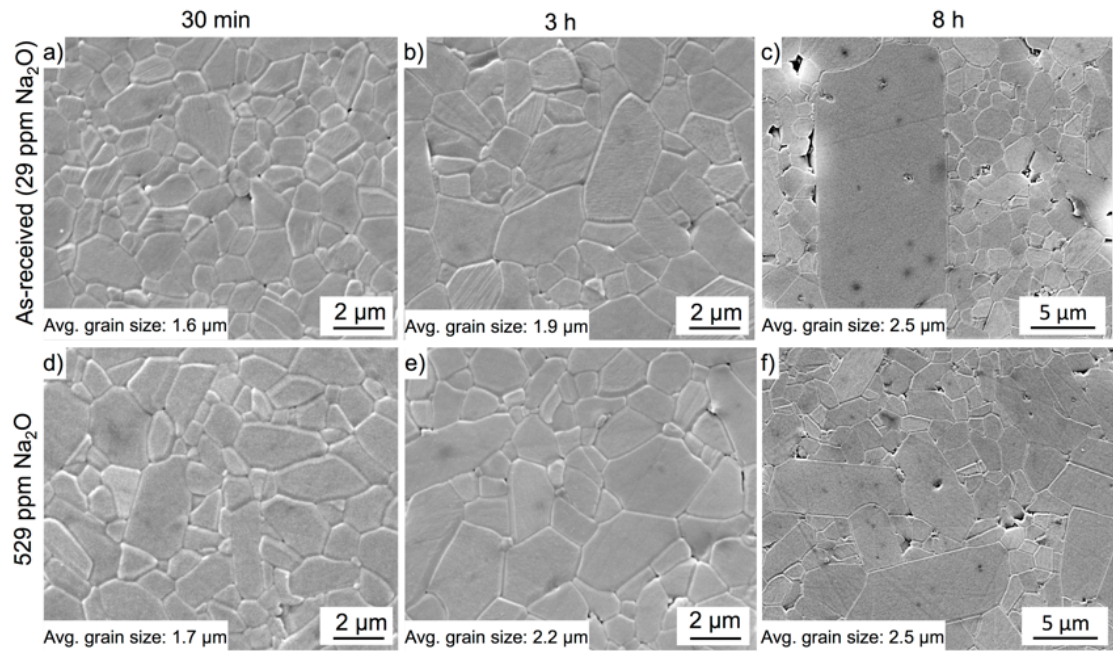


Figure 2.4. Microstructures of as-received and singly 529 ppm Na₂O doped samples after 30 min, 3 h and 8 h at 1525°C.

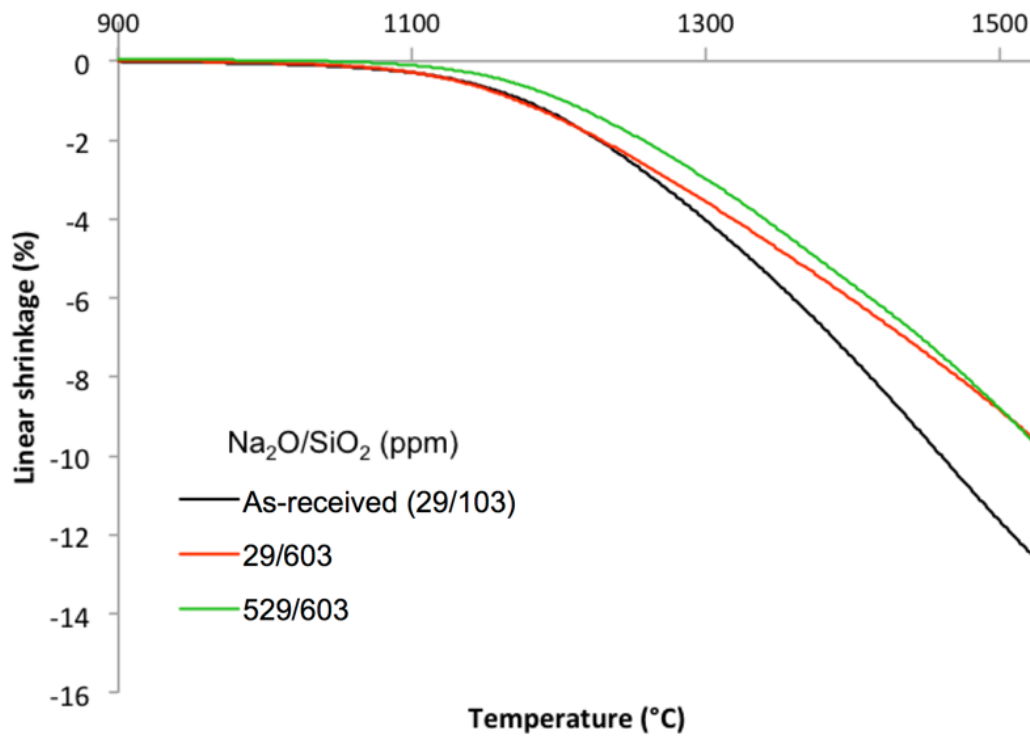


Figure 2.5. Dilatometer curves of as-received, singly SiO_2 -doped, and $\text{Na}_2\text{O}/\text{SiO}_2$ co-doped Bayer Al_2O_3 heated at $10^\circ\text{C}/\text{min}$ to 1525°C .

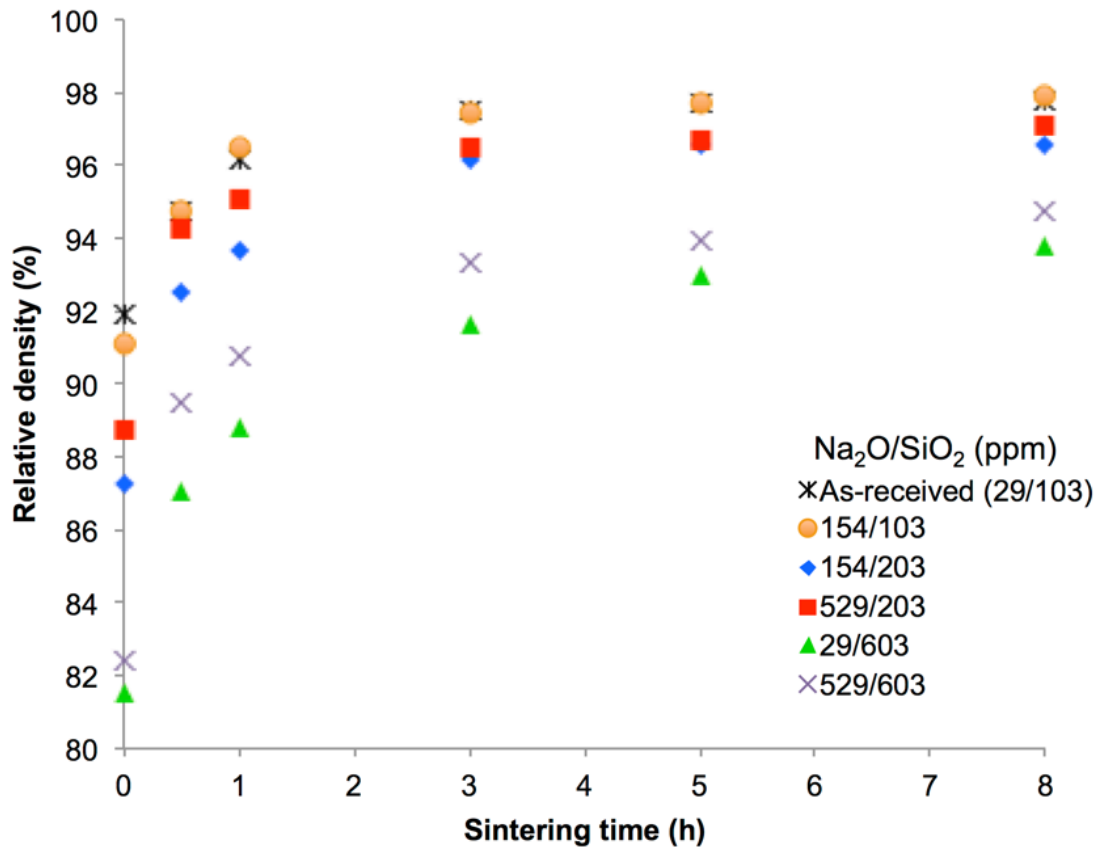


Figure 2.6. Densification kinetics of Bayer Al_2O_3 doped with different concentrations of Na_2O and SiO_2 at 1525°C .

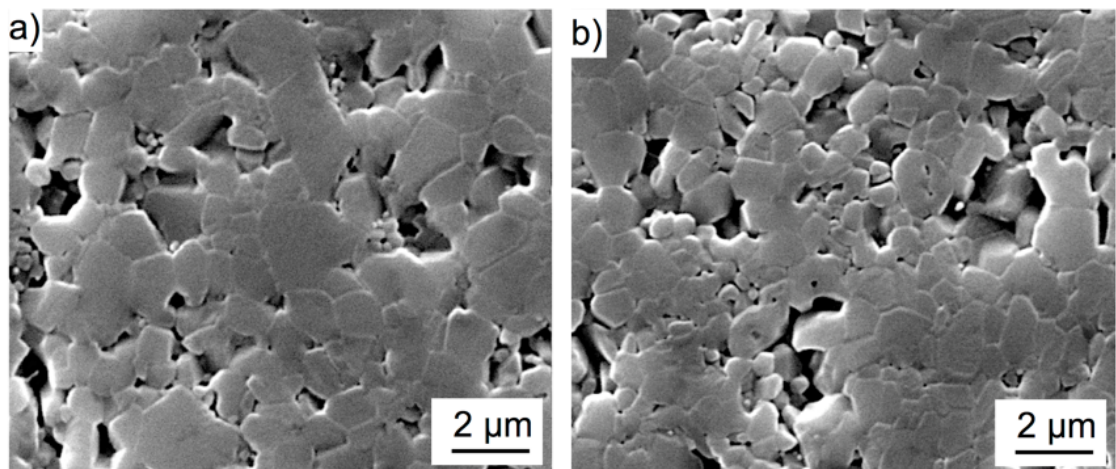


Figure 2.7. Microstructures of Bayer Al_2O_3 doped with a) 603 ppm SiO_2 and b) 529 ppm Na_2O and 603 ppm SiO_2 after heating at 1525°C for 8h.

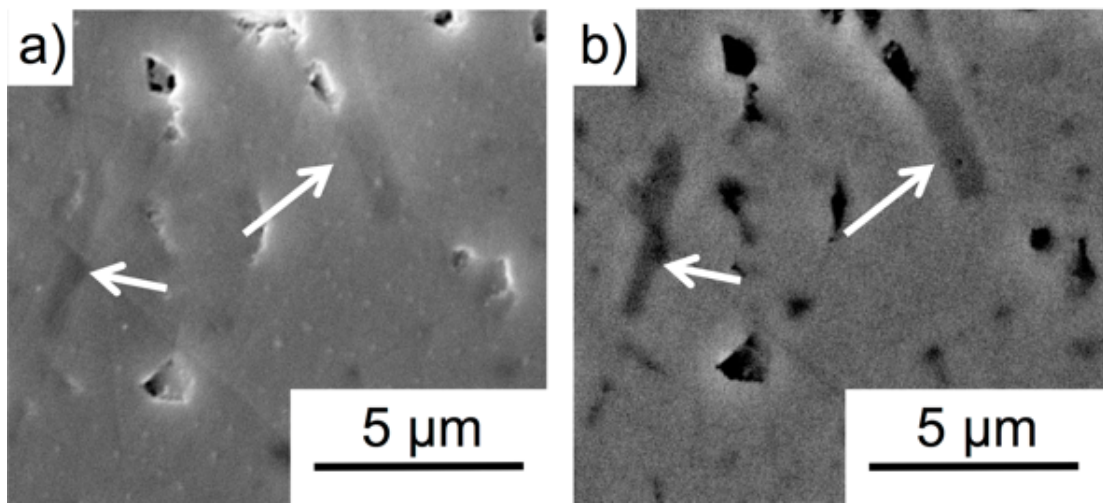


Figure 2.8. Micrographs of a sample doped with 1029 ppm Na_2O after sintering at 1525°C for 3 h. The micrographs were recorded using a) a secondary electron detector and b) a backscattered electron detector. The arrows point at the platelet shaped β -alumina grains that form in samples doped with Na_2O . The samples were not thermally etched.

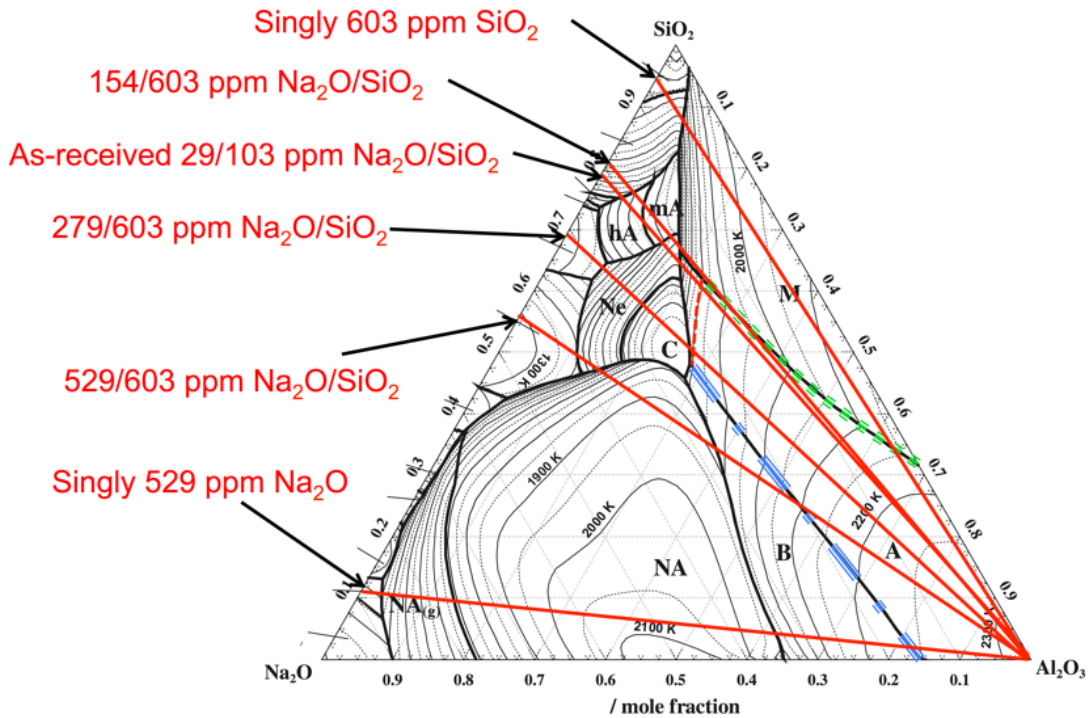


Figure 2.9. Liquidus projection of the Al_2O_3 - SiO_2 - Na_2O ternary phase diagram. The red solid lines are isoplethal cuts representing the samples investigated in this study. The red dashed line is the 1525°C isotherm where $\alpha\text{-Al}_2\text{O}_3$ and liquid are in equilibrium. The blue dash-dot line and green dotted line are eutectic lines at which $\alpha\text{-Al}_2\text{O}_3$ and liquid is in equilibrium with $\beta\text{-Al}_2\text{O}_3$ or mullite, respectively.

Chapter 3 | Powder Chemistry Effects on the Sintering Behavior of MgO- doped Bayer Alumina

3.1 Introduction

Most commercial alumina products use Bayer processed powder because it is a lower cost option for products with purity levels of up to 99.9%. The remaining 0.1% consists of the intentionally added MgO dopant, and impurities such as Na₂O, CaO, Fe₂O₃, and SiO₂ that originate from the bauxite ore or the Bayer process itself. It is well known that trace (ppm) amounts of dopants or impurities can have a significant influence on the sintering of alumina [14, 15, 58]. Since Coble's discovery of MgO doping to produce high-density translucent alumina, there has been high academic and commercial interest in understanding how small concentrations of dopants and impurities characteristic of Bayer alumina affect sintering [8, 10, 12, 35, 59].

In chapter 2, the influence of Na₂O and SiO₂ on the sintering of MgO-free Bayer alumina was investigated. Na₂O was shown to initially retard the densification of MgO-free Bayer alumina samples, but no effect was observed after extended sintering time (> 30 min) at 1525°C, whereas the addition of SiO₂ to MgO-free Bayer alumina formed a liquid phase and significantly retarded densification throughout the entire sintering process. Na₂O addition to SiO₂-doped samples increased the densification rate and degree of densification compared to singly SiO₂-doped samples. Based on phase equilibria, the solubility of Al₂O₃ in the liquid phase was shown to increase as

the Na_2O concentration in the liquid grain boundary phase increases. Furthermore, a higher Na_2O concentration decreases the viscosity of the liquid phase, which further increases the densification rate [3]. Hence, samples with high $\text{Na}_2\text{O}/\text{SiO}_2$ ratios (≥ 0.5) have higher densities than samples with lower $\text{Na}_2\text{O}/\text{SiO}_2$ ratios.

MgO is commonly added to commercial alumina powders because it is known to improve sintering. Several reasonable mechanistic explanations for the beneficial effect of MgO include solute-drag, particle-pinning, modification of defect chemistry, increase of surface diffusivity, modification of a liquid phase, and modification of interfacial properties [15]. A model that takes into account the redistribution of MgO and SiO_2 during the sintering of high purity alumina was reported by Handwerker et al. [16] They proposed that MgO changes the segregation behavior of glass forming impurities such as SiO_2 by increasing their solubility in Al_2O_3 . This mechanism was supported by the work of Gavrilov et al. [2] who demonstrated by high resolution secondary ion mass spectrometry that the dopants segregate strongly to grain boundaries when high purity Al_2O_3 is singly doped with either SiO_2 or MgO , but show a higher solubility in Al_2O_3 when co-doped with MgO and SiO_2 due to a defect mechanism in which Mg^{2+} and Si^{4+} occupy Al^{3+} sites and compensate for each other's charge and strain. This model is of particular interest since it considers the direct interaction of MgO and SiO_2 ; an impurity known to negatively affect alumina densification.

In this chapter it is reported how Na_2O and SiO_2 influence the sintering of 99.8 - 99.9% pure Bayer alumina doped with 380 ppm MgO . Dilatometry and sintering kinetics of MgO -free Bayer alumina samples with similar Na_2O and SiO_2 concentrations from chapter 2 are compared to the present results to identify the stages at which MgO affects densification, and to identify key mechanisms that are responsible for the beneficial effect of MgO on the sintering of Bayer alumina. High-resolution transmission electron microscopy (TEM) and energy dispersive spectroscopy (EDS) measurements show the distribution of dopants/impurities on grain boundaries. First-principles calculations based on the density functional theory (DFT) were carried out to estimate the relative thermodynamic stability of MgO , SiO_2 , and $\text{MgO}+\text{SiO}_2$ in the alumina lattice.

3.2 Experimental

A chemically purified MgO-doped Bayer alumina powder (Almatis, Inc., Leetsdale, PA, USA) was chosen for this study. Earlier we studied the influence of SiO₂ and Na₂O on the sintering of MgO-free Bayer alumina using a powder with similar physical and chemical characteristics as the powder used in this study. Since the sample preparation procedures of the two powders were identical, the differences in sintering behavior after doping with similar Na₂O and SiO₂ concentrations should be attributable primarily to the difference in MgO concentration and its cross effects with Na₂O and SiO₂.

Physical and chemical characteristics of the powder are shown in Table 3.1 and Figure 3.1. The powder was doped with up to 1000 ppm Na₂O and 500 ppm SiO₂ using sodium acetate (NaC₂H₃O₂·3H₂O, ACS grade, BDH, VWR International LLC, West Chester, PA, USA) and tetraethyl orthosilicate (Si(OC₂H₅)₄), 98%, Aldrich Chemical Company, Inc. Milwaukee, WI, USA), respectively, to obtain chemistries similar to commercial high purity Bayer aluminas with different liquid volume fractions and different Na₂O/SiO₂ ratios, as shown in Table 3.2. The amount of liquid in the samples at 1525°C was estimated from the Al₂O₃-Na₂O-SiO₂ and Al₂O₃-MgO-SiO₂ phase diagrams [3, 39, 60] based on the concentrations of SiO₂, Na₂O and MgO. The detailed doping procedures are described in chapter 2.

Samples with green densities of 59.0 ± 0.5% were fabricated for sintering studies by uniaxial and cold isostatic dry pressing (CIP, Autoclave engineers, Erie, Pa, USA) at 170 MPa and 200 MPa, respectively. The dry pressed cylinders were heated at 10°C/min to 1525°C in a thermomechanical analyzer (TMA, Linseis PT1600, Robbinsville, NJ, USA) to record the shrinkage during heating. The kinetics of sintering of samples at 1450°C and 1525°C were investigated for up to 8 h. The samples were heated at 10°C/min to 1200°C and then at 5°C/min to the final sintering temperature. The average grain size and density were measured by the linear intercept (ASTM Standard E112-96) [37] and Archimedes methods (ASTM standard B962-15) [36], respectively. The structure and chemistry of grain boundaries were investigated by transmission electron microscopy (TEM) and energy dispersive x-ray spectroscopy EDS using a dual aberration corrected FEI Titan³ field emission microscope operated at 300 kV and FEI Talos (FEI, Hillsboro, OR, USA) field emission microscope at 200 kV. The EDS on both microscopes is

an FEI Super-X system consisting of four SDDs (Silicon Drift Detectors) with a solid angle of 0.9 sr ad. The samples for TEM and EDS were air-quenched from the sintering temperature by pulling the samples out of the box furnace at temperature and prepared using a focused ion beam (Quanta 200 3D Dual Beam FIB, FEI, Hillsboro, OR, USA). Grain boundaries were chosen for analysis that were oriented parallel to the TEM beam in order to accurately measure grain boundary widths in the 2D projection images and EDS profiles. Chemical analyses were performed by inductively coupled plasma (ICP) emission spectroscopy (iCap 6000, Thermo Fischer Scientific, Inc., Waltham, MA, USA) after alumina samples were acid digested in a microwave digestion unit equipped with a TeflonTM sample holder (MARS M, CEM Corp., Matthews, NC, USA).

3.3 Computational Methodology

DFT-based first-principles calculations were carried out at 0 K to investigate the thermodynamic stability of clustered defects in the α -alumina structure. The energy at 0 K without the contribution of the zero-point vibrational energy E_0 was obtained by an equation of state (EOS) fitting using the four-parameter Birch-Murnaghan (BM4) equation as follows [61]:

$$E_0(V) = a + bV^{-\frac{2}{3}} + cV^{-\frac{4}{3}} + dV^{-2} \quad (3.1)$$

where a , b , c , and d are fitting parameters. The EOS fitting is achieved through an energy-volume (E-V) curve of at least 5 different volumes based on the methodology discussed by Shang et al. [61]. The Helmholtz energy $F(V, T)$ can be predicted as a function of temperature T and volume V via [61, 62]:

$$F(V, T) = E_0(V) + F_{vib}(V, T) + F_{T-el}(V, T) \quad (3.2)$$

where F_{vib} is the temperature-dependent vibrational contribution, and F_{T-el} is the thermal electronic contribution. At ambient pressure, the Helmholtz energy of the system is equal to the Gibbs energy.

The vibrational contribution was obtained using the Debye-Grüneisen model [61]:

$$F_{vib}(V, T) = \frac{9}{8}k_B\theta_D(V) - k_BT \left[D \left(\frac{\theta_D(V)}{T} \right) + 3\ln \left(1 - e^{-\theta_D(V)/T} \right) \right] \quad (3.3)$$

where θ_D is the Debye temperature, T the temperature, and $D[\theta_D(V)/T]$ the Debye function. The Debye temperature can be calculated by:

$$\theta_D = s \frac{(6\pi^2)^{\frac{1}{3}}\hbar}{k_B} V_0^{\frac{1}{6}} \left(\frac{B_0}{M} \right)^{\frac{1}{2}} \left(\frac{V_0}{V} \right)^\gamma \quad (3.4)$$

where s is the Debye temperature scaling factor, γ the Grüneisen parameter determined by the pressure derivative of bulk modulus B' , B_0 the equilibrium bulk modulus, M the atomic mass, and V_0 the equilibrium volume. Here, the equilibrium properties V_0 , B_0 , and B' are estimated from the EOS of Eq. 3.1. The methodology by Liu et al. [63] was used to calculate the scaling factor of Al₂O₃:

$$s(\nu) = 3^{\frac{5}{6}} \left(4\sqrt{2} \left(\frac{1+\nu}{1-\nu} \right)^{\frac{3}{2}} + \left(\frac{1+\nu}{1-\nu} \right)^{\frac{3}{2}} \right)^{-\frac{1}{3}} \quad (3.5)$$

where ν is the Poisson's ratio, which was calculated by Shang et al. [64]. The thermal electronic contribution was estimated based on the electronic density of states and the Fermi-Dirac statistics [62].

In the present work, the Vienna Ab-initio Simulation Package (VASP) was used to perform the first-principles calculations [65]. The projector augmented-wave (PAW) [66, 67] method was utilized to describe the electron-ion interactions with the exchange correlation functional given by the generalized gradient approximation (GGA-PW91) [68]. A sigma value of 0.2 eV and a plane wave energy cutoff of 1.3 times higher than the highest default cutoff were adopted, which was 520 eV. The Brillouin zone sampling was carried out with Blöchl corrections using a gamma centered Monkhorst-Pack (MP) scheme [67, 69]. The automated k-points grid generator in VASP was employed with a subdivision length of 80. The k-points generated by VASP for these calculations was 19x19x6. The energy convergence criterion of the electronic self-consistency was set at 10⁻⁵ eV/atom for all calculations.

The energies of charge, site, and mass balanced defects in α -alumina were calculated for defect clusters, i.e. the defects are located next to each other, since

this has been shown to be the most stable configuration [70]. The geometric arrangements of each of the clusters were chosen based on previous computational work. Multiple authors showed that a 30-40 atom supercell of Al_2O_3 is sufficient to calculate non-charged defects [70–74]. Multiple authors have studied charged and clustered defects in Al_2O_3 [70–74]. They showed that different geometric arrangements and supercell size result in little difference in energy and that the impurity atoms prefer to be clustered due to the binding energy [70–74]. Using this methodology, supercells were generated in the present work with Mg and/or Si clustered, i.e. the Mg-cluster having two Mg atoms substituted for two Al atoms and an oxygen vacancy as nearest neighbors, the Si-cluster having three Si atoms substituted for three Al atoms and an Al vacancy, and the Mg+Si-cluster having one Mg and one Si substituted for two Al atoms.

3.4 Sintering and Microstructure Analysis

In chapter 2, it was shown that a glass phase can form during sintering of Bayer alumina. Table 3.2 shows the amounts of liquid in the samples at 1525°C estimated from the $\text{Al}_2\text{O}_3\text{-Na}_2\text{O}\text{-SiO}_2$ and $\text{Al}_2\text{O}_3\text{-MgO}\text{-SiO}_2$ phase diagrams based on the amount of SiO_2 , Na_2O and MgO [60]. It should be noted that it was proposed in the literature [75] that the composition of the glass in grain boundaries can deviate from the bulk glass composition predicted from the phase diagram. Therefore, the estimations from the phase diagram are approximations. It can be seen that the glass volume fraction increases from 0.03 vol.% for SiO_2 concentrations of 82 ppm to 0.21 vol.% for SiO_2 concentrations of 582 ppm at 1525°C.

Figure 3.2 shows the dilatometry curves of MgO-doped and MgO-free samples with different Na_2O and SiO_2 concentrations heated at 10°C/min to 1525°C. For samples with SiO_2 concentrations of 582 ppm the estimated amount of liquid increases from 0.18 vol.% to 0.21 vol.% during heating from 1250°C to 1525°C, and for samples with 82 ppm SiO_2 the amount of liquid phase is estimated from the phase diagram to increase from 0.026 vol.% to 0.030 vol.% during heating from 1250°C to 1525°C.

Figure 3.2a shows that the onset of densification (taken as the temperature at which the sample shrinkage is 0.1%) of MgO-doped specialty alumina is shifted from ~1050°C for samples with 60 ppm Na_2O to ~1100°C for samples with 560

ppm Na₂O. Samples with 560 ppm Na₂O shrink 1% less than samples with 60 ppm Na₂O after heating to 1525°C. In both the MgO-doped and the MgO-free powders, higher SiO₂ concentrations retard densification at ~1250°C. However, the retardation caused by higher SiO₂ concentrations is less severe in the MgO-doped powder than in the MgO-free powder; e.g. already at 1300°C, MgO-doped powder samples with 582 ppm SiO₂ (after the addition of 500 ppm SiO₂) shrink 0.2% less and are 0.5% less dense than samples with 82 ppm SiO₂, whereas samples of the MgO-free powder with 603 ppm SiO₂ shrink 0.5% less and are 3.2% less dense than samples with 103 ppm SiO₂. After reaching 1525°C the dilatometry curves show that MgO-doped samples with 582 ppm SiO₂ (0.21 vol.% glass) shrink 1.8% less and are 5.4% less dense than MgO-doped samples with 82 ppm SiO₂ (0.03 vol.% glass). In contrast, the retardation of densification caused by the addition of 500 ppm SiO₂ to the MgO-free powder results in 3.0% less linear shrinkage and 8.7% lower relative densities after heating to 1525°C. MgO-doped (380 ppm) powder samples with 560 ppm Na₂O and 582 ppm SiO₂ shrink ~2.5% less than samples with 60 ppm Na₂O and 82 ppm SiO₂ after reaching 1525°C, and MgO-free powder samples with 529 ppm Na₂O and 603 ppm SiO₂ shrink ~3.0% less than samples with 29 ppm Na₂O and 103 ppm SiO₂ after reaching 1525°C.

Figure 3.3a and b show how the sintering kinetics of MgO-doped and MgO-free alumina are affected by Na₂O and SiO₂ after heating at 1450°C and 1525°C for up to 8 h. The density of samples with higher SiO₂ concentrations, i.e. higher glass concentrations, is lower for all hold times at 1450°C and 1525°C. At 1450°C MgO-doped powder samples with 0.19 vol.% glass phase (582 ppm SiO₂) are 6-7% less dense than samples with 0.027 vol.% glass phase (82 ppm SiO₂), for all hold times (Figure 3.3a). At 1525°C MgO-doped powder samples with 0.21 vol.% glass phase are ~11% and ~2% less dense than samples with 0.03 vol.% glass phase after heating for 0 h and 8 h, respectively, and samples with 0.03 vol.% glass phase reach densities >98% after 1 h, whereas samples with 0.066 and 0.21 vol.% glass phase are only ~96% and ~94% dense, respectively (Figure 3.3b).

The effect of Na₂O concentration on densification strongly depends on glass phase concentration. In all samples a higher Na₂O concentration initially retards densification. For example, after 0 h at 1450°C the relative density of samples with 0.03 vol.% glass phase and 560 ppm Na₂O is ~3% lower than the relative density of samples containing the same amount of glass phase and 60 ppm Na₂O. However,

there is no difference in sintered density after 3 h at either 1450°C or 1525°C. For samples with higher glass phase concentrations (e.g., 0.21 vol.%) the effect of Na₂O on the densification is more complicated, due to the changing Na₂O/SiO₂ ratio from 0.1 to 0.9 (Table 3.2). Samples with 0.21 vol.% glass phase and Na₂O/SiO₂ ratios of 0.9 are 1-2% denser than samples with 0.21 vol.% glass phase and Na₂O/SiO₂ ratios of 0.1. However, after 30 min at 1525°C the relative density of samples with 0.21 vol.% glass phase and Na₂O/SiO₂ ratios of 0.9 in the glass phase is 0.9% lower than the relative density of samples with 0.21 vol.% glass phase and Na₂O/SiO₂ ratios of 0.1 in the glass phase, and after 1 h or longer at 1525°C there is no difference in relative density. Samples with 0.066 vol.% glass phase are 98.3 - 98.6% dense after 8 h at 1525°C, and samples with 0.21 vol.% glass phase are 97.1% - 97.5% dense after 8 h at 1525°C.

Comparing the as-received MgO-free and MgO-doped powders with 0.03 vol.% glass phase shows that doping with 380 ppm MgO leads to 1% higher densities for all hold times at 1525°C (Figure 3.3b and c). After 8 h at 1525°C the MgO-doped samples with 0.21 vol.% glass phase are ~2% less dense than samples with 0.03 vol.% glass phase, whereas the addition of 500 ppm SiO₂ (total of 603 ppm SiO₂ and 0.22 vol.% glass) to the MgO-free powder leads to ~4% less dense samples. MgO-free and MgO-doped Bayer alumina samples containing 0.22 and 0.21 vol.% glass phase, respectively, and global Na₂O/SiO₂ ratios of 0.9 show initial retardation of densification compared to samples with Na₂O/SiO₂ ratios of 0.1, but have higher densities than samples with Na₂O/SiO₂ ratios of 0.1 after further heating. This increased densification can be explained by the increased solubility of Al₂O₃ into the liquid grain boundary phase and the higher diffusivity (lower viscosity of the grain boundary phase) as the Na₂O/SiO₂ ratio increases [3,52]. However, after hold times of 1 h or longer at 1525°C, MgO-free powder samples with 0.22 vol.% glass phase and Na₂O/SiO₂ ratios of 0.9 are 1% denser than samples with 0.22 vol.% glass phase and Na₂O/SiO₂ ratios of 0.1, whereas MgO-doped powder samples with 0.21 vol.% and Na₂O/SiO₂ ratios of 0.9 have the same densities as samples with 0.21 vol.% glass phase and Na₂O/SiO₂ ratios of 0.1.

The microstructures of samples with different vol.% glass phase and different Na₂O/SiO₂ ratios heated at 1525°C for 8 h are shown in Figure 3.4. Samples with 60 ppm Na₂O show mostly equiaxed grains, regardless of the glass phase concentration in the samples (Figures 3.4a and c). Samples with 560 ppm Na₂O

(Figures 3.4b and d) show more faceted α -Al₂O₃ grains and appear to have a wider grain size distribution than samples with 60 ppm Na₂O. These effects are more pronounced in samples with higher glass concentrations. The grain sizes of samples with 0.21 vol.% glass are less than the grain sizes of samples with 0.03 vol.% glass phase.

The average grain sizes of samples with different vol.% glass phase and different Na₂O/SiO₂ ratios are plotted as a function of relative density in Figure 3.5. Grain growth starts when the final sintering stage is reached, between 85 and 92% relative density. Samples with 0.03 vol.% glass phase and 60 ppm Na₂O show a three-fold increase in grain size, from 0.5 μ m to \sim 1.5 μ m, when the relative density increases from 68% to 99%, and samples with 0.03 vol.% glass phase and 560 ppm Na₂O have a somewhat larger grain size of 2.2 μ m at 99% relative density. When relative densities of \sim 99% are reached in samples with 0.03 vol.% glass, the grain size increases to 3.1 - 3.4 μ m when heated at 1525°C for 8 h. Samples with higher glass concentrations have a similar trajectory up to 92% density. However, at densities $>$ 92% the grain size of samples with higher glass phase concentrations increases stronger at lower densities compared to samples with lower densities. For example, 97.0-97.5% dense samples with glass phase concentrations of 0.21 and 0.17 vol.% have grain sizes of 2.6 and 2.4 μ m, respectively, whereas samples with glass phase concentrations of 0.03 vol.% have a grain size of 1.5 μ m at the same relative density.

3.5 Mechanistic Interpretation

If the mechanism of MgO increasing the solubility of SiO₂ in alumina, as proposed by Handwerker et al. [16], is responsible for the improved sintering behavior of alumina, then the amount of liquid phase in MgO-doped alumina should be less than calculated and less than in MgO-free samples, and, the grain boundary thickness in MgO-doped alumina should be less than in MgO-free powder. The reduced grain boundary thickness in MgO-doped alumina should lead to a change in grain boundary chemistry and different sintering behavior after this co-dissolution has occurred compared to MgO-free alumina.

Comparing the dilatometry curves and sintering kinetics of MgO-doped and MgO-free Bayer alumina powders with different chemistries shows that there are two stages at which MgO affects densification. At 1250°C increased SiO₂ concentrations

retard densification, and at the same stage there is an enhancement of densification due to MgO. This suggests that there is a direct interaction between SiO₂ and MgO at this stage, where MgO mitigates the negative effect of SiO₂. In ultrahigh purity alumina SiO₂ has been reported to decrease the concentration of Al interstitials and O vacancies, which decreases the diffusion rate during intermediate stage sintering (>1200°C) [76]. However, a liquid phase forms during the sintering of Bayer alumina at temperatures as low as 1200°C due to the presence of other impurities and dopants such as Na₂O and MgO. Therefore, Bayer alumina densifies by liquid phase sintering. The Al₂O₃-SiO₂-MgO phase diagram suggests that MgO increases the solubility of Al₂O₃ in the liquid, and MgO can lower the viscosity of the glass melt [55], which results in higher diffusion coefficients. The enhanced diffusion associated with the lower viscosity and higher solubility of Al₂O₃ in the glass phase can explain why MgO positively affects the sintering of alumina at stages when SiO₂ would negatively affect densification.

The second stage at which MgO affects densification is after 1 h at 1525°C. MgO-free powder samples with 0.22 vol.% glass phase and Na₂O/SiO₂ ratios of 0.9 have 1-2% higher relative densities than samples with 0.22 vol.% glass phase and Na₂O/SiO₂ ratios of 0.1 for all hold times at 1525°C. In previous work we calculated an expected grain boundary thickness of 1.3 nm for samples with 0.22 vol.% glass phase after 3 h at 1525°C, based on the observed grain size of 1.6 μm assuming spherical monodispersed grains as an approximation.. The addition of 500 ppm Na₂O increases the Na₂O/SiO₂ ratio from 0.1 to 0.9, which modifies the liquid grain boundary phase and enhances densification as shown in Chapter 2. Figure 3.6 shows a high-resolution TEM image of a grain boundary of a MgO-free powder sample (2 ppm MgO) with 0.22 vol.% glass phase and a Na₂O/SiO₂ ratio of 0.9 after 3 h at 1525°C. It can be seen that the measured grain boundary thickness of 1.7 nm is close to the grain boundary thickness calculated based on the amount of glass phase in the sample. MgO-doped powder samples with 0.21 vol.% glass phase and Na₂O/SiO₂ ratios of 0.9 have 1-2% higher densities than samples with 0.21 vol.% glass phase and Na₂O/SiO₂ ratios of 0.1 for most hold times at 1450°C and for hold times < 30 min at 1525°C. This difference in densification behavior is similar to the densification behavior of MgO-free powder samples, which suggests the presence of a liquid phase that is modified by Na₂O, as seen in the MgO-free alumina samples.

Figure 3.7a shows a high resolution TEM image of a grain boundary in an MgO-doped alumina sample with 0.21 vol.% glass phase and a Na₂O/SiO₂ ratio of 0.9 after 0 h at 1525°C. The measured grain boundary thickness of ~1.4 nm for this sample is in agreement with the theoretically estimated [3] grain boundary thickness. However, after 1 h or longer at 1525°C, samples with 0.21 vol.% glass and Na₂O/SiO₂ ratios of 0.9 have the same densities as samples with 0.21 vol.% glass and Na₂O/SiO₂ ratios of 0.1, and the grain boundary thicknesses of those samples after 3 h at 1525°C are ~0.5 nm (Figure 3.7b) and substantially thinner than the calculated grain boundary thickness of 1.4 nm.

The thinner grain boundary demonstrates that the addition of MgO causes a reduction of the amount of liquid phase in the grain boundaries after longer time at 1525°C. In the literature it is reported that excess liquid phase, after an equilibrium grain boundary thickness [75] is reached, can accumulate in triple pockets. However, we did not observe any triple pockets in the 380 ppm MgO-doped samples with 0.21 vol.% glass. Therefore, the impurities and dopants that formed the liquid phase after 0 h have to be distributed elsewhere in the sample after 3 h at 1525°C. Since SiO₂-containing second phases, such as mullite or cordierite, were not observed in the samples, we hypothesize that SiO₂ and MgO form a solid solution in α -alumina, as proposed by Handwerker et al. [16]. This co-dissolution mechanism would significantly reduce the total amount of SiO₂ and, therefore, the liquid phase content in the samples and in the grain boundaries.

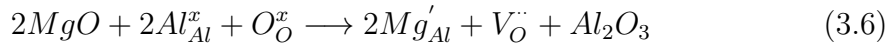
The EDS maps in Figure 3.8 show the distribution of Si around a grain boundary in MgO-doped samples with a calculated glass concentration of 0.21 vol.% after 0 h and 3 h at 1525°C. Figure 3.9 shows the corresponding EDS line scans for Si and Mg across the grain boundaries. It can be seen that after 0 h at 1525°C SiO₂ and MgO are strongly concentrated in the grain boundaries, and a chemical grain boundary thickness, δ_{chem} , of ~1.7 nm is estimated (Figures 3.8a and 3.9a), which is close to the structural grain boundary thickness of 1.4 nm measured from the high resolution TEM image (Figure 3.7a). After 3 h at 1525°C MgO and SiO₂ are still concentrated on the grain boundary, however, the chemical grain boundary thickness, δ_{chem} , is ~3.2 nm (Figure 3.8b and 3.9b) and substantially thicker than the observed structural grain boundary thickness, δ_{str} , of ~0.5 nm (Figure 3.7b). This difference in structural and chemical grain boundary thickness after 3 h supports the argument that MgO and SiO₂ form a solid solution in the

alumina lattice in the near grain boundary region. If we assume that equal amounts of MgO and SiO₂ dissolve into the alumina lattice to form the proposed defect complex, and that all MgO in the sample is consumed by this process, then 380 ppm SiO₂ must be removed from the amorphous grain boundary phase. This would leave 202 ppm SiO₂ in the grain boundaries to form the amorphous film with a calculated grain boundary thickness of 0.5 nm, which agrees with the observed grain boundary thickness of 0.5 nm.

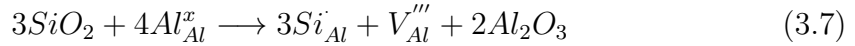
To further evaluate whether MgO and SiO₂ form a solid solution in α -alumina we conducted first-principles calculations based on density functional theory to gain insight into the thermodynamic stability of Mg²⁺ and Si⁴⁺ by themselves and together in the α -alumina structure. To ensure the accuracy of the calculations, the lattice parameters and energy of the α -alumina structure without any substitutions are compared with previous experiments and calculations in Table 3.3. It can be seen that the calculated lattice parameters match well with experimental values and lattice parameters from previous first-principles calculations [70, 77–81]. The difference between the present and past first-principles calculations can be attributed to the different input parameters used.

We calculated the energy of a unit cell of the α -alumina structure with substitutions according to the following balanced equations:

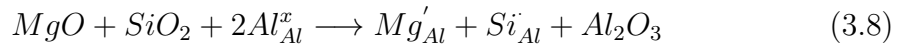
Mg-Cluster:



Si-Cluster:



Mg+Si-Cluster:



Defect simulations of aliovalent cation substitutions in alumina [70] showed that the dominant compensation mechanisms for Mg²⁺ and Si⁴⁺ by themselves in alumina are the formation of oxygen and aluminum vacancies, respectively (Eq. 3.6 and 3.7).

In Eq. 3.8 Mg^{2+} and Si^{4+} compensate for each other's charge and the formation of vacancies or interstitials is unnecessary to account for dissolution in the alumina lattice. The calculations were carried out for clustered defects since they are lower in energy than isolated defects [70]. The structures were relaxed and the formation energies as a function of temperature with bulk Al_2O_3 as the reference state are plotted in Figure 3.10. It can be seen that the formation energy for the Mg+Si-cluster, E_{Form}^{Mg+Si} , is lower than the formation energies of the Mg-cluster, E_{Form}^{Mg} , and the Si-cluster, E_{Form}^{Si} , which shows that the Mg+Si-cluster is more stable than the Mg-cluster and the Si-cluster. Since two Mg^{2+} ions and three Si^{4+} ions are necessary to form the Mg-cluster and Si-cluster, respectively, but only one Mg^{2+} and one Si^{4+} are required to form the Mg+Si-cluster, the formation energies of the clusters can be compared by

$$\Delta E_{Form} = E_{Form}^{Mg+Si} - \left(\frac{1}{3}E_{Form}^{Si} + \frac{1}{2}E_{Form}^{Mg} \right) \quad (3.9)$$

The formation energy difference, ΔE_{Form} , is plotted in Figure 3.10 and it can be seen that ΔE_{Form} is negative at all temperatures, which means that the Mg+Si-cluster is more energetically favored to form than the Mg-cluster or Si-cluster. This shows that MgO and SiO_2 have a higher co-solubility in α -alumina than MgO or SiO_2 by themselves. In α -alumina the Al^{3+} cation sites are 6-fold coordinated and Al^{3+} has an effective ionic radius of 53.5 pm, while the radii of Mg^{2+} and Si^{4+} are 72 pm and 40 pm, respectively. Therefore, Mg^{2+} and Si^{4+} can compensate for each other's size and charge difference relative to Al^{3+} in the α -alumina lattice, which explains the lower energy of the Mg+Si-cluster. The stable phases for MgO and/or SiO_2 and Al_2O_3 are spinel, cordierite, and mullite. However, we hypothesize that if both MgO and SiO_2 are present at low concentrations, then it is more favorable for MgO and SiO_2 to form a solid solution in the α -alumina structure than to form a second phase or remain in the grain boundaries as a siliceous liquid phase.

The described mechanism could also influence the distribution of other oxides in the samples, such as Fe_2O_3 , CaO , and Na_2O . Figure 3.11 shows the element distribution obtained from EDS of two grain boundaries in samples sintered at 1525°C for 0 h and 3 h, respectively. Figures 3.11a and e show the segregation of MgO to the grain boundaries after 0 h and 3 h, respectively, and it can be seen that after 0 h at 1525°C Mg is more strongly concentrated in the grain boundary

than after 3 h at 1525°C, due to the mechanism described above. From Figures 3.11b and f it can be seen that there is no segregation of Fe₂O₃, which indicates that Fe₂O₃ is in solid solution in the alumina lattice [70], since the Al₂O₃-Fe₂O₃ phase diagram shows considerable solubility [82]. Figures 3.11c, d, g, and h show that there is a slightly higher Na and Ca signal coming from the grain boundaries, showing that Na and Ca segregate to the grain boundaries and are components of the liquid grain boundary phase. Ca is more concentrated in the grain boundary after 3 h at 1525°C, due to the narrower grain boundary thickness (Figure 3.7b).

It can be seen that the Na signal after 0 h at 1525°C (Figure 3.11c) shows a slight segregation of Na to the grain boundary, but after 3 h at 1525°C (Figure 3.11g) no segregation can be observed. It should also be noted that it is challenging to detect Na using EDS since the Na signal disappears quickly after the high-voltage electron beam is focused on the grain boundary. Therefore, we believe that there is still Na on the grain boundaries, even though the EDS map does not show an increased Na signal. However, since the Na signal is lower, we believe that after 3 h at 1525°C there is less Na₂O on the grain boundaries than after 0 h at 1525°C. The reduced amount of Na might be a result of volatilization of Na₂O during sintering. Figure 3.12 shows the influence of sintering time and temperature on the Na₂O concentration, obtained by ICP analysis, during sintering for samples with target concentrations of 560 ppm Na₂O. Between 1300°C and 1525°C the Na₂O concentration is constant at ~510 ppm, which is 50 ppm below the target level. The lower Na₂O concentration might be due to volatilization at earlier stages. After heating to 1600°C there is a loss of ~250 ppm or a ~50% decrease in Na₂O concentration (Figure 3.12a). After sintering at 1525°C for 30 min the Na₂O concentration decreases by about 210 ppm or 40%, but remains constant at ~300 ppm when heated to 1525°C for up to 8 h (Figure 3.12b). This Na₂O loss between 0 and 30 min at 1525°C can explain the lower Na signal in Figure 3.11g.

As explained earlier, the described dissolution of MgO and SiO₂ into the alumina lattice reduces the amount of glass phase in the grain boundaries. Since only SiO₂ is removed from the glass phase and other components of the glass phase, such as CaO and Na₂O remain, the grain boundaries can supersaturate. This can eventually lead to the nucleation of second phases, which was observed for samples with lower SiO₂ concentrations of 82 and 182 ppm.

3.6 Summary and Conclusion

The effect of MgO on the sintering of Bayer alumina powders with different chemistry was analyzed by comparing the sintering kinetics of MgO-free and MgO-doped Bayer aluminas with different impurity levels and ratios of Na₂O and SiO₂. TEM images of grain boundaries shows that the grain boundary thickness of MgO-doped Bayer alumina is reduced during densification at 1525°C and are thinner than observed in MgO-free Bayer alumina. EDS analysis suggests that MgO and SiO₂ have an increased co-solubility in the alumina lattice when present together. This co-dissolution mechanism was supported by DFT-based first-principles calculations showing that the formation energy of MgO and SiO₂ together in the alumina lattice is lower than the formation energies of MgO or SiO₂ by themselves in the alumina lattice. The reduced amount of SiO₂ on the grain boundaries of MgO-doped alumina leads to enhanced densification compared to MgO-free alumina because SiO₂ has been shown to retard densification.

The present study supports the hypothesis of Handwerker et al. [16] and high resolution SIMS observations of Gavrilov et al. [2] that the key mechanism responsible for the beneficial effect of MgO on the sintering of alumina is the reduction of amorphous phase in the grain boundaries by increasing the solubility of SiO₂ in the alumina lattice.

Table 3.1. Physical and chemical characteristics of the as-received 380 ppm MgO-doped Bayer alumina powder used in this study.

BET (m^2/g)	7.3
D_{50} (μm)	0.4
D_{90} (μm)	1.4
	ICP (ppm)
Al_2O_3	99.92 %
SiO_2	82
Na_2O	60
Fe_2O_3	140
CaO	51
TiO_2	8
MgO	380

Table 3.2. Calculated compositions and amounts of liquid in 380 ppm MgO-doped Bayer alumina samples of different chemistries at 1450°C and 1525°C.

Na ₂ O/SiO ₂ concentration		Global Na ₂ O/SiO ₂ ratio	Na ₂ O:SiO ₂ ratio in the liquid	Vol. % of liquid in sample	
ppm by wt.	ppm by mole			1450°C	1525°C
60/82 - 560/82	99/139 - 921/139	0.7 - 6.6	0.5	0.027	0.030
185/182 - 560/182	304/309 - 921/309	1.0 - 3.0	0.5	0.060	0.066
60/582	99/987	0.1	0.1	0.19	0.21
560/582	921/987	0.9	0.5	0.19	0.21

Table 3.3. Lattice parameters and equilibrium energy (E_0) compared to previous first-principles and experimental values.

Reference	E_0 (eV/atom)	a (Å)	b (Å)	c (Å)
This work	-7.48	4.76	4.76	12.99
Calc. [77–81]	-7.48	4.78	4.78	13.00
Expt. [70]		4.76	4.76	13.00

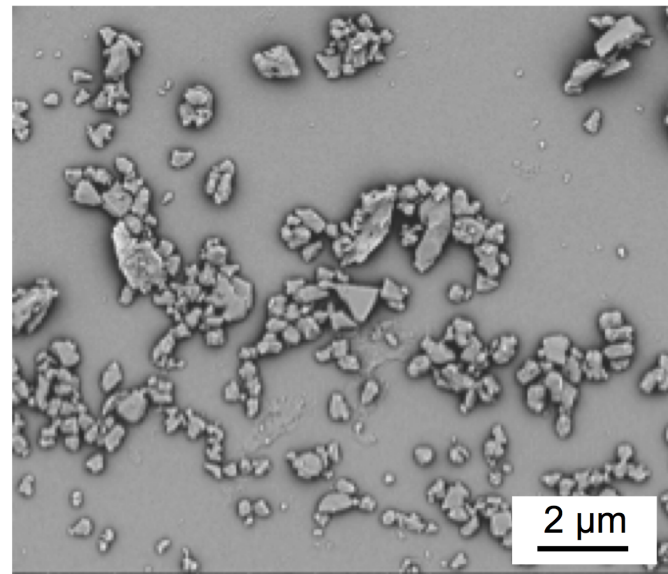


Figure 3.1. SEM image of 380 ppm MgO-doped Bayer alumina powder used in this work.

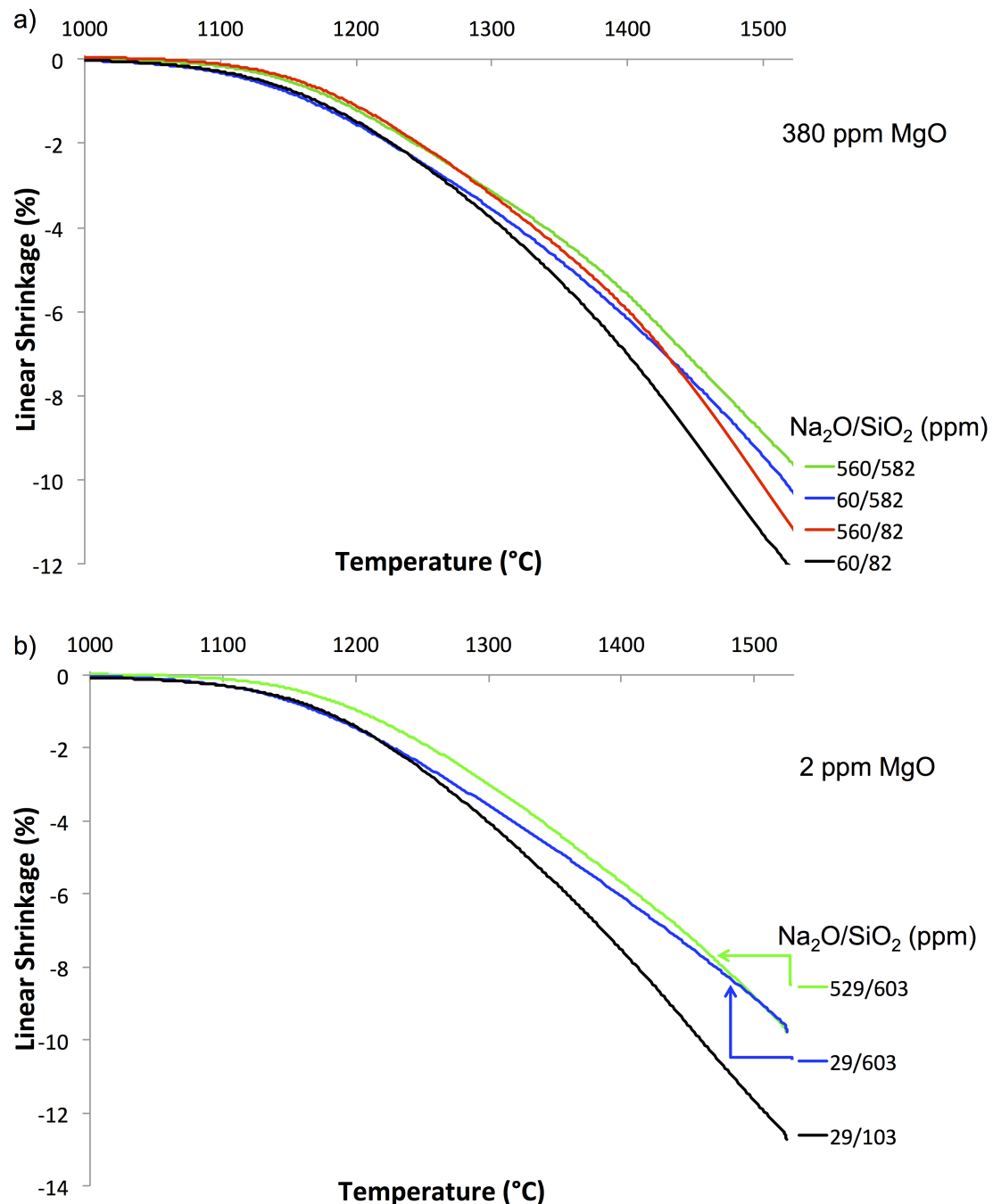


Figure 3.2. Dilatometer curves of a) 380 ppm MgO-doped and b) MgO-free [3] Bayer alumina samples with different $\text{Na}_2\text{O}/\text{SiO}_2$ levels heated at $10^\circ\text{C}/\text{min}$ to 1525°C .

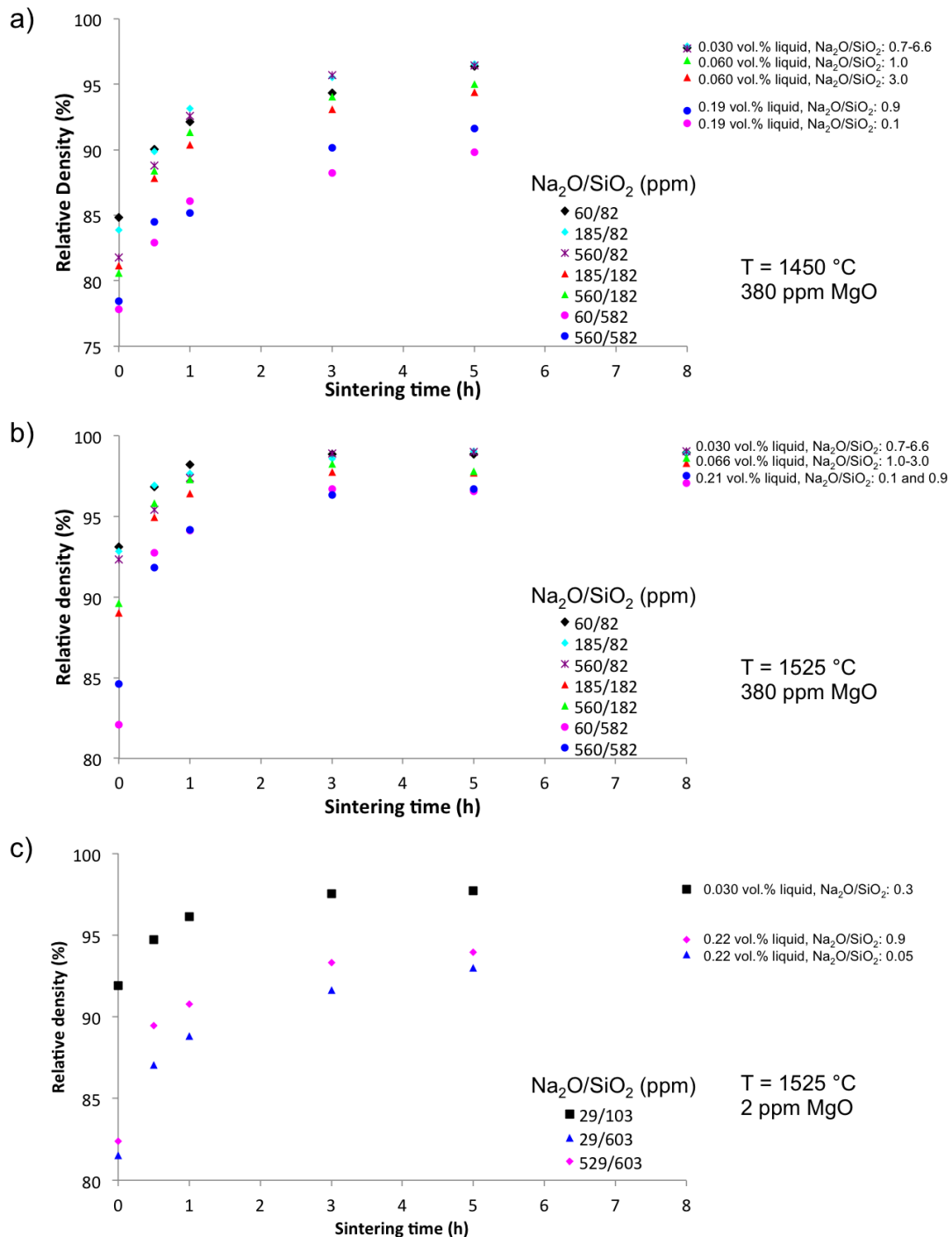


Figure 3.3. Densification kinetics of Bayer processed alumina containing different amounts Na₂O and SiO₂ and a) 380 ppm MgO sintered at 1450°C, b) 380 ppm MgO sintered at 1525°C, and c) 2 ppm MgO sintered at 1525°C [3].

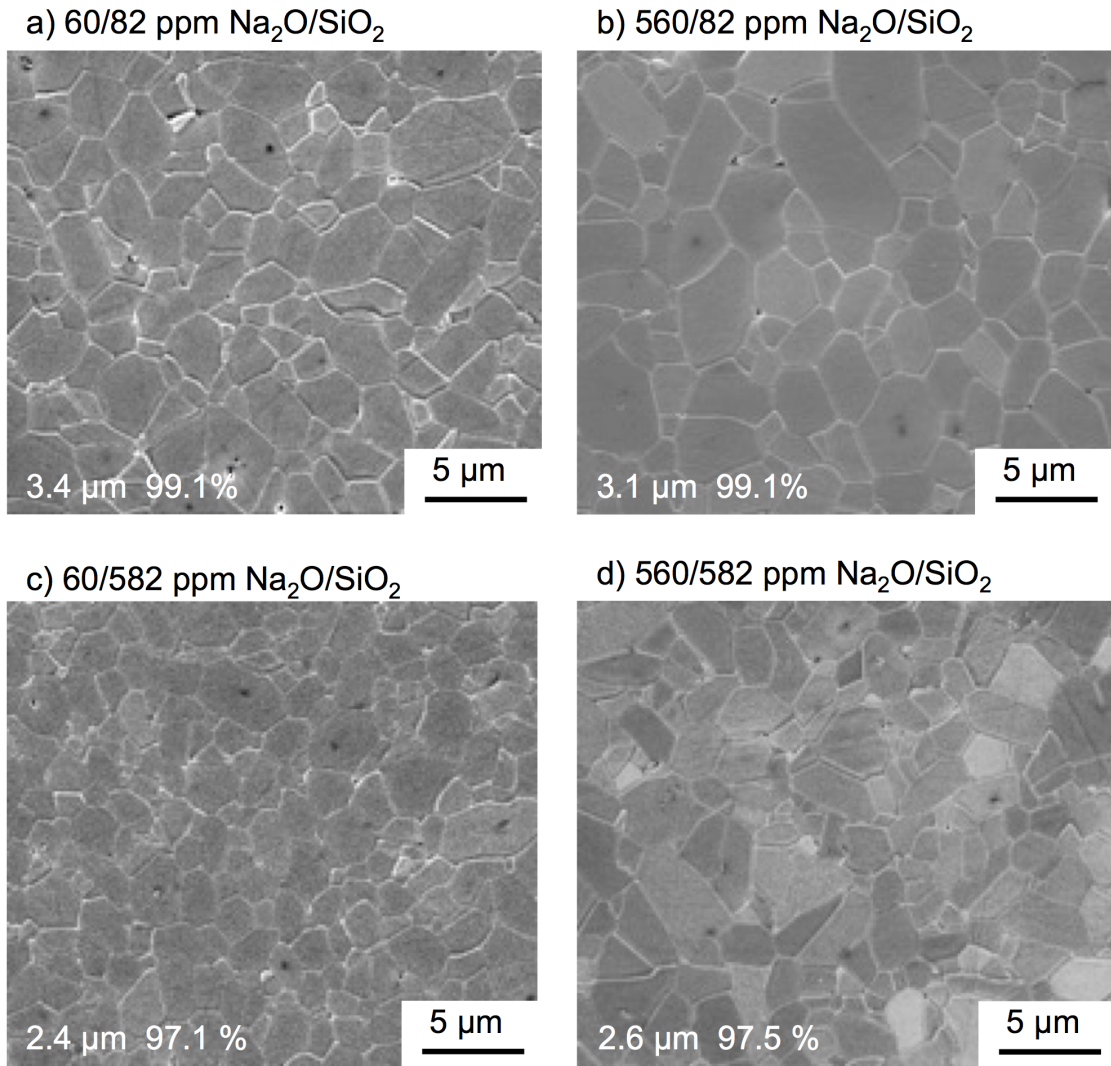


Figure 3.4. Microstructures of 380 ppm MgO-doped Bayer alumina samples with different Na_2O and SiO_2 concentrations sintered at 1525°C for 8 h.

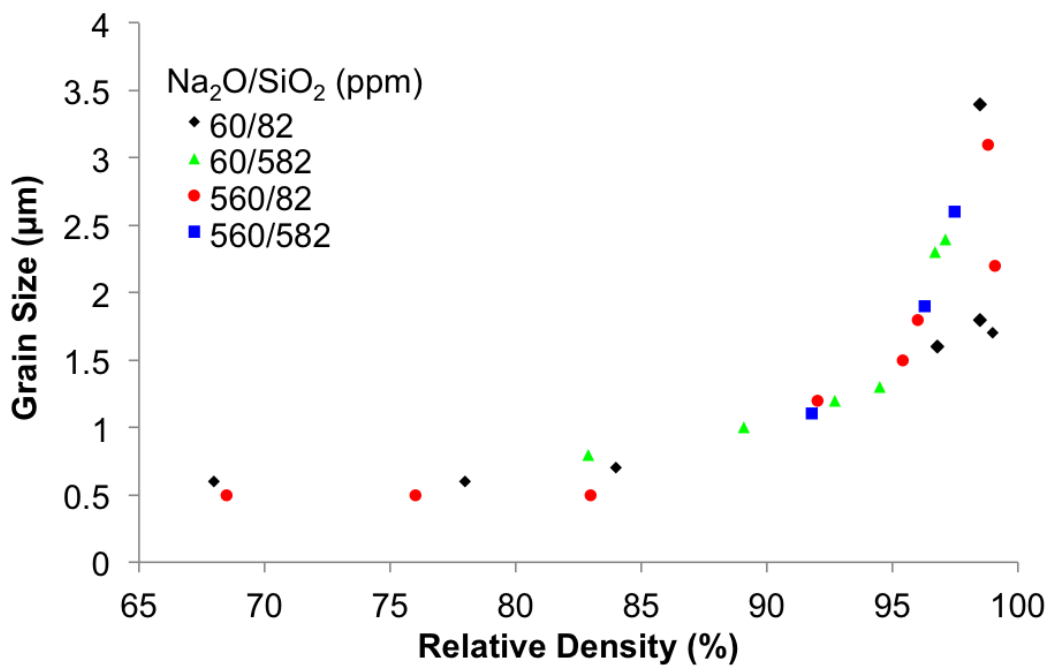


Figure 3.5. Sintering trajectories (grain size vs. relative density) for 380 ppm MgO-doped Bayer alumina samples with different Na₂O and SiO₂ concentrations.

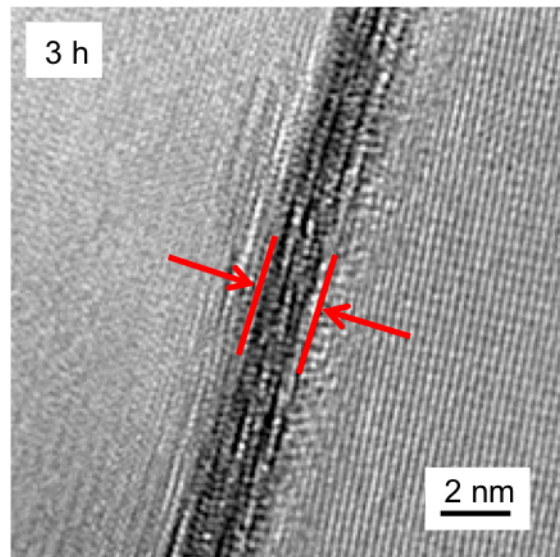


Figure 3.6. Grain boundary of a sample containing 529 ppm Na₂O, 603 ppm SiO₂, and 2 ppm MgO after 3 h at 1525°C.

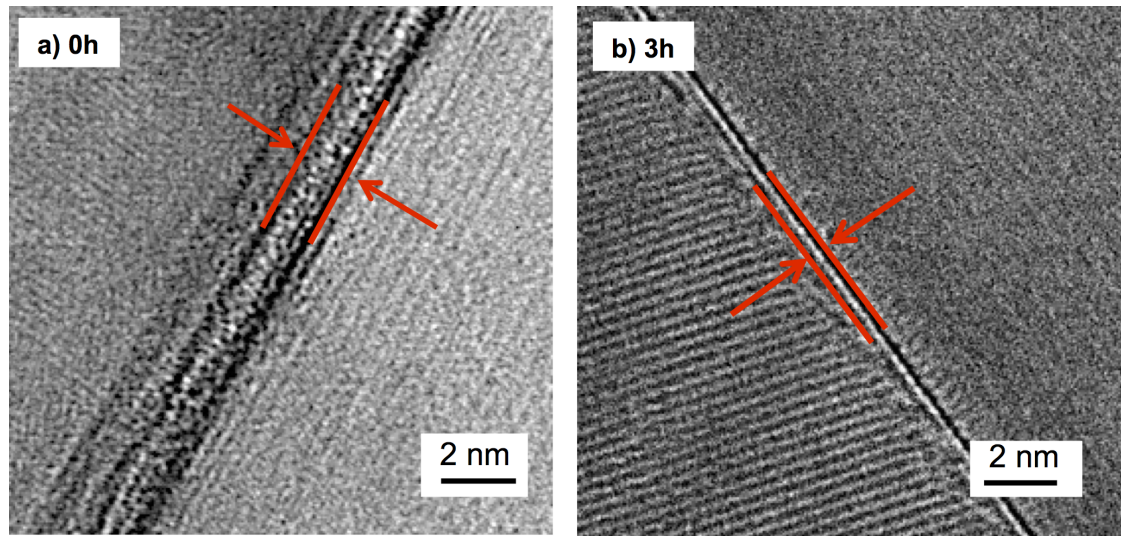


Figure 3.7. Grain boundaries of samples containing 560 ppm Na₂O, 582 ppm SiO₂, and 380 ppm MgO after a) 0 h and b) 3 h at 1525°C.

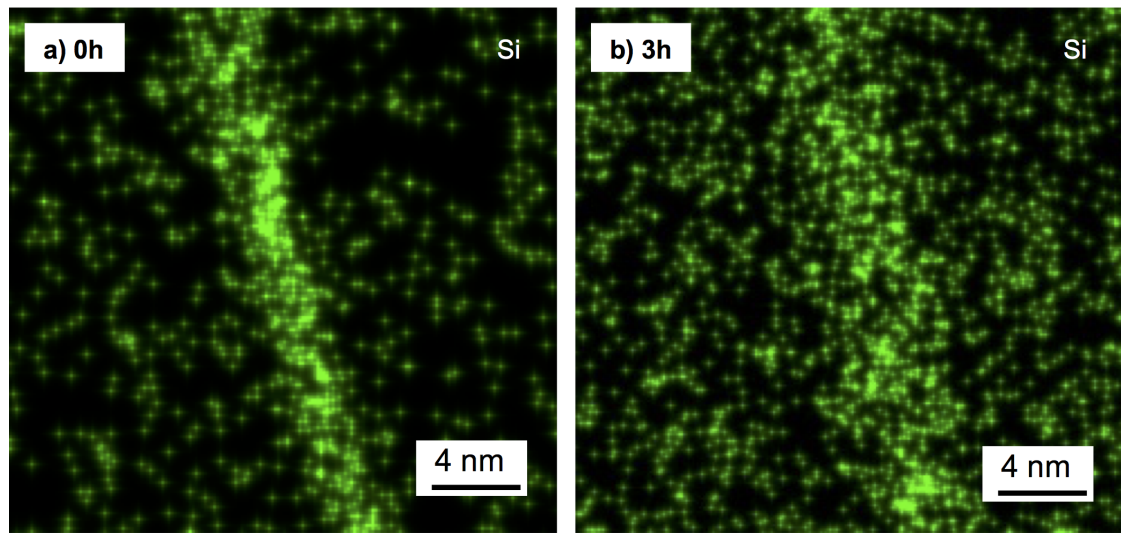


Figure 3.8. EDS of grain boundaries of samples containing 560 ppm Na₂O, 582 ppm SiO₂, and 380 ppm MgO after a) 0 h and b) 3 h at 1525°C showing the Si distribution. After 0 h Si shows a stronger segregation to the grain boundaries than after 3 h.

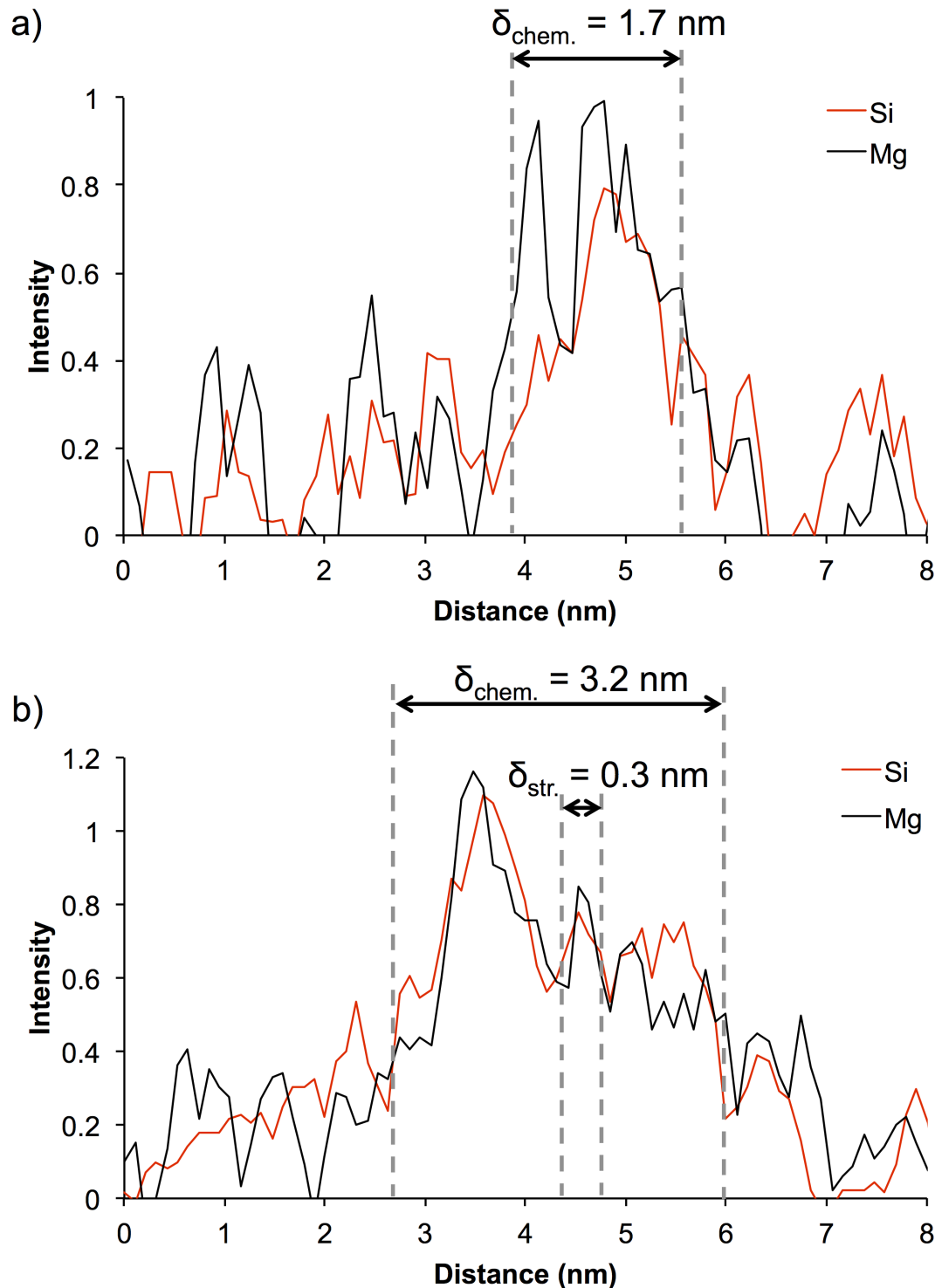


Figure 3.9. EDS line scan across a grain boundary of a sample containing 560 ppm Na₂O, 582 ppm SiO₂, and 380 ppm MgO after sintering at 1525°C for a) 0 h and b) 3 h.

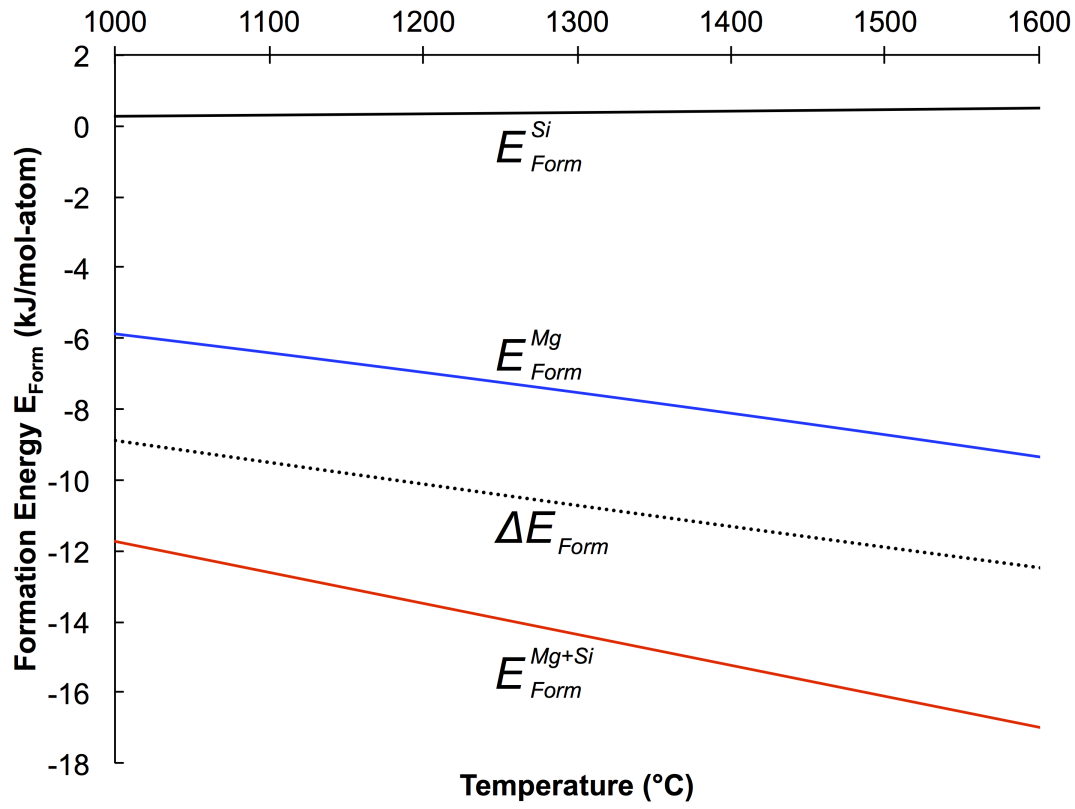


Figure 3.10. Comparison of the formation energy of $\alpha\text{-Al}_2\text{O}_3$ with an Mg-cluster (E_{Form}^{Mg}), Si-cluster (E_{Form}^{Si}) and Mg+Si-cluster (E_{Form}^{Mg+Si}) as a function of temperature. The formation energy difference (ΔE_{Form}) between the structures was calculated from Eq. 3.9 to compare the formation energy values and show that it is energetically favorable to form Mg+Si-clusters over Si-clusters and Mg-clusters.

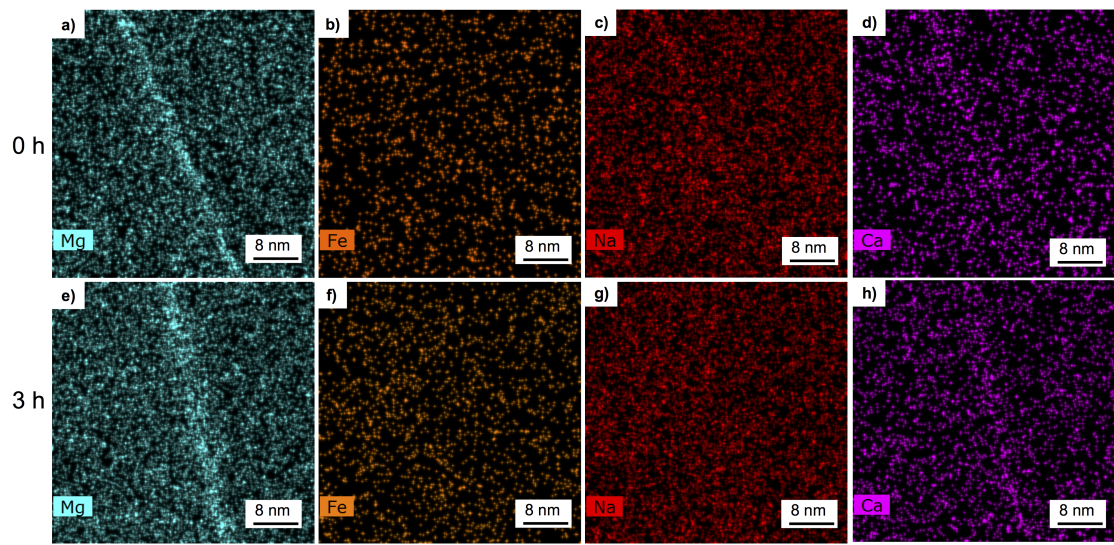


Figure 3.11. EDS maps of different oxides in 380 ppm MgO-doped Bayer alumina samples after sintering at 1525°C for a-d) 0 h and e-h) 3 h. a) and e) show the distribution of Mg, b) and f) show the distribution of Fe, c) and g) show the distribution of Na, and d) and h) show the distribution of Ca.

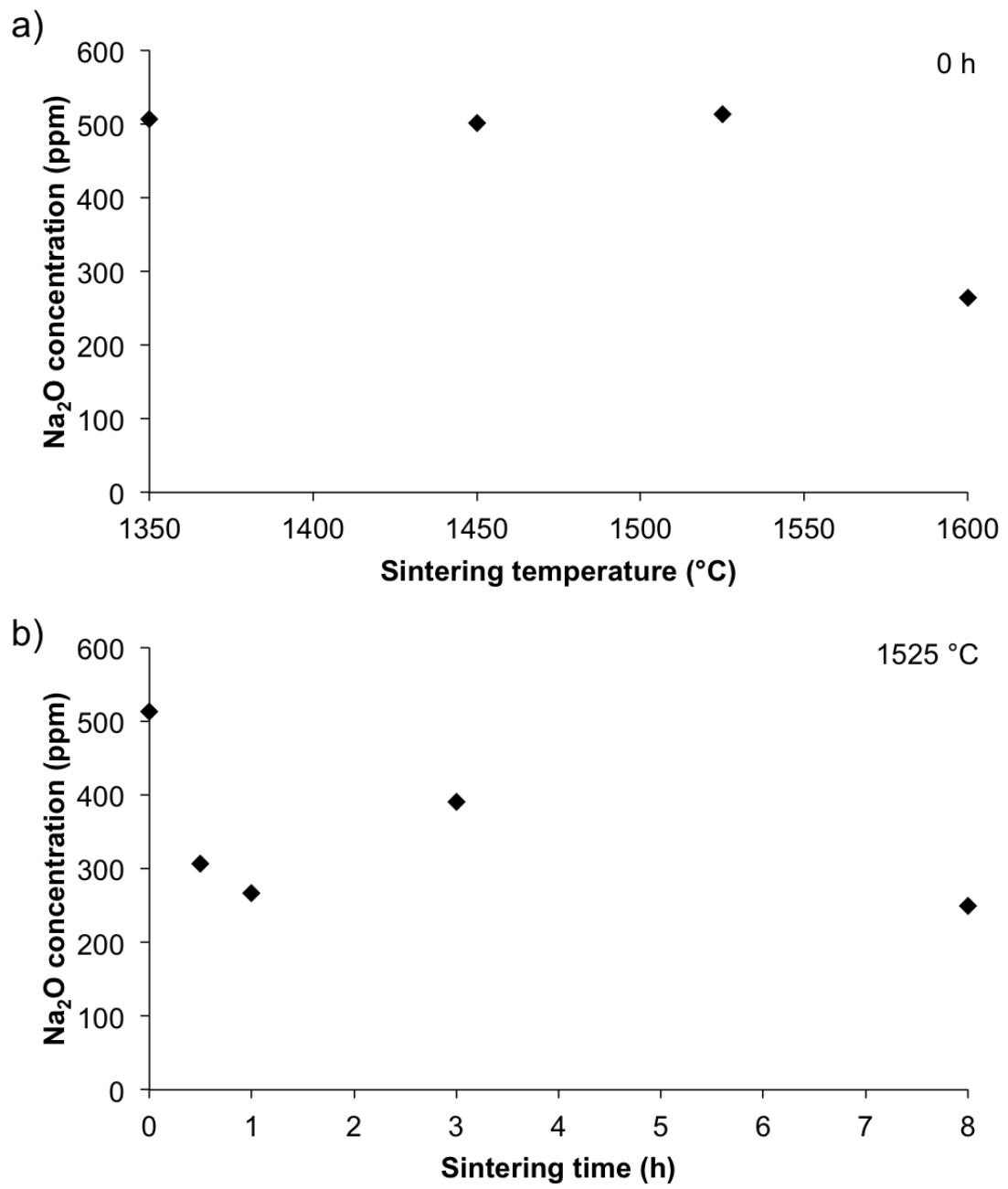


Figure 3.12. Na_2O concentration (ICP measurements) of 380 ppm MgO -doped Bayer alumina samples with 560 ppm Na_2O as a) function of sintering temperature and b) as a function of sintering time at 1525 $^{\circ}\text{C}$.

Chapter 4

Dynamic development of nanometer scale grain boundaries during liquid phase sintering

4.1 Introduction

During sintering of ceramics insoluble impurities and dopants can accumulate in the grain boundaries and form an amorphous grain boundary film that significantly influences the sintering behavior and properties of ceramics. Recently, it has been established that grain boundaries in fully dense microstructures can possess different characteristics, depending on chemistry and temperature. Based on their structure and thickness, grain boundaries have been classified into different types of thermodynamically stable complexions [25]. The type of complexion strongly affects transport kinetics and determines the mobility of a grain boundary, and if multiple complexions coexist at a time, multi-modal grain-size distributions and anisotropic microstructures can develop. One class of grain boundaries that is well investigated in dense ceramics are intergranular films (IGF), since they are often observed in a variety of systems such as Si_3N_4 , SiC , and Al_2O_3 [75, 83]. IGFs are amorphous grain boundary films with an equilibrium thickness of typically 1-2 nm. Clarke et al. showed that the equilibrium film thickness results from a balance of attractive and repulsive interparticle forces, similar to those seen in colloidal systems [83, 84].

In classical sintering theories the differences in grain boundary structures are

considered by distinguishing between solid state and liquid phase sintering with fundamental differences in their respective sintering mechanisms. Solid state sintering occurs by solid state diffusion throughout the entire sintering process. During initial stage sintering surface diffusion leads to the formation of necks between particles. Most of the densification up to $\sim 92\%$ occurs during intermediate stage, where grain boundaries between particles and pore channels along the grain edges form. At densities $>92\%$ the pore channels close and isolated pores first form and are then eliminated during final stage sintering. The dominant diffusion mechanisms during intermediate and final stage sintering are volume and grain boundary diffusion, which can be affected by solute segregated to the grain boundaries [25].

In contrast, for liquid phase sintering [85] the particle compact is penetrated by a liquid film and during the initial sintering stage the powder compact begins to densify by particle rearrangement after the liquid phase has formed. Further densification during intermediate and final stage sintering is controlled by a solution-precipitation mechanism, where the particles of the sinter are dispersed in a liquid glass matrix, and material from the grain boundary area dissolves into the liquid grain boundary phase and diffuses to the particle necks, where it precipitates, leading to a particle contact flattening and densification.

Additional models were developed in the literature that account for the liquid phase redistribution during densification. For example, a number of models describe the filling of pores during liquid phase sintering due to capillarity [86,87]. However, the existing models in the literature that address liquid phase redistribution typically deal with liquid concentrations of at least a few volume percent. In this case it can be assumed that the concentration of liquid phase is high enough to form a continuous liquid film of equilibrium thickness [75,83,84] in the grain boundaries and that excess liquid phase accumulates in necks, pores and glass pockets. For example, Svoboda et al. [88] assumed a constant equilibrium intergranular film thickness of 1.5 nm when they developed their liquid phase sintering model, and Kwon and Messing [52] estimated a grain boundary thickness of ~ 1 nm based on a squeeze film analysis.

The redistribution of liquid phase becomes more complicated as the liquid phase concentration in a sinter is reduced, for example to concentrations <0.2 vol.%. In this case the glass phase concentration could be insufficient to form a liquid

film of equilibrium thickness, and if the glass phase concentration is low enough the grain boundaries may be considered rather solid than liquid, which changes the sintering model that can be applied. This case is interesting specifically in commercial powders used in industry, since they typically contain higher impurity levels than the ultrahigh purity powders studied in academia. For example, most fundamental research on alumina uses ultrahigh purity aluminas of >99.99% Al₂O₃ and, therefore, sintering is analyzed using solid state sintering models. In contrast commercial alumina powders are typically produced by the Bayer process and are ~99.8% pure with ppm levels of Na₂O, SiO₂, CaO, and Fe₂O₃, and added MgO as a sintering additive. The concentration and ratios of these impurities and additives can vary substantially by the commercial grade and can form a small amount of liquid phase. Despite considerable interest no research has been done on determining what volume fraction of liquid phase is necessary to consider grain boundaries liquid and when to apply a liquid phase sintering model in such a system.

Concentration, chemistry, and distribution of a liquid phase change during densification as a result of increasing temperature during heating and as a result of changing grain boundary area during densification and grain growth. This implies that grain boundaries undergo a dynamic change in physical and chemical character during densification. This dynamic change in chemistry and structure and possible transitions of grain boundaries from solid to liquid or vice versa can significantly impact densification as densification typically occurs via grain boundary diffusion. While most liquid phase sintering models imply that grain boundaries may change during densification, no work has been done on identifying these changes.

In this work we develop a model to predict the dynamic development of grain boundaries from initial to final stage sintering as a function of chemical and physical parameters of a sintering powder. The predicted grain boundary thicknesses are compared with grain boundaries examined by high-resolution TEM.

4.2 Experiment

Two chemically purified Bayer process alumina powders (Almatis, Inc., Leetsdale, PA, USA) were chosen for study. Powder characteristics and experimental details are described in previous chapter. The main difference between the two powders

are the MgO concentrations of 2 ppm (MgO-free powder) and 380 ppm (MgO-doped powder), respectively. The powders were doped with up to 1000 ppm Na₂O and 1000 ppm SiO₂ using sodium acetate (NaC₂H₃O₂·3H₂O, ACS grade, BDH, VWR International LLC, West Chester, PA, USA) and tetraethyl orthosilicate (Si(OC₂H₅)₄, 98%, Aldrich Chemical Company, Inc. Milwaukee, WI, USA), respectively, to obtain chemistries similar to commercial high purity Bayer aluminas at different glass concentrations. Samples with green densities of 59.0 ± 0.5% were fabricated for sintering studies by uniaxial and cold isostatic dry pressing (CIP, Autoclave engineers, Erie, Pa, USA) at 170 MPa and 200 MPa, respectively. The dry pressed cylinders were heated at 10°C/min to 1525°C in a thermomechanical analyzer (TMA, Linseis PT1600, Robbinsville, NJ, USA) to record the shrinkage during heating. Samples were heated at 10°C/min to 1200°C and then at 5°C/min to 1525°C for different hold times. Microstructure and density were measured by the linear intercept (ASTM Standard E112-96) [37] and Archimedes methods (ASTM standard B962-15), [36] respectively. The structure and chemistry of grain boundaries were investigated by transmission electron microscopy (TEM) and energy dispersive x-ray spectroscopy (EDS) using a dual aberration corrected FEI Titan [84] field emission microscope operated at 300 kV and FEI Talos (FEI, Hillsboro, OR, USA) field emission microscope at 200 kV. The EDS on both microscopes is an FEI Super-X system consisting of four SDDs (Silicon Drift Detectors) with a solid angle of 0.9 sr. The samples for TEM and EDS were air-quenched from the sintering temperature and prepared using a focused ion beam (Quanta 200 3D Dual Beam FIB, FEI, Hillsboro, OR, USA). Grain boundaries were chosen for analysis that were oriented parallel to the TEM beam in order to accurately measure grain boundary thicknesses in the 2D projection images and EDS profiles.

4.3 Grain boundary thickness in MgO-free alumina

The development of the grain boundary thickness during densification is described for MgO-free powder samples with 529/103 ppm Na₂O/SiO₂, 529/203 ppm Na₂O/SiO₂, and 529/603 ppm Na₂O/SiO₂. As shown in the previous chapter, the main difference of the samples is the concentration of glass phase that forms. The liquidus projection of the Al₂O₃-Na₂O-SiO₂ phase diagram [88] was used to predict the equilibrium composition of the glass phase during heating as a function

of temperature [3], and based on the concentration of Na₂O and SiO₂ the glass phase concentration $\phi(T)$ was estimated as a function of temperature, as shown in Figure 4.1.

The liquid glass is expected to accumulate in particle contacts due to capillary forces [87], and during densification it is assumed that the liquid phase accumulates in the grain boundaries until an equilibrium film thickness [75] is reached. After this equilibrium thickness is reached it is assumed that the excess liquid phase accumulates in the particle necks. The fraction of a particle/grain surface that is in contact with another particle/grain, i.e. the fraction of grain boundary area, increases with increasing density [89]:

$$\alpha(\rho) = 1 - r(\rho) \left(1 - \frac{\rho}{100}\right)^{\frac{1}{2}} \quad (4.1)$$

where r is a factor between 1.4 and 1.7, depending on the relative density. With these assumptions the grain boundary thickness based on the amount of impurities in the samples can be estimated by:

$$\delta = 2 \frac{V_g \phi(T)}{S_g (1 - \phi(T)) \alpha(\rho)} \quad (4.2)$$

where V_g and S_g are the average volume and average surface area of a particle/grain. The parameters of this equation are specific to the system investigated and change during sintering.

If the calculated grain boundary thickness is smaller than a monolayer, e.g. the size of a SiO₄⁴⁻ tetrahedron (~ 0.3 nm), the liquid phase concentration in the sample is not high enough to form a liquid grain boundary phase, assuming a homogeneous distribution of the liquid phase in the sample. We assume that a grain boundary thickness > 0.6 nm, i.e. a bilayer of SiO₄⁴⁻ tetrahedra, is necessary to consider the grain boundary liquid or liquid like. For calculated grain boundary thicknesses > 0.6 nm the grain boundary thickness is assumed to be limited by an equilibrium film thickness, if the concentration of the liquid phase is high enough to form an amorphous film of equilibrium thickness. If the concentration of the liquid phase is not high enough to form an amorphous film of equilibrium thickness, the grain boundary thickness is limited by the concentration of glass phase in the sample.

Dilatometry was used to determine the development of relative density as a function of temperature (Figure 4.2), assuming isotropic shrinkage of the samples.

Now the increase in liquid phase concentration can be expressed as a function of relative density, as seen in Figure 4.3. V_g and S_g were estimated using the average particle/grain size determined from micrographs, assuming spherical particles of the same size. Using the sintering trajectories shown in Figure 4.4, V_g and S_g can be expressed as a function of relative density. The grain boundary thickness can be calculated as a function of relative density since all parameters in Eq. 4.2 can be expressed as a function of the relative density.

4.4 The equilibrium film thickness model

In 1987 Clarke proposed a model to calculate the equilibrium grain boundary thickness based on the equilibrium between attractive van der Waals and capillary pressures (P_{vdW} and P_C) and repulsive electric double layer and structural disjoining pressures (P_{ELD} and P_{ST}) [83, 84]:

$$P_{vdW} + P_C = P_{ELD} + P_{ST} \quad (4.3)$$

The van der Waals pressure is given by

$$P_{vdW} = \frac{H}{6\pi h^3} \quad (4.4)$$

where h is the grain boundary thickness and H is the Hamaker constant, which can be estimated by:

$$H = \frac{3}{4}kT \left(\frac{\varepsilon_\alpha - \varepsilon_\beta}{\varepsilon_\alpha + \varepsilon_\beta} \right)^2 + \frac{3\pi\hbar v}{8\sqrt{2}} \frac{(n_\alpha^2 - n_\beta^2)^2}{(n_\alpha^2 + n_\beta^2)^{\frac{3}{2}}} \quad (4.5)$$

where k is the Boltzmann constant, T is the absolute temperature, ε_α and ε_β are the dielectric constants of the ceramic and the glass phase, respectively, and n_α and n_β are the refractive indices of the ceramic and the glass phase, respectively.

In Clarke's original work the capillary pressure was assumed to be constant, which is a valid assumption for samples at constant densities. However, during densification the capillary pressure changes and can be estimated by [52]:

$$P_C = \frac{\left(0.59 - 0.79(1-\rho)^{\frac{1}{2}}\right)\rho^{\frac{1}{3}}}{0.39(1-\rho)^{\frac{1}{2}}\left(0.59 - 0.39(1-\rho)^{\frac{1}{2}}\right)} \frac{\gamma_{lv}}{r_s} \quad (4.6)$$

where γ_{lv} is the surface tension of the liquid, r_s is the particle radius, and ρ is the relative sintered density.

The structural disjoining force is given by [84]:

$$P_{ST} = -\alpha\tau_0^2 \left(\sinh^2\left(\frac{h}{2\xi}\right)\right)^{-1} \quad (4.7)$$

where a is a constant that can be approximated by the heat of fusion, τ_0 is a coefficient for the degree of ordering between 0 and 1, and ξ is a structural correlation length. The electric double layer force is given by [83]

$$P_{ELD} = \frac{16kT}{z^2\pi b_L h^2} \left(\tanh\frac{ze\psi_s}{4kT}\right)^2 (\kappa h)^2 e^{(-\kappa h)} \quad (4.8)$$

where z is the ion charge and e is the proton charge. The Bjerrum length b_L and the inverse of the Debye length κ are given by [83]

$$b_L = \frac{e^2}{4\pi\varepsilon_\beta\varepsilon_0 kT} \quad (4.9)$$

and [90]

$$\kappa = \sqrt{\frac{2N_A I e^2}{\varepsilon_\beta \varepsilon_0 kT}} \quad (4.10)$$

where N_A and I are the Avogadro's number and the ionic strength of the liquid, respectively.

4.5 Calculation of the theoretical Equilibrium Film Thicknesses

To calculate the equilibrium film thickness for alumina samples, the contributions P_{vdW} , P_C , P_{ELD} , and P_{ST} were calculated using parameters from the literature. The van der Waals pressure was estimated using Eq. 4.3 and 4.4 for a liquid sodium aluminosilicate glass film ($\varepsilon_\beta = 10$ [91], $n_\beta = 1.51$ [54]) located between

two flat alumina surfaces ($\varepsilon_\alpha = 11.6$, $n_\alpha = 1.752$) [84]. The capillary pressure was calculated as a function of the relative density and grain size from the sintering trajectories shown in Figure 4.2, using Eq. 4.6, assuming a surface tension of the sodium aluminosilicate glass of $\gamma_{glass} = 387 \text{ N/m}$ [92]. The structural disjoining pressure was calculated using the heat of fusion of carnegieite (35.8 J/cm^3) for the constant a , and a structural correlation length of 0.3 nm (approximate size of a SiO_4^{4-} tetrahedron). The heat of fusion of carnegieite was chosen since its chemical composition is close to the chemical composition of the grain boundary phase investigated here. It is reported in the literature that considerable ordering of intergranular films can extend up to 1.5 nm into the intergranular film before they can be assumed completely amorphous [93]. Therefore, a high ordering factor of 0.75 was assumed.

The electric double layer pressure was calculated as a function of film thickness h using Eq. 4.8-4.10, with $z = 1$ (Na^+ ion charge) and $\varepsilon_\beta = 10$. The electrostatic potential ψ_s and ionic strength I are difficult to estimate, since they are not reported in the literature for the present system. Literature reports estimating equilibrium film thicknesses based on Clarke's model assume values for ψ_s within a reasonable range of up to 1.5 V [83, 94]. In this work we estimate ψ_s and I based on the composition and structure of sodium aluminosilicate glass. It is reported in the literature [95] that all Al^{3+} ions in sodium aluminosilicate glasses are in tetrahedral coordination if $\text{Na}/\text{Al} \geq 1$, and the local charge deficit of an AlO_4^{5-} tetrahedron (compared to the SiO_4^{4-} tetrahedron) is compensated by an associated Na^+ . Excess Na^+ ions that are not required for this charge compensation act as network modifiers in the glass. For $\text{Na}/\text{Al} < 1$, there are not enough Na^+ ions to stabilize all Al^{3+} ions in tetrahedral coordination, and excess Al^{3+} ions can form triclusters or are in octahedral coordination [95].

In this model we assume for $\text{Na}/\text{Al} > 1$ in the glass that Na^+ ions compensating the charge of an AlO_4^{5-} tetrahedron are not mobile due to electrostatic attraction between the charged AlO_4^{5-} tetrahedron and the Na^+ ion, whereas excess Na^+ ions are assumed to be available as charge carriers. For the samples investigated here an I of 2.25 mol/l was calculated. If we assume that a fraction f_{cc} of the charge carriers segregate to the immediate particle/grain surface, a charge carrier density σ can be calculated by

$$\sigma = \frac{(c_{Na} - c_{Al}) f_{cc} V_{glass} N_A}{V_m \pi d^2} \quad (4.11)$$

where c_{Na} and c_{Al} are the concentration of Na^+ and Al^{3+} ions in the glass, respectively, V_{glass} is the volume of glass around one particle/grain, V_m is the molar volume of the glass, and d is the particle/grain diameter. The electrostatic potential can then be calculated by [83]:

$$\psi_s = \sinh^{-1} \left(\frac{\sigma 2\pi z e b_L}{\kappa} \right) \frac{2kT}{ze} \quad (4.12)$$

The composition of the glass phase in the samples estimated from the phase diagram changes during heating, and consequently the Na/Al ratio changes as shown in Figure 4.5. ψ_s changes during heating because of the changing charge carrier concentration, the increasing grain boundary area, and the increasing grain size during densification. Figure 4.6 shows the change in ψ_s during heating, assuming a glass density of 2.45 g/cm³ and 75% of the charge carriers segregate to the particle/grain surface ($f_{cc} = 0.75$). The estimated values for ψ_s are reasonable when compared to ψ_s values used in the literature [83].

Figure 4.7 shows the individual contributions to the equilibrium film thickness plotted as a function of film thickness for a sample with 529 ppm Na_2O and 603 ppm SiO_2 at 1525°C and a relative density of 93%. It can be seen that the net pressure, i.e. the sum of the acting pressures, is 0 MPa for a film thickness of 1.7 nm, which corresponds to the equilibrium film thickness.

From the above discussion it is apparent that P_{vdW} , P_{CP} , and P_{ELD} change during densification. The film thickness at which the net pressure is 0 MPa (i.e., the equilibrium film thickness) was calculated for samples at different relative densities during the sintering process, and the calculated equilibrium film thicknesses are shown in Figure 4.8. It should be noted that P_{vdW} and P_C are a function of temperature, since the parameters they are calculated from are functions of temperature, glass composition, refractive indices, dielectric constants, and surface tension. However, investigations showed that the changes in P_{vdW} and P_C due to the changing temperature are insignificant, and therefore, these contributions were assumed to be constant. Figure 4.8 shows that the equilibrium film thickness does not depend on the amount of glass phase, but decreases as a function of relative density from 2.2 nm at ~60% relative density to 1.6 nm at 98% relative density, as

seen in Figure 4.7.

It is interesting to note that for film thicknesses > 1 nm P_C and P_{ST} control the equilibrium thickness, and the contributions from P_{vdW} and P_{ELD} are negligible. At film thicknesses > 1 nm P_{ST} is not expected to change as a function of density, and, therefore, the equilibrium thickness during densification is governed by the change in P_C . For film thicknesses < 1 nm P_{ELD} , P_{ST} , and P_{vdW} significantly contribute to the force balance and P_C is negligible.

Figure 4.9 shows plots of the development of the grain boundary thickness as a function of relative density for different glass concentrations. The trajectory of the equilibrium film thickness (see also Figure 4.8) represents the grain boundary thickness if enough glass phase is present to form a film with equilibrium thickness. The three trajectories labeled with 529/103 ppm Na₂O/SiO₂, 529/203 ppm Na₂O/SiO₂, and 529/603 ppm Na₂O/SiO₂ are the estimated grain boundary thicknesses based on the amount of glass phase that is present in the samples. For all glass concentrations, the grain boundary thickness first decreases during initial and intermediate stage sintering. This decrease in grain boundary thickness is due to the increase in grain boundary area with increasing relative density, since the liquid glass phase is distributed over a larger grain boundary area. At the end of the intermediate sintering stage and during final stage sintering grain growth begins, which results in a reduction of the grain boundary area and, therefore, an increase in grain boundary thickness.

For samples with 529/103 ppm Na₂O/SiO₂ and 529/203 ppm Na₂O/SiO₂ the grain boundary thicknesses determined from the amount of glass phase are less than the equilibrium film thickness, and therefore, the grain boundary thickness is limited by the amount of glass phase in the sample. For samples with 529/603 ppm Na₂O/SiO₂ the glass phase concentration in the sample is close to the glass phase concentration necessary to form a film of equilibrium thickness, and the grain boundary thickness is limited by the amount of glass phase or the equilibrium film thickness, depending on the relative density. For samples with higher glass concentrations, the grain boundary thickness is determined by the equilibrium film thickness.

4.6 High-resolution TEM

The predicted grain boundary thicknesses were compared to grain boundary thicknesses measured from high-resolution TEM images of samples with different glass concentrations. Figure 4.10 shows high resolution TEM images of the grain boundaries of samples with 0.066 vol.% (529/203 ppm Na₂O/SiO₂), 0.21 vol.% (529/603 ppm Na₂O/SiO₂), and 0.36 vol.% glass phase (1000/1000 ppm Na₂O/SiO₂) after 3 h at 1525°C. The thicknesses of the amorphous grain boundary as measured from the TEM images are 1.0 nm, 1.7 nm and 1.9 nm, respectively.

As seen in Figure 4.9 the measured grain boundary thicknesses agree well with the predicted grain boundary thicknesses. For a sample of 96% relative density and 0.073 vol.% glass phase the predicted grain boundary thickness is 0.9 nm, and the measured grain boundary thickness is 1.0 nm (Figure 4.10a). The equilibrium grain boundary thickness for this sample is 1.6 nm. However, the glass phase concentration is only high enough to form a 1.0 nm thick film. For the sample with 0.21 vol.% (529/603 ppm Na₂O/SiO₂) and a relative density of 93% the measured grain boundary thickness of 1.7 nm agrees well with the estimated equilibrium film thickness of 1.7 nm. The glass phase concentration in this sample is high enough to form a film with a thickness of ~2.2 nm, however, the grain boundary thickness is limited by the equilibrium film thickness. For samples with even higher glass concentrations of 0.36 vol.% the glass phase concentration is high enough to form a grain boundary thickness > 3.5 nm, however, the grain boundary thickness determined by TEM is 1.9 nm, which is close to the value of the equilibrium film thickness of 1.7 nm.

Figure 4.9d shows a sample with 0.03 vol.% glass phase (29/103 ppm Na₂O/SiO₂). There is no amorphous film in the grain boundaries because for samples with low SiO₂ concentrations such as 103 ppm the theoretically predicted grain boundary is less than a monolayer, and the amount of SiO₂ is insufficient to form a continuous amorphous film in the grain boundaries. However, EDS analysis shows that there is still SiO₂ segregated to the grain boundaries. Note that the maximum sintering temperature of the samples in this work is 1525°C. At higher sintering temperatures a higher glass phase concentration is expected, and, therefore, thicker grain boundaries would be observed.

4.7 The effect of changes in powder chemistry

4.7.1 Na₂O/SiO₂ ratio

For the results above a Na₂O/SiO₂ ratio ≥ 0.5 in the sample was assumed, which results in a Na₂O/SiO₂ ratio of 0.5 in the glass phase. For Na₂O/SiO₂ ratios < 0.5 the composition of the glass phase is expected to change, and consequently the grain boundary thickness is expected to change as a function of chemistry.

Figure 4.11 shows a high resolution TEM image of a grain boundary of a sample containing 0.17 vol.% glass phase (29/603 ppm Na₂O/SiO₂) and a molar Na₂O/SiO₂ ratio of 0.1 after 3 h at 1525°C, and the measured grain boundary is ~ 1.0 nm thick. Based on the amount of impurities a grain boundary thickness of 2.2 nm is expected in those samples, which indicates that for this chemical composition an equilibrium grain boundary thickness [75] is reached at ~ 1.0 nm. Investigations on how the capillary pressure and van der Waals pressure change as a result of the changed glass chemistry show that the differences in the resulting pressures are negligible. Therefore, the reduction can be attributed to a reduction in the repulsive P_{ST} and P_{ELD} .

The Na/Al ratio in the glass phase of the sample with 29/603 ppm Na₂O/SiO₂ is < 1 , and all Na⁺ ions are assumed to stabilize Al³⁺ ions in tetrahedral coordination. Therefore, no Na⁺ ions are available as charge carriers, and P_{ELD} is assumed to be zero. If P_{ELD} is assumed to be zero and P_{ST} is the same as for higher Na₂O/SiO₂ ratios, the change in equilibrium film thickness is < 0.1 nm. This confirms the earlier conclusion that P_{ST} is the dominant repulsive pressure at film thicknesses ≥ 1 nm, and that P_{ELD} is insignificant for the equilibrium grain boundary thicknesses investigated here. This means P_{ST} has to decrease as the Na₂O/SiO₂ ratio in the sample decreases. Computer simulations showed that the ordering of sodium silicate glass between two alumina surfaces increases with increasing Na₂O/SiO₂ ratio [96]. Therefore, it is reasonable to assume a lower ordering parameter τ_0 for the sample with a molar Na₂O/SiO₂ ratio of 0.1. For example, if an ordering parameter of 0.25 is assumed the calculated equilibrium film thickness is ~ 1.0 nm for samples with a relative density of 93%, which is close to the observed grain boundary thickness seen in Figure 4.11.

4.7.2 MgO-doped Bayer alumina

The influence of MgO on the sintering of Bayer alumina was reported in chapter 3, and it was shown that MgO increases the solubility of SiO₂ in the alumina lattice. Therefore, the reduction of SiO₂ on the grain boundaries by this process has to be taken into account when the grain boundary thickness is calculated. Figure 4.12 shows high resolution TEM images of grain boundaries of the MgO-doped powder with a) 60/82 ppm Na₂O/SiO₂, b) 60/582 ppm Na₂O/SiO₂, and c) 560/582 ppm Na₂O/SiO₂ after 3 h at 1525°C and the amorphous film thicknesses are 0 nm, 0.5 nm, and 0.8 nm, respectively. For the sample containing 60 ppm Na₂O and 82 ppm SiO₂ no amorphous film is expected because the amount of liquid phase in this sample is not sufficient to form a monolayer, similar to the MgO-free powder samples with 103 ppm SiO₂ seen in Figure 4.9d.

For the samples with 60/582 ppm Na₂O/SiO₂ and 560/582 ppm Na₂O/SiO₂ the grain boundaries are substantially thinner than the theoretical calculation of ~2.2 nm. As reported in previous work, the reduced grain boundary thickness is due to a co-dissolution process of Mg²⁺ and Si⁴⁺ into the alumina lattice, which reduces the amount of liquid phase in the grain boundaries. A maximum of 380 ppm MgO and 380 ppm SiO₂ dissolve into the alumina lattice assuming that equivalent amounts of SiO₂ and MgO go into solid solution, which leaves 202 ppm SiO₂ in the grain boundaries that can form a liquid phase. With 202 ppm SiO₂ in the grain boundaries an amorphous film with a thickness of ~0.8 nm is calculated, which agrees well with the observed grain boundary thicknesses of 0.5 and 0.8 nm for the samples containing 560/582 ppm Na₂O/SiO₂ and 60/582 ppm Na₂O/SiO₂, respectively.

4.8 Conclusion

A model that describes the dynamic change in grain boundary chemistry and thickness during densification of Bayer alumina was developed. SiO₂ and Na₂O impurities form a glass phase during heating, which accumulates in particle contacts due to capillarity. The chemistry and concentration of this glass phase changes as a function of temperature. During sintering the grain boundary area changes as a result of densification and grain growth, which affects the glass phase distribution

and, therefore, leads to the observed dynamic change in grain boundary thickness as a function of relative density.

An intergranular film of equilibrium thickness can form between particles/grains if the glass phase concentration is sufficient, and an interparticle force balance governs the grain boundary thickness. We demonstrated that for grain boundary thicknesses ≥ 1.0 nm the contributions that control the equilibrium intergranular film thickness are the attractive capillary pressure and the repulsive structural disjoining pressure. If the glass phase concentration in the sample is insufficient to form an intergranular film of equilibrium thickness the grain boundary thickness is determined by the glass phase concentration in the sample. Changes in powder chemistry such as changing the $\text{Na}_2\text{O}/\text{SiO}_2$ ratio or the MgO concentration affect the concentration of glass phase in the sample and the interparticle force balance, which leads to a change in grain boundary thickness. Grain boundary thicknesses measured from high-resolution TEM images agree well with predicted values.

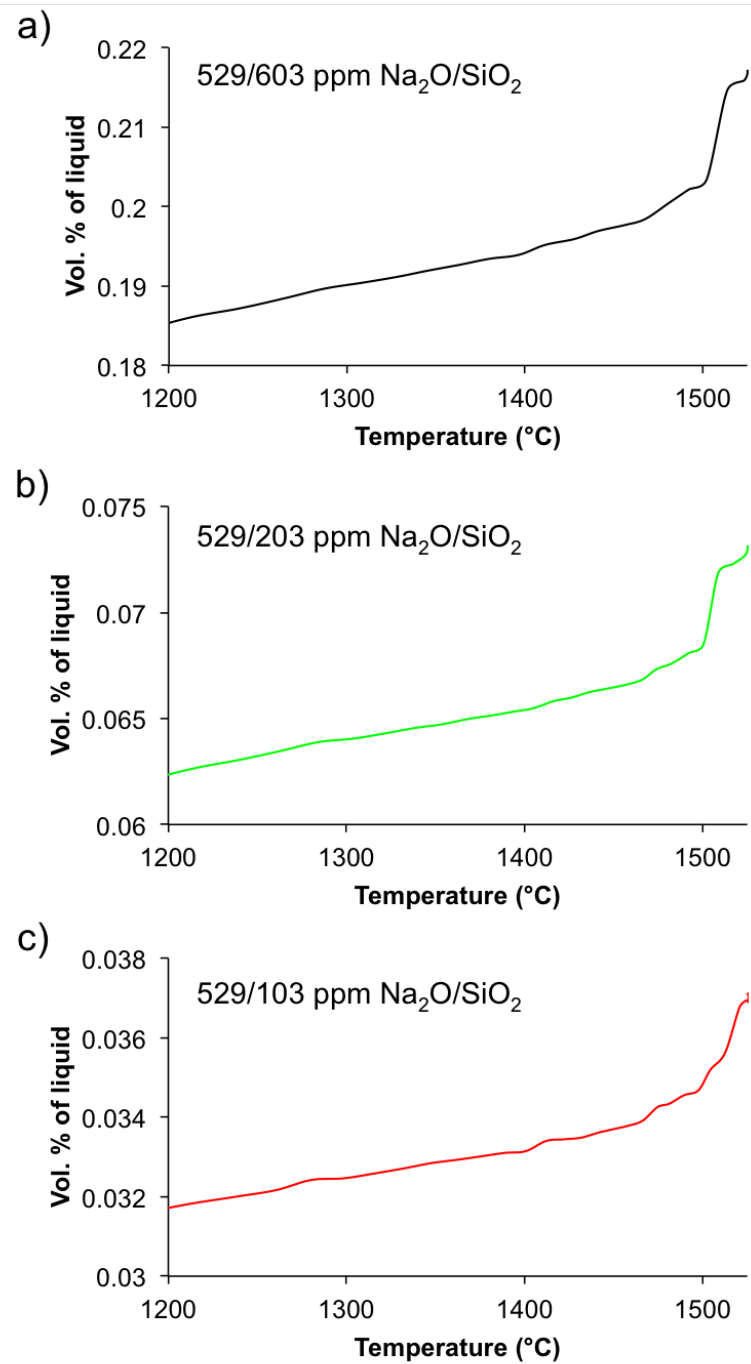


Figure 4.1. Increase in concentration of liquid phase as a function of temperature for MgO-free powder samples with 529 ppm Na₂O and different SiO₂ concentrations.

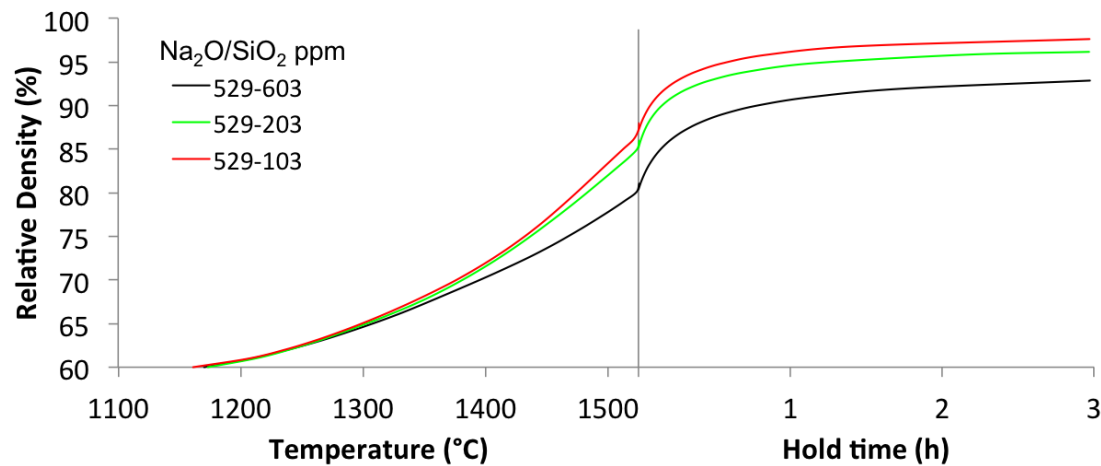


Figure 4.2. Relative density as a function of temperature and hold time determined from dilatometry for MgO-free powder samples with 529 ppm Na_2O and different SiO_2 concentrations.

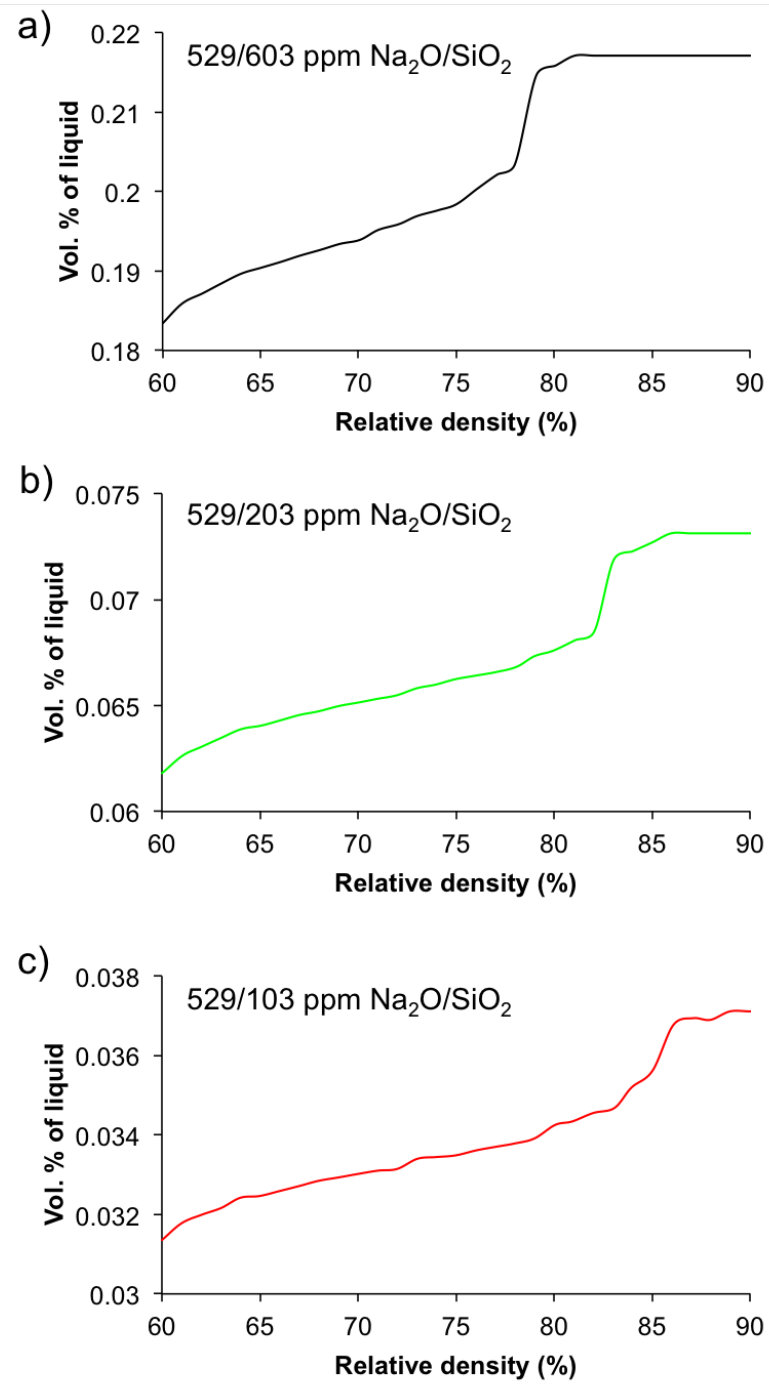


Figure 4.3. Liquid phase concentration as a function of relative density for MgO-free powder samples with 529 ppm Na₂O and different SiO₂ concentrations.

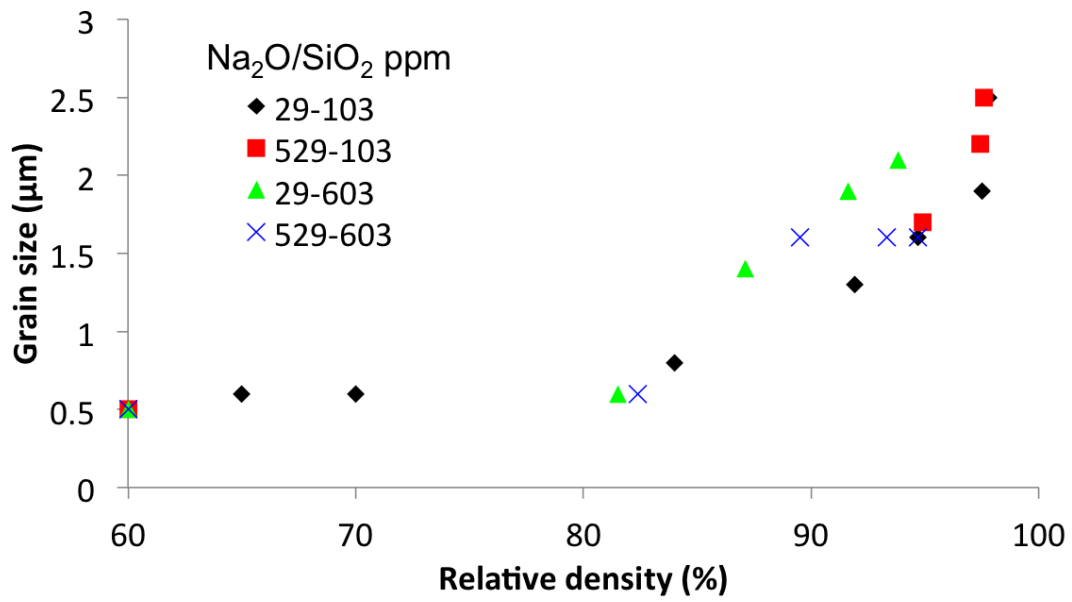


Figure 4.4. Grain size - density trajectories as a function of Na_2O and SiO_2 concentration for MgO-free alumina.

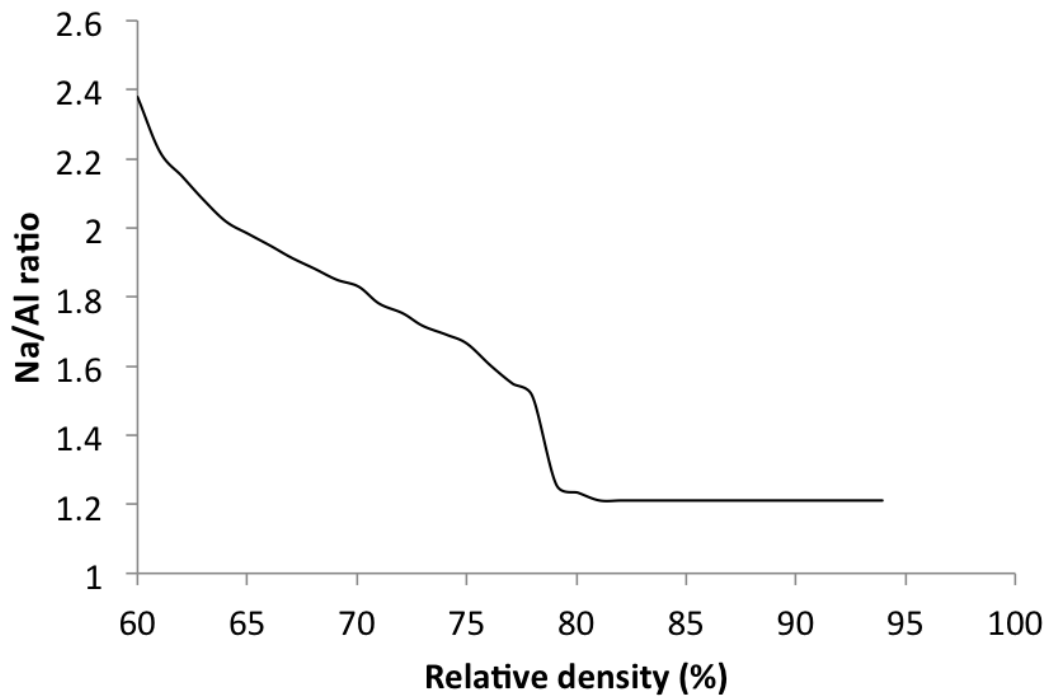


Figure 4.5. Change in Na/Al ion ratio in the liquid phase during sintering of samples with $\text{Na}_2\text{O}/\text{SiO}_2$ ratios > 0.5 .

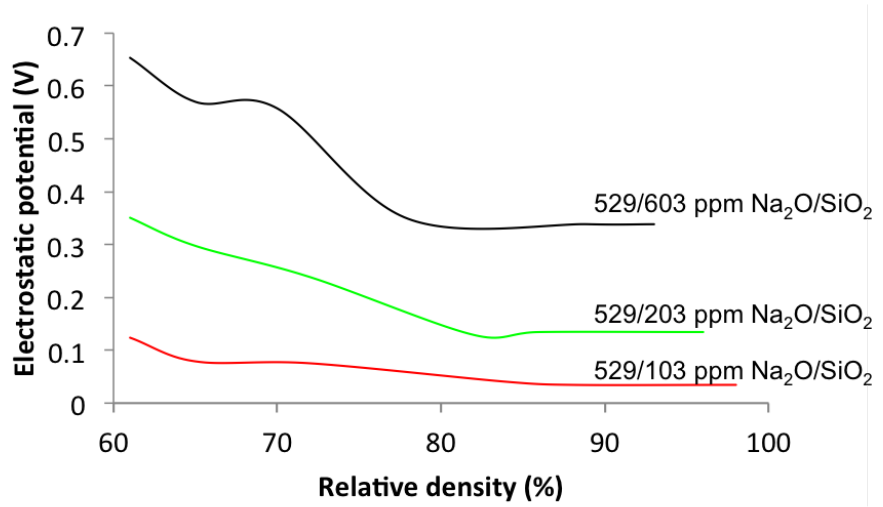


Figure 4.6. Development of the electrostatic potential as a function of relative density. For MgO-free powder samples with 529 ppm Na_2O and different SiO_2 concentrations.

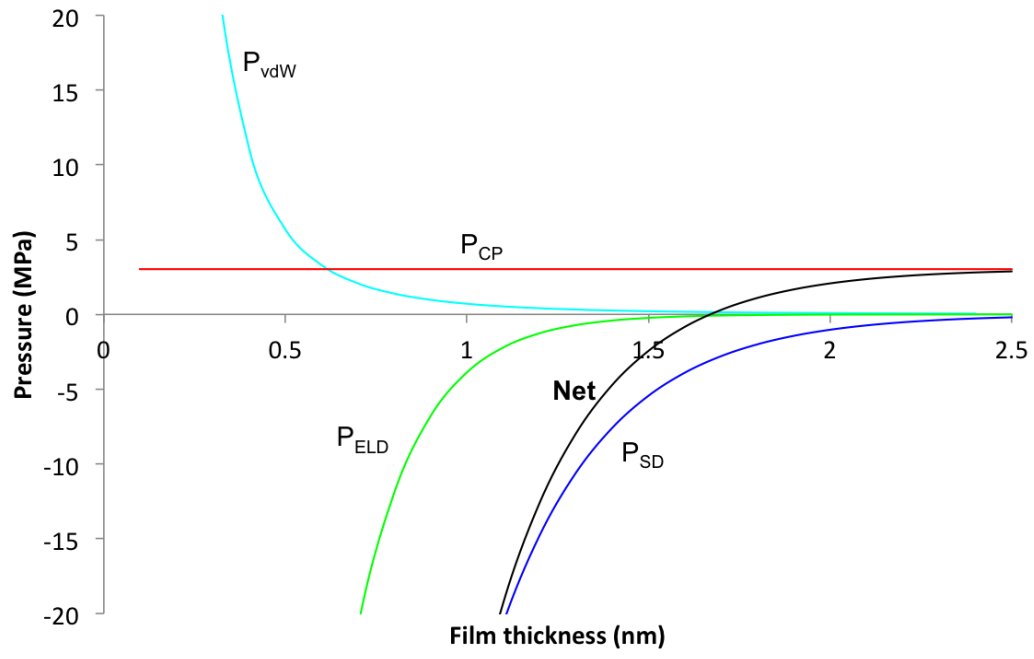


Figure 4.7. Contributions to the equilibrium film thickness as a function of film thickness for MgO-free powder samples with 529/603 ppm Na₂O/SiO₂ at a relative density of 93%.

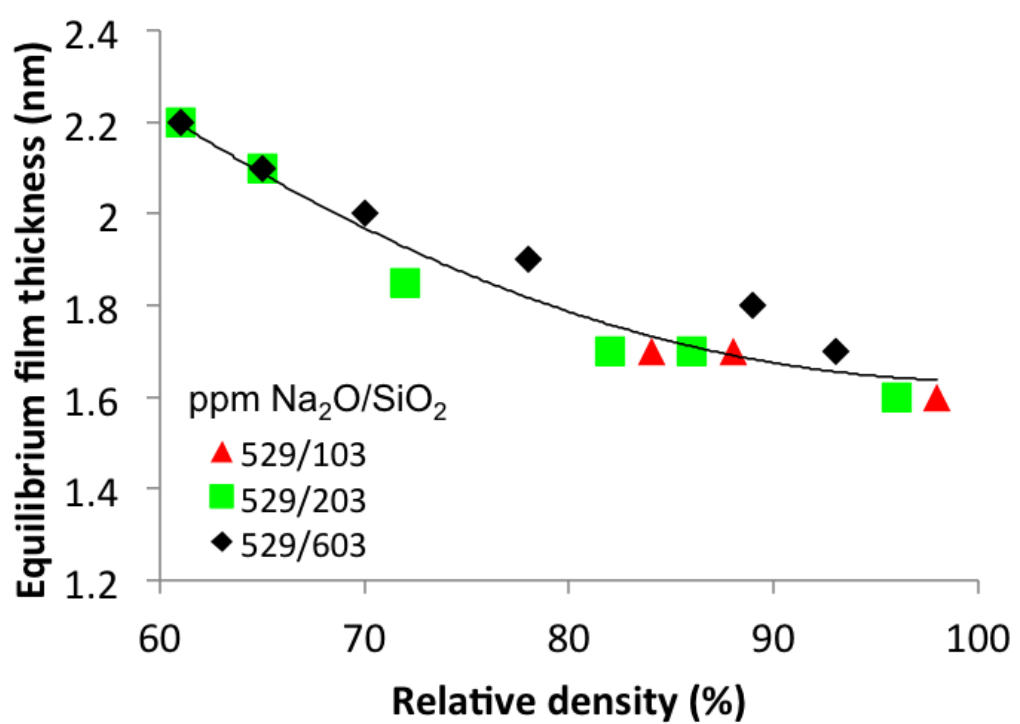


Figure 4.8. Calculated equilibrium film thickness for MgO-free powder samples at different chemistries as a function of relative density.

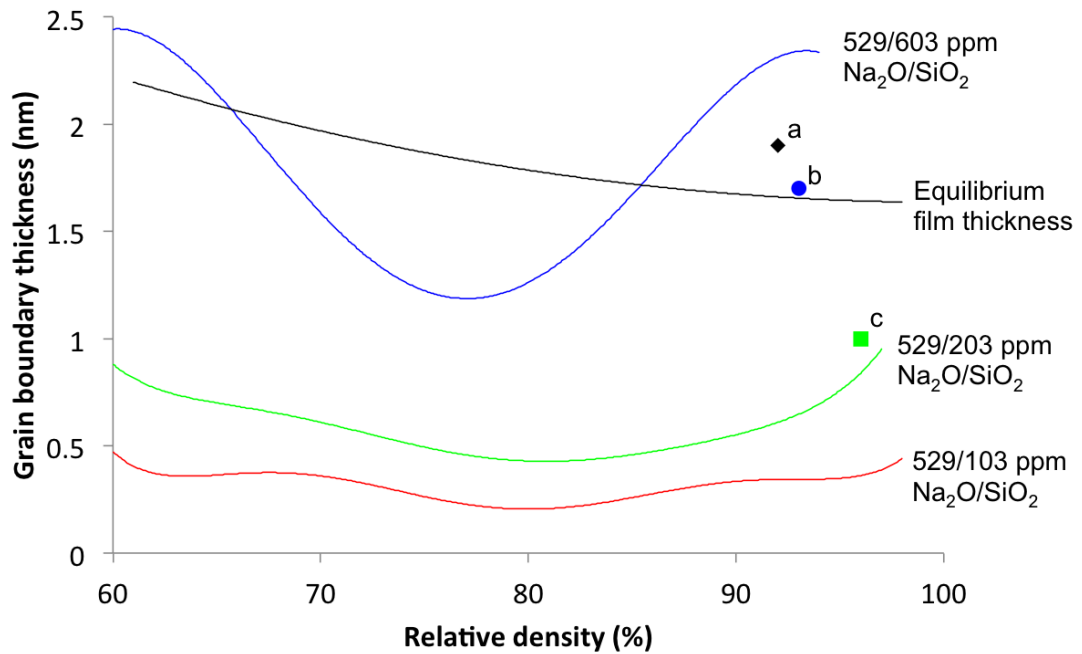


Figure 4.9. Calculated grain boundary thicknesses as a function of relative density for MgO-free powder samples. The trajectories labeled with 529/603 ppm $\text{Na}_2\text{O}/\text{SiO}_2$, 529/203 ppm $\text{Na}_2\text{O}/\text{SiO}_2$, and 529 ppm $\text{Na}_2\text{O}/\text{SiO}_2$ were calculated based on the liquid phase concentration and sintering stage. The equilibrium film thickness was calculated based on Clarke's model. The calculated grain boundary thicknesses are compared to measured grain boundary thicknesses (data points a: 1000/1000 ppm $\text{Na}_2\text{O}/\text{SiO}_2$, b) 529/603 ppm $\text{Na}_2\text{O}/\text{SiO}_2$, c) 529/203 ppm $\text{Na}_2\text{O}/\text{SiO}_2$ after heating at 1525°C for 3 h).

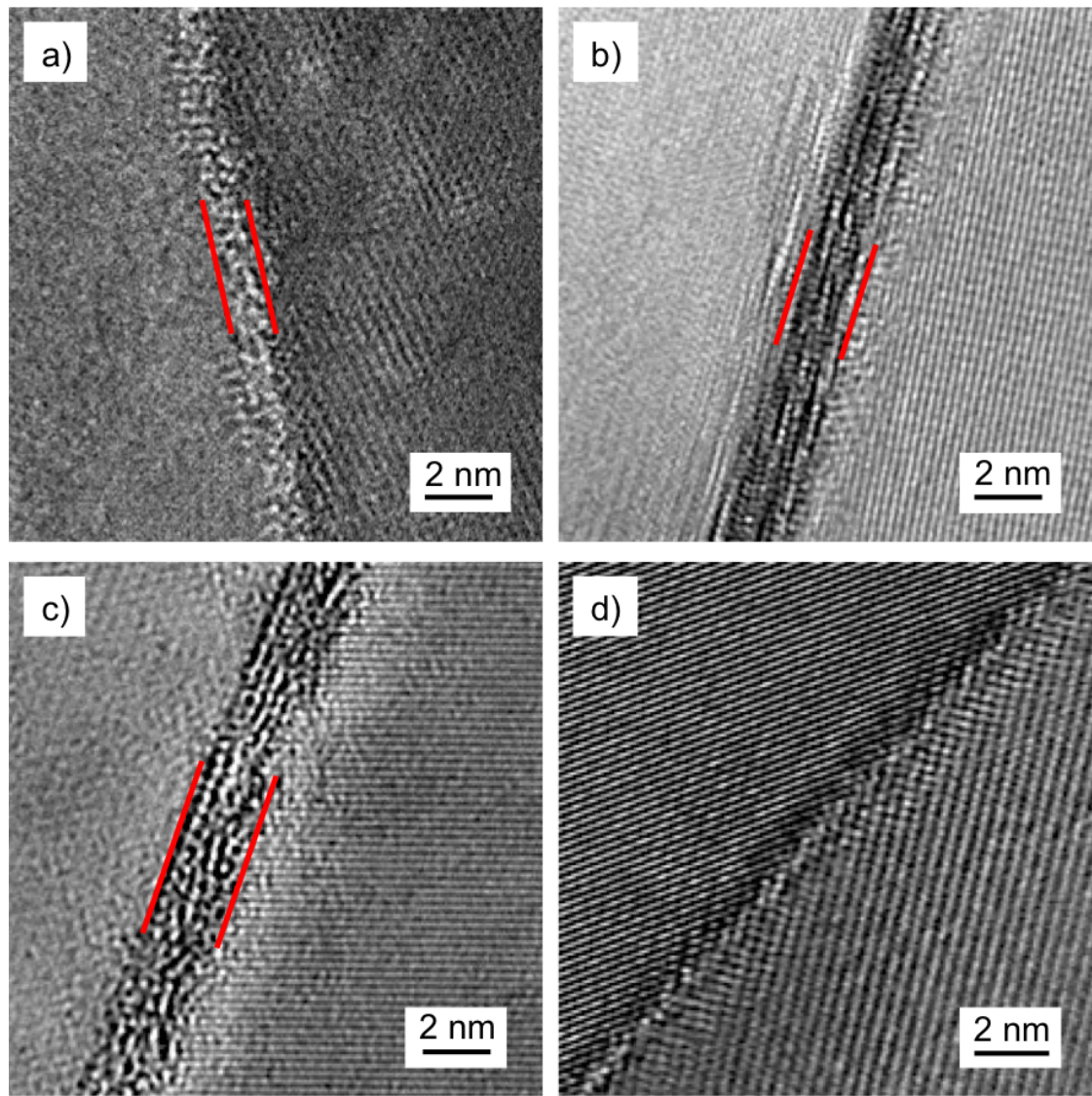


Figure 4.10. TEM images of MgO-free powder samples with a) 529/203 ppm Na_2/SiO_2 , b) 529/603 ppm Na_2/SiO_2 , c) 1000/1000 ppm Na_2/SiO_2 , and d) 29/103 ppm Na_2/SiO_2 after sintering at 1525°C for 3 h.

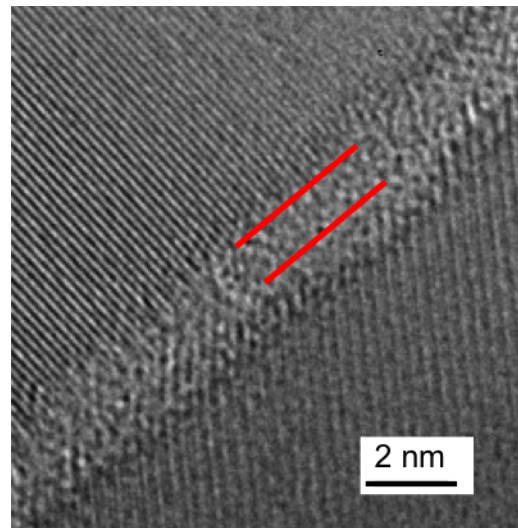


Figure 4.11. TEM image of a MgO-free powder sample with 29/603 ppm Na₂O/SiO₂.

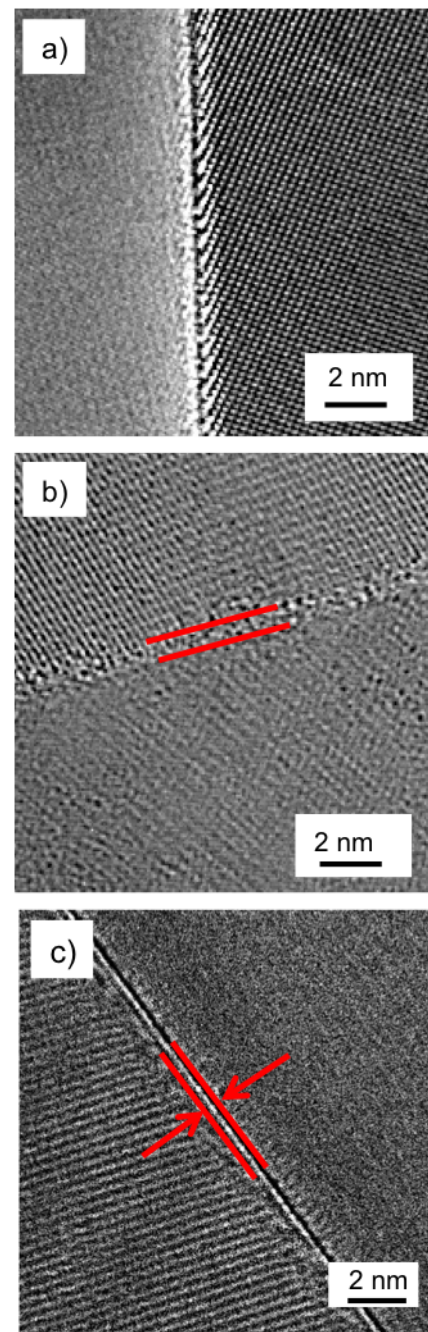


Figure 4.12. TEM images of MgO-doped (380 ppm) powder samples with a) 60/82 ppm Na₂O/SiO₂, b) 60/582 ppm Na₂O/SiO₂, and c) 560/582 ppm Na₂O/SiO₂. After heating at 1525°C for 3 h.

Chapter 5 |

Second phase formation in Bayer alumina

5.1 Introduction

Second phases such as spinel [1], calcium hexaluminate [97], and β -Al₂O₃ [44], are known to form during the sintering of Bayer alumina as a result of dopants and impurities such as MgO, CaO, and Na₂O. For Bayer aluminas, β -Al₂O₃ (Na₂O·11Al₂O₃) is of particular interest because Na₂O is present up to a few hundred ppm. Rankin and Merwin [42] were the first to observe the formation of a new alumina phase in the high Al₂O₃ region in the system CaO-Al₂O₃-MgO. They believed it was an allotropic modification of Al₂O₃, and named it β -Al₂O₃. However, later work clarified that there is a relation between the alkali content in the Al₂O₃ and the formation of β -Al₂O₃ [98], and that β -Al₂O₃ is an alkali aluminate, rather than an allotropic form of Al₂O₃ [49]. Ridgway et al. [43] reported that the Na₂O content in Bayer process alumina is sufficient to form β -Al₂O₃. Four types of beta aluminas have been reported; two of them, β -Al₂O₃ (Na₂O·11Al₂O₃) and β'' -Al₂O₃ (Na₂O·5Al₂O₃), form in the binary system Na₂O-Al₂O₃ and these phases can dissolve up to 2.5 and 5 wt.% MgO, respectively [48]. The other two beta aluminas, β''' -Al₂O₃ and β'''' -Al₂O₃ are found at higher MgO concentrations in the ternary system Na₂O-Al₂O₃-MgO [46, 48]. For completeness it should be mentioned that the existence of a β' -Al₂O₃ (Na₂O·7Al₂O₃) has been reported, but subsequent literature is in agreement that β' -Al₂O₃ is actually β -Al₂O₃ with excess Na₂O [46, 48].

The fabrication and stability of β -Al₂O₃ powder has been extensively reported for the fabrication of the solid electrolyte in Na-S batteries. Most β -Al₂O₃ powder synthesis studies use sodium carbonate and alumina [48, 49, 99], which when heated to 1100°C leads to the formation of β'' -Al₂O₃ and decomposes to β -Al₂O₃ and NaAlO₂ at >1500°C. The equilibrium vapor pressure of Na₂O over β -Al₂O₃ has been reported to be "appreciable" at >1400°C [48], and thus β -Al₂O₃ can decompose to α -Al₂O₃ by volatilization of Na₂O. Gallup [57] investigated the high temperature stability of β -Al₂O₃ under different atmospheres and reported that β -Al₂O₃ can transform to α -Al₂O₃ at 1300°C when heated in hydrogen or vacuum atmosphere. Interestingly, β -Al₂O₃ did not convert to α -Al₂O₃ after heating for 1 h at 1500°C in air, but fully converted when heated for 10 min at 1600°C.

There has been little study of β -Al₂O₃ formation in α -Al₂O₃ ceramics even though β -Al₂O₃ grains in α -Al₂O₃ ceramics can greatly impact electrical and structural properties. Duncan and Creyke [44] investigated the formation and stability of β -Al₂O₃ in α -Al₂O₃ ceramics and reported that β -Al₂O₃ forms at Na₂O concentrations as low as 0.04 wt.% if 0.25 wt.% MgO is present. An increase in β -Al₂O₃ content was observed for powders with higher Na₂O and MgO concentrations. They showed by electron-probe microanalysis that there is a higher concentration of Na₂O and MgO in the β -Al₂O₃ grains, and that β -Al₂O₃ is stable in dense α -Al₂O₃ samples (24 mm diameter x 7 mm thick) up to 1650°C in static air. In flowing air, however, β -Al₂O₃ decomposes to α -Al₂O₃ even in the center of the sample.

To date, there is no systematic study on the effect of Na₂O and SiO₂ on the formation of β -Al₂O₃ during the sintering of MgO-doped Bayer alumina powders. The goals of this work are to identify the stages and mechanisms of β -Al₂O₃ formation in α -Al₂O₃ ceramics during sintering and to determine how specific chemistries affect β -Al₂O₃ formation.

5.2 Experimental

A 380 ppm MgO-doped Bayer alumina (99.92% pure, Almatis, Inc., Leetsdale, PA, USA) was chosen to investigate the formation of β -Al₂O₃. Physical and chemical characteristics of the powder are shown in Table 5.1. The powder was doped with up to 1000 ppm Na₂O and 1000 ppm SiO₂ using sodium acetate (NaC₂H₃O₂·3H₂O, ACS grade, BDH, West Chester, PA), and TEOS (Si(OC₂H₅)₄,

98%, Aldrich Chemical Company, Inc., Milwaukee, WI), respectively. The detailed doping procedures were described in previous chapters. After drying the powders were sieved to $-106\text{ }\mu\text{m}$, dry pressed at 170 MPa, and subsequently cold isostatically pressed at 200 MPa (CIP, Autoclave Engineers, Erie, PA) to form ~ 3 mm tall cylindrical samples with 6 mm and 12.7 mm in diameter. The samples were sintered in a box furnace at $10^\circ\text{C}/\text{min}$ to 1200°C and then at $5^\circ\text{C}/\text{min}$ to the final temperature between 1450°C and 1600°C , followed by a hold time of up to 8 h. The sintered samples were ground to half their initial height and polished to a surface finish of $1\text{ }\mu\text{m}$. The crystal structure of the second phase was identified by x-ray diffraction (XRD, X’Pert Pro MPD, PANalytical B.V., The Netherlands) using Cu K_α radiation. The concentration of $\beta\text{-Al}_2\text{O}_3$ grains was determined on a minimum area of 0.1 mm^2 from the center of the samples using scanning electron microscopy (SEM, Phenom ProX; Phenom-World B.V., Eindhoven, The Netherlands). SEM micrographs obtained from backscattered electrons were used to detect $\beta\text{-Al}_2\text{O}_3$ grains. The contrast, brightness, and sharpness of the obtained SEM images were adjusted to improve the visibility of the second phases. The size of the $\beta\text{-Al}_2\text{O}_3$ grains was measured from the SEM images (length and thickness) and an area fraction was estimated. Considering the stereology of randomly oriented, platelet shaped $\beta\text{-Al}_2\text{O}_3$ grains [100] the estimated area fraction was assumed to be equal to the volume fraction of $\beta\text{-Al}_2\text{O}_3$ in the samples. The chemical composition of the second phase was determined by energy dispersive x-ray spectroscopy (EDS, Phenom ProX; Phenom-World B.V., Eindhoven, The Netherlands). Note that the samples for SEM analysis were not coated with a conducting material since such coatings can obscure second phases.

5.3 Results

Figure 5.1 shows an example of second phases observed in sintered Bayer alumina. The second phase grains are platelet shaped, as evident from the high aspect ratio of the second phase grains. Initial studies showed that the detection of this second phase is challenging because no second phase grains are observed after thermal etching and in unetched samples the second phase grains can only be observed if a backscattered electron detector is used, as seen in Figure 5.1. Furthermore, coatings that are typically applied on insulating samples to achieve sufficient electrical

conductivity for SEM analysis can obscure the second phase grains, and therefore the samples were not coated.

Figure 5.2 shows the XRD pattern of a 99% dense Bayer alumina sample doped with 1060 ppm Na₂O and 582 ppm SiO₂ and sintered at 1525°C for 5 h. The small amount of second phase was indexed and identified as β -Al₂O₃ (PDF number: 98-001-2968). The estimated amount of β -Al₂O₃ from Rietveld analysis is 0.6 wt.% and EDS analysis reveals that the β -Al₂O₃ grains contain higher concentrations of MgO and Na₂O relative to the surrounding matrix. As noted earlier, the Al₂O₃-Na₂O-MgO phase diagram shows that β -Al₂O₃ can dissolve up to 2.5 wt% MgO [48].

Samples were heated for up to 8 h at 1525°C to determine when β -Al₂O₃ forms during sintering and Figure 5.3 shows micrographs of MgO-doped Bayer alumina samples doped with 560 ppm Na₂O and 82 ppm SiO₂ after heating for 0 h, 1 h, and 8 h. The relative densities of the samples were 92%, 97%, and 99%, respectively. It can be seen that the β -Al₂O₃ grains are 4 - 10 μ m long and their size does not change as a function of sintering time. However the number of β -Al₂O₃ grains increases with increasing sintering time. To estimate how the amount of β -Al₂O₃ changes as a function of sintering time and powder chemistry the number density of β -Al₂O₃ grains per unit area was determined.

The kinetics of β -Al₂O₃ formation in MgO-doped Bayer alumina is shown in Figure 5.4 as a function of powder chemistry. Most β -Al₂O₃ grains form within the first hour at 1525°C, and after that the number density of β -Al₂O₃ grains does not change as a function of hold time for all chemistries. For example, samples with 560 ppm Na₂O and 82 ppm SiO₂ form \sim 320 β -Al₂O₃ grains/mm² after 0 h at 1525°C (92% relative density), and the amount of β -Al₂O₃ increases to >1000 β -Al₂O₃ grains/mm² after 1 h at 1525°C (97% relative density), but does not change upon further heating. Samples with 560 ppm Na₂O and 182 ppm SiO₂ form \sim 130 β -Al₂O₃ grains/mm² after 0 h at 1525°C (89% relative density), and \sim 600 β -Al₂O₃ grains/mm² after 1 h at 1525°C (97% relative density). Samples with lower Na₂O and/or higher SiO₂ concentrations form less β -Al₂O₃ grains for all hold times, as seen in Figure 5.4.

Figure 5.5 shows the number density of β -Al₂O₃ grains in MgO-doped Bayer alumina samples with 82 ppm SiO₂, and Figure 5.6 shows some of the corresponding micrographs. In samples with 60 and 185 ppm Na₂O β -Al₂O₃ grains with a length

of 3 - 13 μm form, and if the Na_2O concentration is increased to 560 and 1060 ppm, the number density of $\beta\text{-Al}_2\text{O}_3$ increases and the length of the $\beta\text{-Al}_2\text{O}_3$ grains decreases to 4 - 10 μm and 2 - 7 μm , respectively.

The number density of $\beta\text{-Al}_2\text{O}_3$ in MgO -doped Bayer alumina decreases for all Na_2O concentrations if the SiO_2 concentration is increased, as shown in Figure 5.7a, whereas the size of the $\beta\text{-Al}_2\text{O}_3$ grains increases with increasing SiO_2 concentration, as seen when the micrographs in Figure 5.5 are compared to the micrographs in Figure 5.8. For example, samples with 185 ppm Na_2O and 82 ppm SiO_2 form 3 - 13 μm long $\beta\text{-Al}_2\text{O}_3$ grains (Figure 5.5a) and if the SiO_2 concentration is increased to 182 ppm the number density of $\beta\text{-Al}_2\text{O}_3$ grains decreases significantly, and the $\beta\text{-Al}_2\text{O}_3$ grains are $\sim 15 \mu\text{m}$ long (Figure 5.8a). No $\beta\text{-Al}_2\text{O}_3$ was observed in samples with 582 ppm SiO_2 and Na_2O concentrations of 60-560 ppm.

The effect of Na_2O and SiO_2 shows that the formation of $\beta\text{-Al}_2\text{O}_3$ is a function of the $\text{Na}_2\text{O}/\text{SiO}_2$ ratio. Figure 5.7b shows that no $\beta\text{-Al}_2\text{O}_3$ forms in MgO -doped Bayer alumina samples with $\text{Na}_2\text{O}/\text{SiO}_2$ ratios < 0.7 , and only a small amount of $\beta\text{-Al}_2\text{O}_3$ forms in samples with $\text{Na}_2\text{O}/\text{SiO}_2$ ratios of 0.7 - 2.0. For higher $\text{Na}_2\text{O}/\text{SiO}_2$ ratios the amount of $\beta\text{-Al}_2\text{O}_3$ increases linearly to as much as ~ 1880 grains/ mm^2 for a $\text{Na}_2\text{O}/\text{SiO}_2$ ratio of ~ 13 .

A theoretical volume fraction of $\beta\text{-Al}_2\text{O}_3$ was estimated based on the chemical formula of $\beta\text{-Al}_2\text{O}_3$ ($\text{Na}_2\text{O}\cdot 11\text{Al}_2\text{O}_3$) and the amount of Na_2O in the samples, as seen in Table 5.2. It can be seen that the theoretically estimated amount of $\beta\text{-Al}_2\text{O}_3$ that can form based on the amount of Na_2O in the samples is higher than the observed amount of $\beta\text{-Al}_2\text{O}_3$ in the samples. This difference can be explained by Na_2O volatilization during sintering, as shown in Chapter 3. Taking into account that $\sim 40\%$ of the Na_2O volatizes during heating (Figure 3.12 Chapter 3), the expected amount of $\beta\text{-Al}_2\text{O}_3$ in the samples is close to the observed amount of $\beta\text{-Al}_2\text{O}_3$, as seen in Table 5.2.

5.4 Interpretation and mechanisms of $\beta\text{-Al}_2\text{O}_3$ formation

It was shown by TEM and EDS analysis that insoluble impurities and dopants such as Na_2O , MgO , CaO and SiO_2 segregate to the grain boundaries during sintering

of alumina, and second phases can form if a critical impurity concentration in the grain boundaries is exceeded [1]. For example, a segregation and precipitation map for MgO in ultrahigh purity alumina, which predicts the formation of spinel as a function of MgO concentration and grain size, was proposed in the literature [1]. However, the presence of several impurities and dopants in Bayer alumina can affect the critical concentrations of impurities and dopants in grain boundaries, and the formation of second phases can strongly depend on the concentration and ratios of several impurities and dopants. For example, in previous chapters it was shown that SiO₂, MgO, and Na₂O form a liquid grain boundary phase during sintering of Bayer alumina, and the critical concentration of Na₂O to form β -Al₂O₃ depends on the amount of siliceous glass phase that forms, since the glass phase consists of 20-30 mol% Na₂O. Furthermore, it was shown that MgO and SiO₂ co-dissolve into the alumina grains during final stage sintering, which reduces the concentration of SiO₂ in the grain boundaries and thus the amount of Na₂O that can be dissolved in the glass phase.

The above discussion indicates that MgO plays an important role for β -Al₂O₃ formation in Bayer alumina. To gain insight into how MgO affects β -Al₂O₃ formation an additional set of experiments with a Bayer alumina with 2 ppm MgO ("MgO-free") was completed. The powder was doped to concentrations between 2 and 1002 ppm MgO and different Na₂O and SiO₂ concentrations of up to 1029 ppm and 1000 ppm, respectively, and heated at 1525°C for 3 h. Figures 5.8 and 5.9 show the influence of powder chemistry on the number density of β -Al₂O₃ grains and microstructures, respectively. It can be seen that no β -Al₂O₃ forms in samples with 2 ppm MgO and 29 ppm Na₂O, but the amount of β -Al₂O₃ increases with increasing MgO concentration (Figure 5.9a).

In the Bayer alumina powder with 2 ppm MgO no second phase formation was observed for Na₂O concentrations of 29 ppm, and only a very small amount (\sim 10 grains/mm²) of β -Al₂O₃ forms in samples with 529 ppm Na₂O, which indicates that most Na₂O is segregated to the grain boundaries, but the Na₂O concentration is not sufficient to form β -Al₂O₃. Note that the presence of 103 ppm SiO₂ in the Bayer alumina powder with 2 ppm MgO affects the formation of β -Al₂O₃. When the Na₂O concentration is increased to 1029 ppm the amount of β -Al₂O₃ increases significantly to 470 grains/mm² (Figure 5.9b), which indicates that grain boundaries supersaturate during sintering and β -Al₂O₃ forms.

No or only a very small amount of β -Al₂O₃ forms in samples with 2 ppm MgO if the SiO₂ concentration is increased to 203 ppm or higher. It was demonstrated by high resolution TEM and EDS that SiO₂ segregates to the grain boundaries and forms an amorphous glass phase. With increasing SiO₂ concentration in the sample the glass phase can dissolve more Na₂O without precipitating β -Al₂O₃, and, therefore, increasing SiO₂ in a sample decreases the amount of β -Al₂O₃. This hypothesis is supported by an additional experiment with an ultrahigh purity alumina (AKP-50) with only 11 ppm SiO₂. The powder was doped to 502 ppm Na₂O and heated at 1525°C for 0 h and it can be seen in Figure 5.11 that a substantial amount of β -Al₂O₃ (\sim 1100 grains/mm²) has formed. In Bayer alumina samples with 529 ppm Na₂O, 2 ppm MgO, and 103 ppm SiO₂ form only \sim 10 β -Al₂O₃ grains/mm².

When the MgO concentration in Bayer alumina is increased to 252 ppm or higher β -Al₂O₃ forms at a Na₂O concentration as low as 29 ppm. It is hypothesized that more β -Al₂O₃ forms with increasing MgO concentration because MgO removes SiO₂ from the grain boundaries by co-dissolving into the alpha alumina matrix during final stage sintering, as explained earlier. This co-dissolution mechanism significantly decreases the amount of Na₂O that can be dissolved in the liquid grain boundary phase, leading to the nucleation and growth of β -Al₂O₃.

If it is assumed that MgO and SiO₂ form the defect complex proposed earlier, and if it is assumed that MgO and SiO₂ co-dissolve at equal amounts and that all MgO is consumed by this process, MgO-doped powder samples (380 ppm MgO) with 82 and 182 ppm SiO₂ do not have any SiO₂ left in the grain boundaries. This reduction in the amount of SiO₂ in the grain boundaries reduces the solubility of Na₂O significantly, leading to the precipitation of β -Al₂O₃. Samples with 582 ppm SiO₂ have 202 ppm SiO₂ left in the grain boundaries after 380 ppm MgO and SiO₂ co-dissolve into the alumina lattice, and the solubility of Na₂O in the liquid grain boundary phase is still high enough that only few β -Al₂O₃ grains form in this sample.

The co-dissolution of SiO₂ and MgO into the alumina lattice and the formation of the majority of the β -Al₂O₃ grains happens at the same time, between 0 and 3 h at 1525°C at relative densities $>$ 90%, which supports the hypothesis that β -Al₂O₃ nucleates and grows as a result of supersaturation of the liquid grain boundary phase when MgO reduces the SiO₂ concentration in the grain boundaries. However,

samples with 560 ppm Na₂O and 82 ppm SiO₂ form more β -Al₂O₃ than samples with 560 ppm Na₂O and 182 ppm SiO₂, even though no SiO₂ should be left in the grain boundaries of both samples. One reason could be that not all 380 ppm MgO and SiO₂ are consumed by this co-dissolution process, and a small amount SiO₂ might remain on the grain boundaries. Another possible explanation is that MgO has an additional effect on the formation of β -Al₂O₃ in α -Al₂O₃. It has been reported that MgO supports the formation of β -Al₂O₃ in alumina, and samples with 560 ppm Na₂O and 82 ppm SiO₂ have 100 ppm more MgO left in the grain boundaries than samples with 560 ppm Na₂O and 182 ppm SiO₂. MgO might facilitate the formation of β -Al₂O₃ since EDS analysis shows the presence of MgO in the β -Al₂O₃ grains.

5.5 Summary

The effect of powder chemistry on the formation of β -Al₂O₃ in α -Al₂O₃ was investigated. The number density of β -Al₂O₃ grains increases with increasing Na₂O and MgO concentrations and decreases with increasing SiO₂ concentration, whereas the size of the β -Al₂O₃ grains decreases with increasing Na₂O and MgO concentration and increases with increasing SiO₂ concentration. The majority of β -Al₂O₃ grains form within the first hour at 1525°C at densities >90%, at the same stage at which MgO and SiO₂ were shown to co-dissolve into the α -Al₂O₃ grains. It was concluded that the mechanism of β -Al₂O₃ formation in Bayer alumina is by precipitation from the liquid grain boundary phase. The liquid glass phase in the grain boundaries supersaturates with Na₂O when the amount of SiO₂ in the grain boundaries is reduced by the co-dissolution of MgO and SiO₂ into the alumina lattice, which leads to the precipitation of β -Al₂O₃.

Table 5.1. Physical and chemical characteristics of the alumina powder used in this study.

	MgO-doped
	Bayer alumina
BET (m^2/g)	7.3
D_{50} (μm)	0.4
	ICP (ppm)
Al_2O_3	99.92%
SiO_2	82
Na_2O	60
Fe_2O_3	140
CaO	51
TiO_2	8
MgO	380

Table 5.2. Estimated amount of β -Al₂O₃ in MgO-doped Bayer alumina samples after 3 h at 1525°C.

Concentration of Na ₂ O in the sample (ppm)	Theoretical vol.% of β -Al ₂ O ₃		Measured amount of β -Al ₂ O ₃ 3h 1525°
	No Na ₂ O volatizes	Assuming 40 % of Na ₂ O volatizes	
60	0.14	0.08	0.18
185	0.42	0.25	0.25
310	0.71	0.43	0.38
560	1.28	0.77	0.65
1060	2.42	1.45	0.49

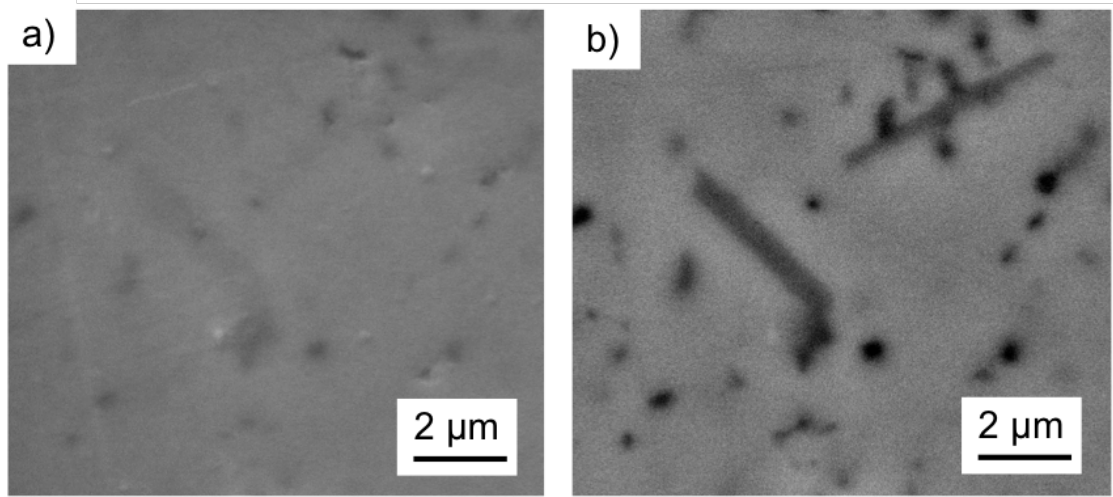


Figure 5.1. Micrographs of MgO-doped Bayer doped with 560 ppm Na₂O and 82 ppm SiO₂ after 3 h at 1525°C obtained using a) a secondary electron detector and b) a backscattered electron detector.

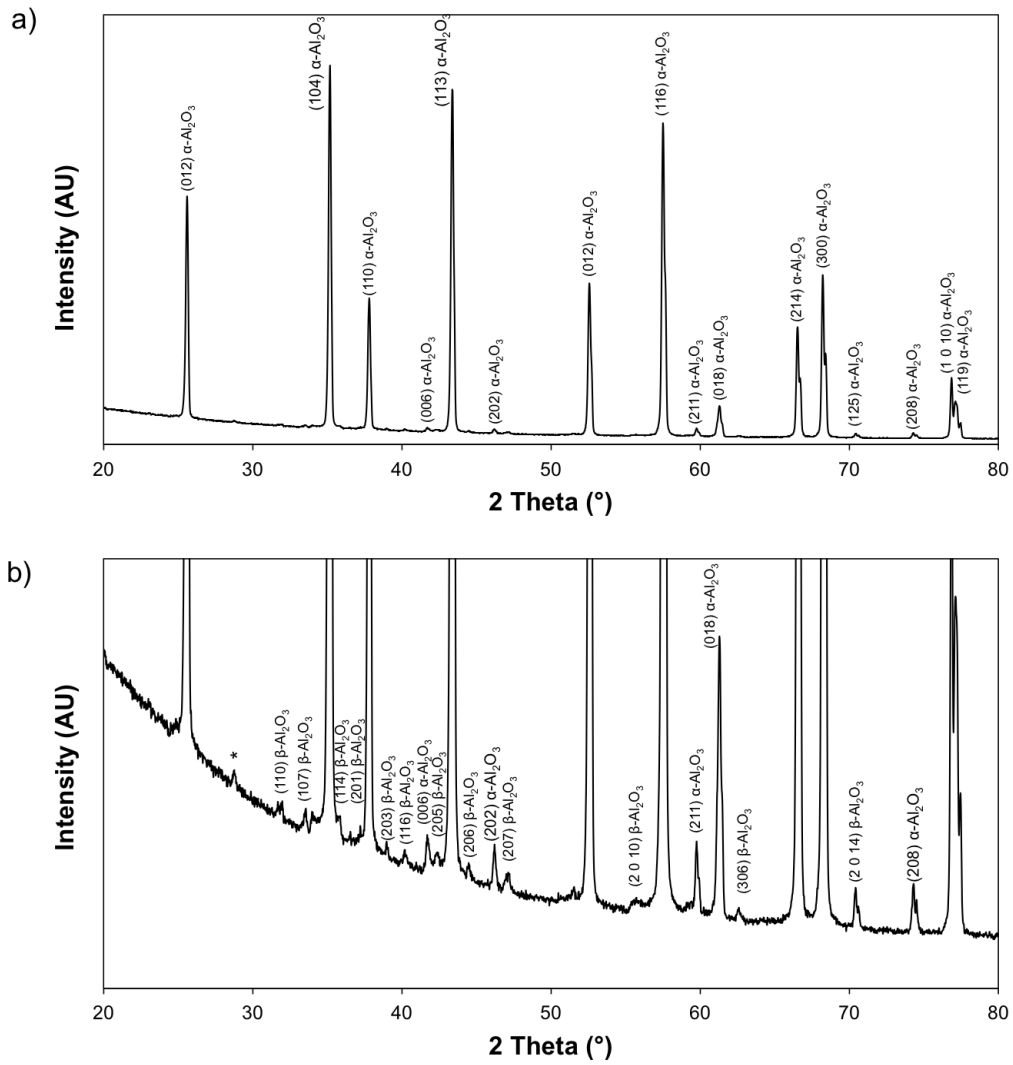


Figure 5.2. a) XRD pattern and b) zoomed-in XRD pattern of a sample with 1060 ppm Na₂O, 82 ppm SiO₂, and 380 ppm MgO after sintering at 1525°C for 5 h. All observed peaks except for one (*) can be assigned to either α -Al₂O₃ or β -Al₂O₃.

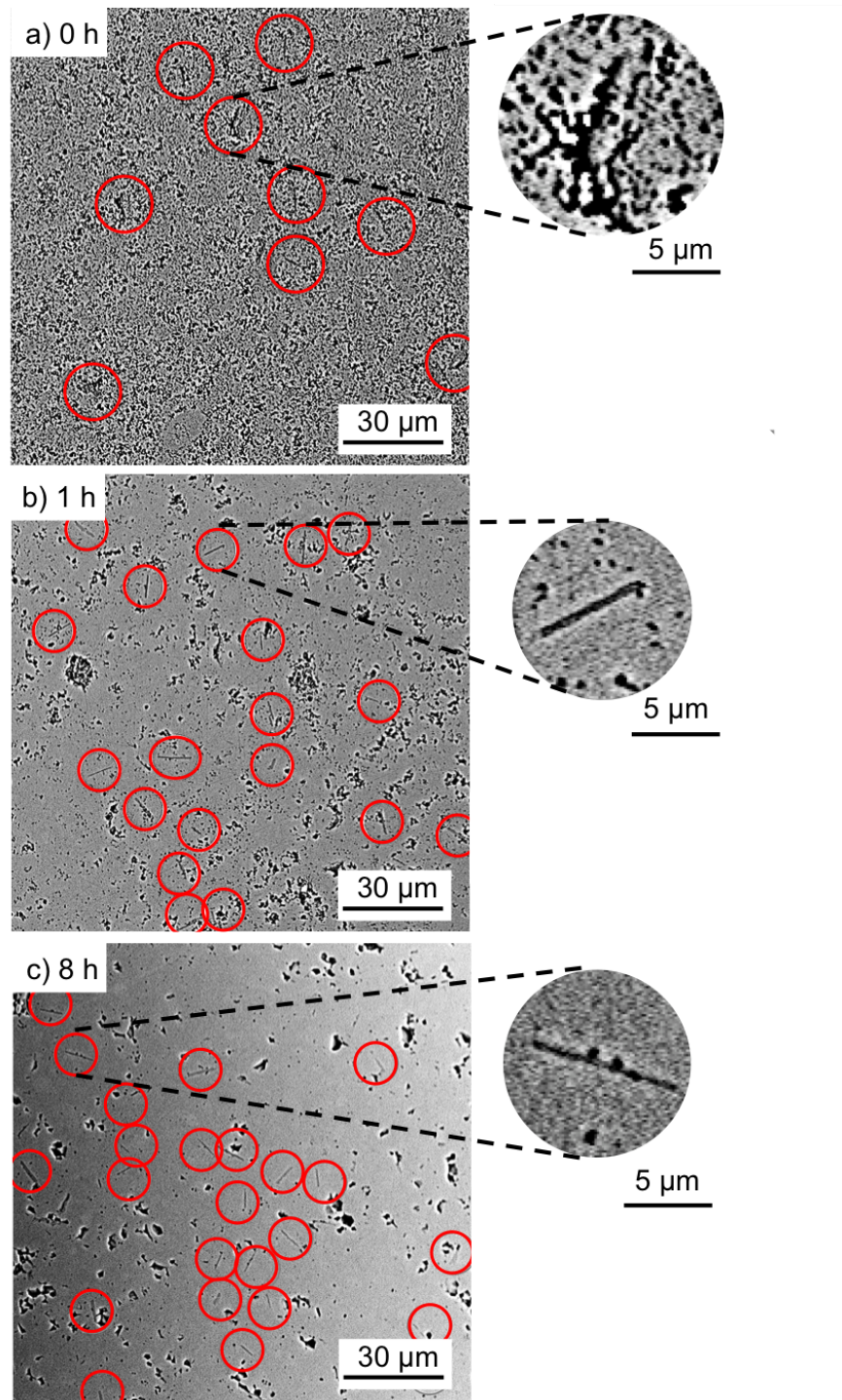


Figure 5.3. Micrographs showing β -Al₂O₃ grains (red circles) in MgO-doped Bayer alumina samples with 82 ppm SiO₂ and 560 ppm Na₂O after sintering at 1525°C for a) 0 h, b) 1 h, and c) 8 h.

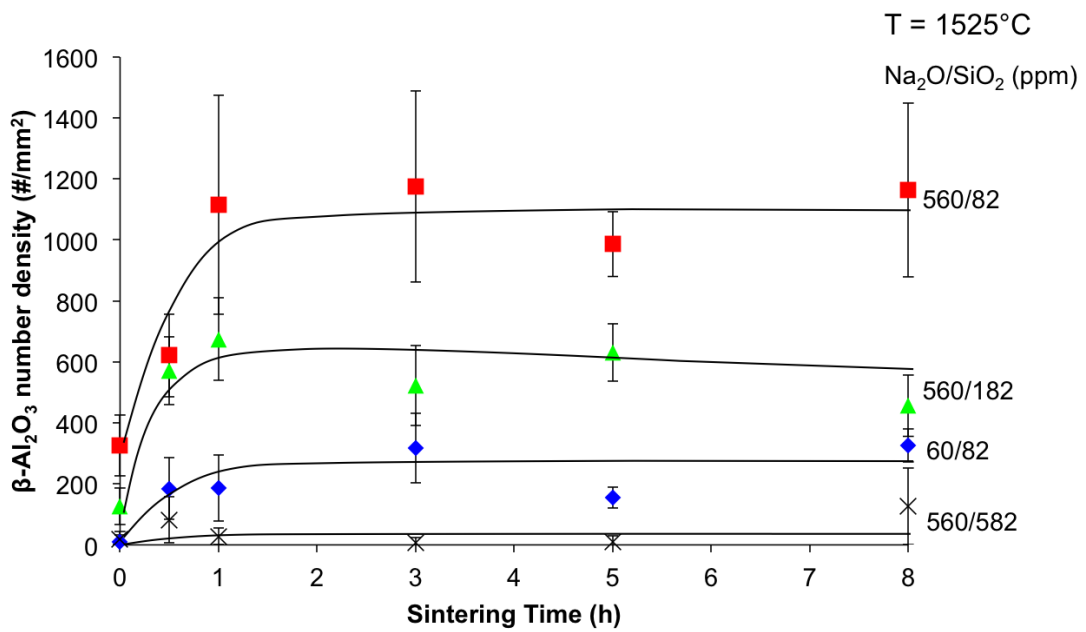


Figure 5.4. Kinetics of $\beta\text{-Al}_2\text{O}_3$ formation for different powder chemistries of MgO-doped powder samples.

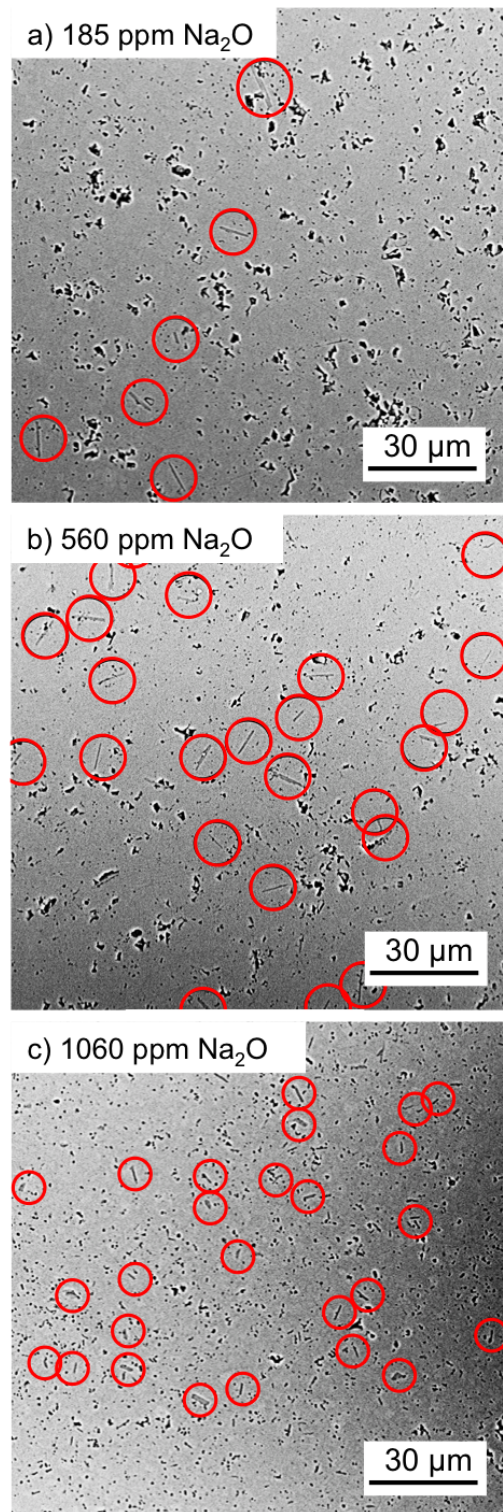


Figure 5.5. Micrographs showing β -Al₂O₃ grains (red circles) in MgO-doped Bayer alumina samples with 82 ppm SiO₂ and a) 185 ppm Na₂O, b) 560 ppm Na₂O, and c) 1060 ppm Na₂O after sintering at 1525°C for 3 h.

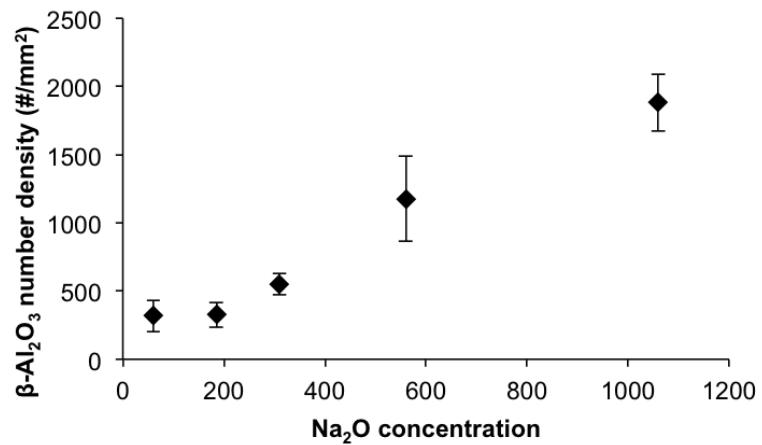


Figure 5.6. Formation of $\beta\text{-Al}_2\text{O}_3$ a function of Na_2O concentration in MgO-doped Bayer alumina.

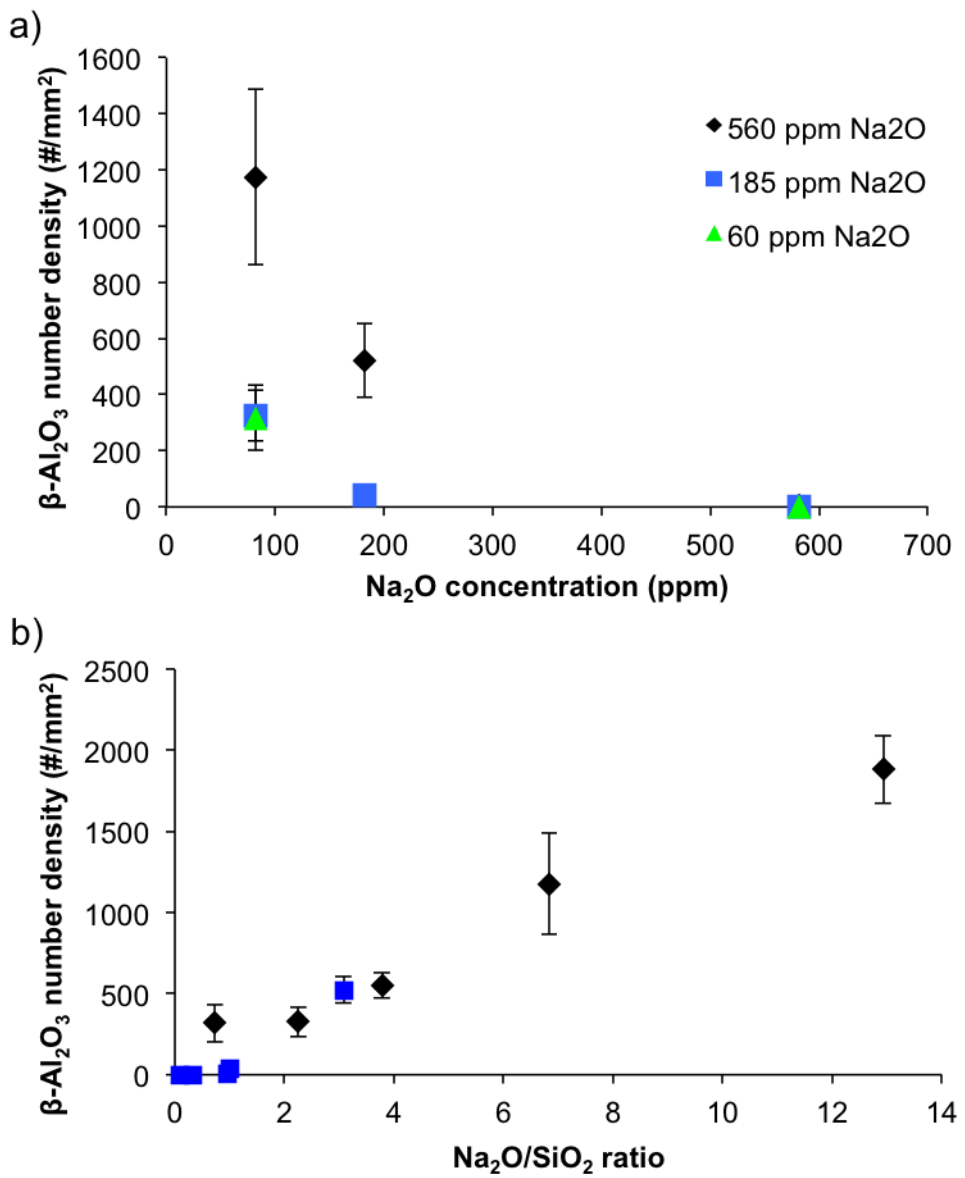


Figure 5.7. Formation of β -Al₂O₃ in MgO-doped powder samples a function of a) SiO₂ concentration for different Na₂O concentrations, and b) Na₂O/SiO₂ ratio. In b) the black diamonds are samples with 82 ppm SiO₂ and the blue squares are samples with 182 and 582 ppm SiO₂.

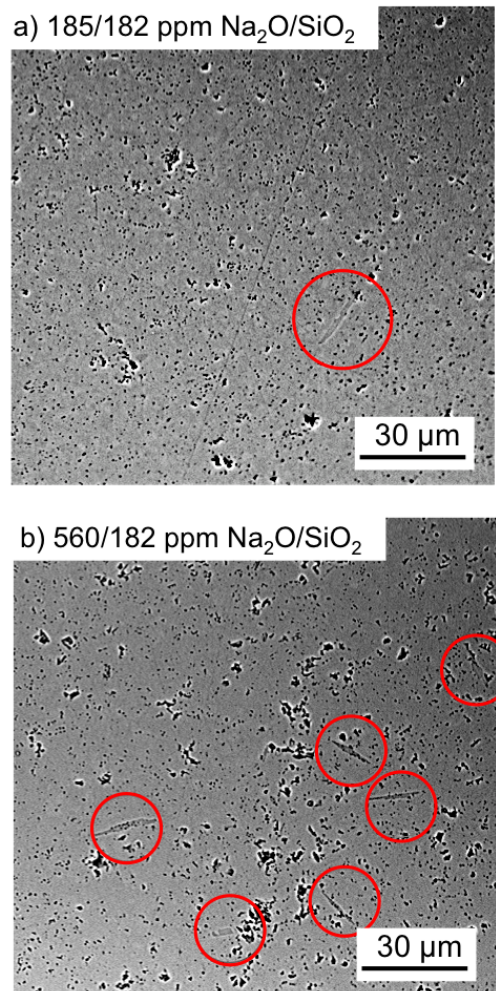


Figure 5.8. Micrographs showing β -Al₂O₃ grains (red circles) in MgO-doped Bayer alumina samples with a) 185/182 ppm Na₂O/SiO₂ and b) 560/182 ppm Na₂O/SiO₂ after sintering at 1525°C for 3 h.

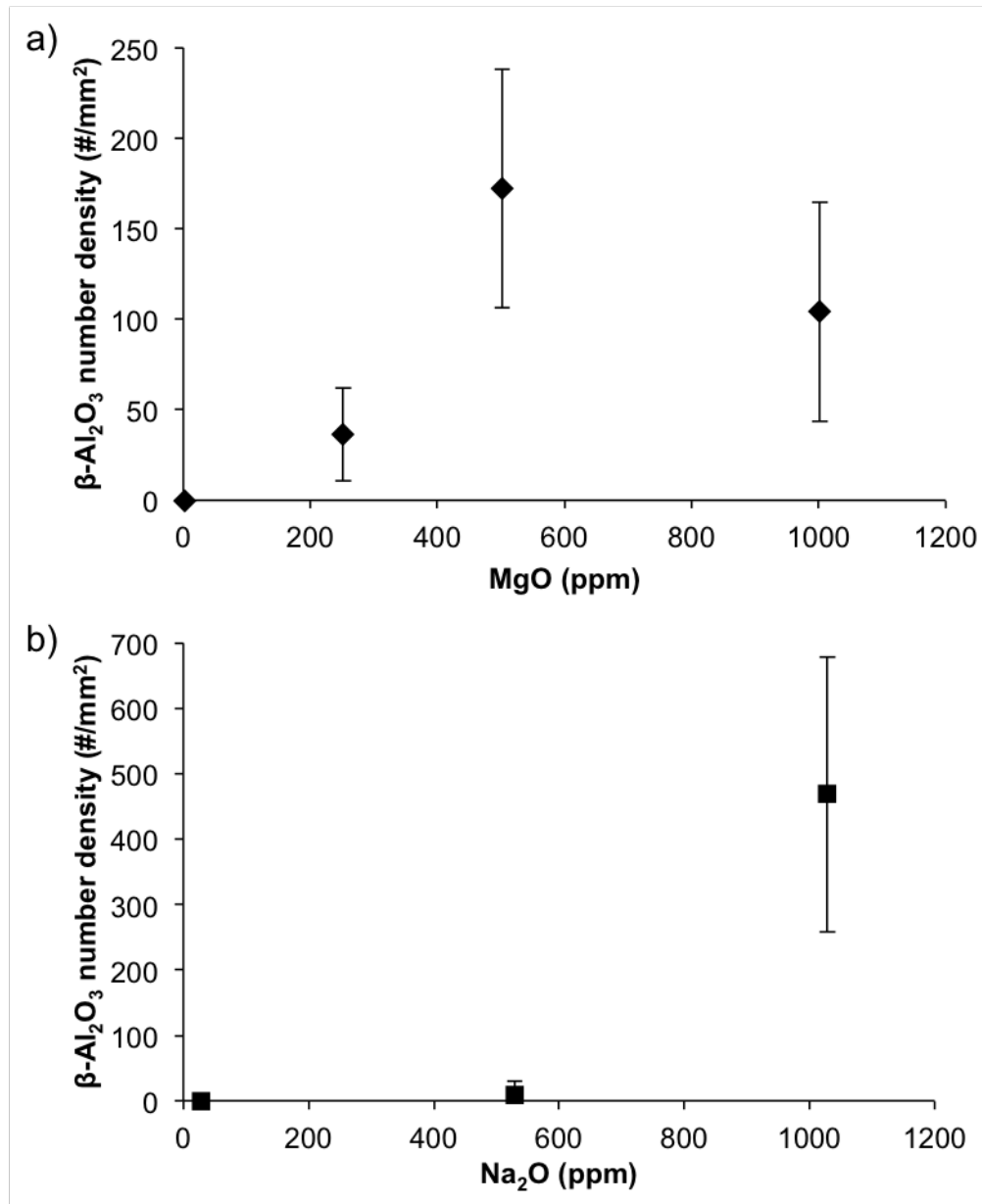


Figure 5.9. Formation of β -Al₂O₃ in MgO-free powder samples as a function of a) MgO concentration (29 ppm Na₂O) and b) Na₂O concentration (2 ppm MgO) after 3 h at 1525°C.

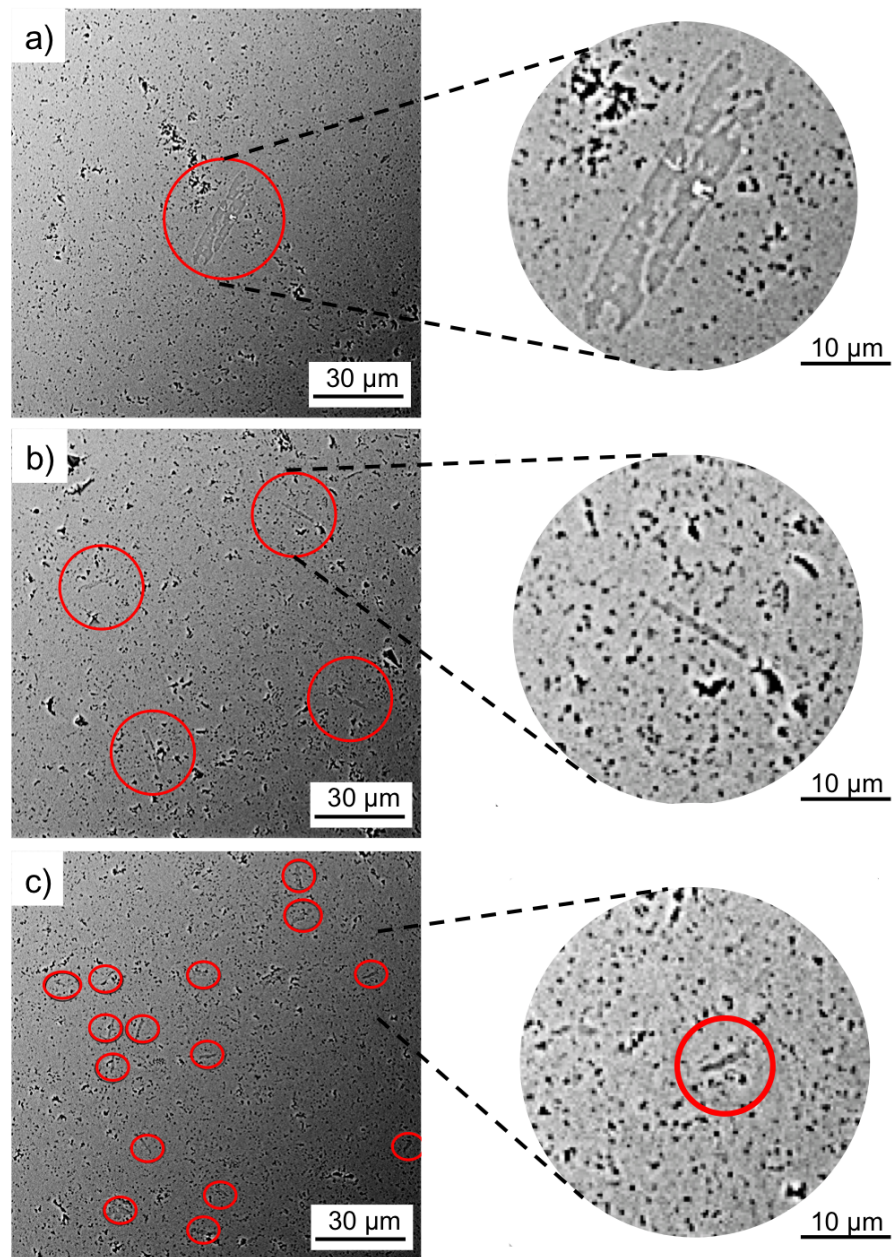


Figure 5.10. Micrographs showing β -Al₂O₃ grains (red circles) in Bayer alumina samples with a) 1002 ppm MgO, 1000 ppm SiO₂, 29 ppm Na₂O, b) 2 ppm MgO, 1000 ppm SiO₂, 1029 ppm Na₂O, c) 1002 ppm MgO, 1000 ppm SiO₂, 1029 ppm Na₂O after 3 h at 1525°C.

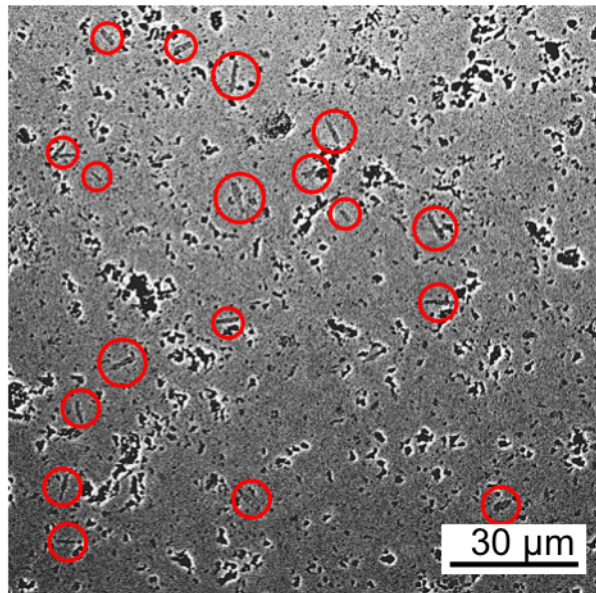


Figure 5.11. Micrograph showing β -Al₂O₃ grains (red circles) in an ultra high purity powder sample with 502 ppm Na₂O, 2 ppm MgO, and 11 ppm SiO₂ after sintering at 1525°C for 3 h.

Chapter 6 |

A Critique of the Master Sintering Curve Analysis of Sintering Processes

6.1 Introduction

The master sintering curve (MSC) approach was developed by Su and Johnson [101] to generalize the densification behavior of a sintering powder with a single curve for the entire sintering time/temperature profile. The MSC approach is based on a combined-stage sintering model developed by Hansen et al [102], given as:

$$\frac{1}{\rho} \frac{d\rho}{dt} = \frac{3\gamma\Omega}{k_B T} \left(\frac{\delta D_b \Gamma_b}{G^4} + \frac{D_v \Gamma_v}{G^3} \right) \quad (6.1)$$

where ρ is relative density of the powder compact, $d\rho/dt$ is densification rate, γ is surface energy, Ω is molar volume, k_B is Boltzmann's constant, T is absolute temperature, G is grain size, D is diffusion coefficient, δ is grain boundary thickness, and Γ is a geometric scaling factor. The subscripts b and v represent grain boundary and volume diffusion mechanisms, respectively. The MSC was originally derived to simplify the combined-stage sintering model (Eq. 6.1) to account for only a single diffusion mechanism, and by considering diffusion as thermally-activated with an activation energy Q . The resulting equation is given as:

$$\frac{1}{\rho} \frac{d\rho}{dt} = \frac{3\gamma\Omega}{k_B T} \left(\frac{D\Gamma}{G^n} \right) \quad (6.2)$$

where

$$D = D_0 e^{-Q/RT} \quad (6.3)$$

and R is the ideal gas constant. Eq. 6.2 is re-written to collect microstructural parameters on the left hand side and temperature dependent parameters on the right hand side:

$$\frac{k_B G^n}{3\rho\gamma\Omega\Gamma D_0} \frac{d\rho}{dt} = \frac{1}{T} \exp\left(-\frac{Q}{RT}\right) = \frac{d\Theta}{dt} \quad (6.4)$$

Eq. 6.4 can be integrated to give:

$$\frac{k_B}{\gamma\Omega\Gamma D_0} \int_{\rho_0}^{\rho} \frac{(G(\rho))^n}{3\rho\Gamma(\rho)} d\rho = \int_0^t \frac{1}{T} \exp\left(-\frac{Q}{RT}\right) dt = \Theta \quad (6.5)$$

Equation 6.5 describes the sintering behavior for an arbitrary time-temperature profile, and the integral over this profile with respect to time is termed the work of sintering Θ . The MSC is obtained by plotting ρ versus Θ . The left hand side of Eq. 6.5 is not solved, because many of the parameters are unknown. However, as long as these parameters are independent of time and temperature, data plotted in this way will collapse into a single continuous curve for a single value of Q . It is interesting to note that the MSC analysis is independent of the sintering mechanism and, as a generalized model, was applied to other thermally activated process such as grain growth [103] and binder decomposition [104, 105].

In practice, Q is a fitting parameter for which the best-fit MSC is obtained over a range of heating rates by determining the minimum mean residual. Assuming arbitrary values for Q in Eq. 6.5, the mean residual square is calculated by [106]

$$\text{Mean residual square} = \sqrt{\frac{1}{\rho_s - \rho_0} \int_{\rho_0}^{\rho_s} \frac{\sum_{i=1}^N \left(\frac{\Theta_i}{\Theta_{avg}} - 1 \right)^2}{N} d\rho} \quad (6.6)$$

where N is the number of experimental data points gathered at a series of heating rates and a sintered density ρ_s , and Q_{avg} is the average of all Q_i over N . The Q value that yields the minimum mean residual square is the Q value at which the MSC trajectories obtained from the densification curves at different heating rates yield the best fit and converge onto a single curve. Because of the mechanistic nature of the model, the Q parameter is usually referred to in the literature as the

'activation energy' for sintering.

MSC analysis has been applied to ceramic powders formed and densified by a variety of techniques. For high purity alumina, the reported Q values vary drastically, as seen in Table 6.1. In Su and Johnson's original work [101], Q values of 440 and 488 kJ/mol were determined by minimum mean residuals and iso-strain analysis, respectively, for an ultrafine, ultrahigh purity alumina (AKP-50, Sumitomo Chemical America, Inc.). These results showed that the activation energy obtained from minimum mean residuals is in close agreement with the activation energies determined by conventionally used methods. Using the same powder, Tatami et al. [107] determined a Q of 555 kJ/mol, and when the powder was doped with 2000 ppm MgO, a Q of 880 kJ/mol was determined. Pouchly et al. [108] estimated the Q of two different ultrahigh purity alumina powder graded (Taimicron TM-DAR, Taimei Chemicals and RC-HP DBM, Reynolds Chemicals) to be 770 and 640 kJ/mol, respectively, and attributed the difference in Q to the difference in particle size of 110 nm and 240 nm, respectively. Aminzare et al. [109], reported Q values of 700 and 605 kJ/mol for alumina (Taimicron TM-DAR, Taimai Chemicals) samples prepared by dry pressing and pressure filtration, respectively. Using the same alumina powder grade (Taimicron TM-DAR, Taimai Chemicals), Guillon and Langer [110] reported a Q of 290 kJ/mol for Al_2O_3 densified by spark plasma sintering (SPS). They attributed the lower Q value to the effect of the high heating rates of 35 - 150°C/min during SPS. Q values of up to 1064 kJ/mol were reported by Shao et al. [111] for granulated and dry pressed alumina powder (350 nm, 99.9%, Dalian Luming Nanometer Material Ltd.). They explained the higher Q values as an effect of slower heating rates (0.5 and 5°C/min) on densification.

The effect of heating rate on densification was explained by Harmer and Brook [112] as due to the relative time the material is heated under conditions favoring surface and grain boundary diffusion. They reasoned that a slow heating process favors surface diffusion and particle coarsening because surface diffusion usually has a lower activation energy than densification mechanisms such as grain and volume diffusion. Samples heated at slow rates spend relatively longer times at lower temperatures and, therefore, experience more particle coarsening prior to reaching the temperatures where densification occurs. Thus, the sintering driving force provided by surface area is higher during the densification stage when ceramics are fired at higher heating rates since these samples do not undergo as much coarsening

prior to densification. In MSC analysis, these relative changes in mechanism result in lower Q values at faster heating rates. However, it is assumed in the MSC analysis that sintering occurs by a single mechanism for the heating conditions used to collect densification data. Since data for MSC analysis is performed by heating samples at different heating rates, the contributions from surface diffusion and grain boundary diffusion vary, and it is questionable if the Q values obtained can be used for mechanistic interpretations. Furthermore, it is not apparent what other parameters, additionally to the heating rate, cause the large variability of the reported Q values.

In this work we investigate how forming techniques and powder chemistry affect the Q parameter and the shape of the MSC for a commercial specialty alumina powder. We explore how forming process-induced differences in relative green density, microstructural homogeneity and shrinkage anisotropy affect the value of Q . We also investigate how the assumption of a constant microstructure (i.e., grain size) at high density affects the MSC fit and Q value. A series of Na₂O-doped samples were studied to determine how changes in densification mechanism affect the value of Q . Based on these experiments, we discuss the limits and accuracy of the MSC approach and then determine how MSC can be used in a constructive, practical way to predict the sintering of a specific powder.

6.2 Experimental Procedure

To examine the impact of the forming technique on the MSC, we prepared undoped alumina (CT3000 LS SG, Almatis, Inc., Leetsdale, PA) samples by dry pressing, slip casting and tape casting. The powder was a specialty reactive alumina (99.8%) with an average particle diameter of $\sim 0.3 \mu\text{m}$. Two sets of samples were prepared by uniaxial dry pressing. For one set, the as-received powder was sieved to -106 μm and uniaxially dry pressed at 30 MPa. The powder handling for the second set was designed to produce a soft granule powder by dispersing it in ethanol with 5 wt.% polyethylene glycol (PEG 600, Alfa Aesar, Ward Hill, MA, USA). After ball milling for 24 h, the dried powder was sieved to -106 μm and samples were lightly pressed at 30 MPa. For uniaxial dry pressing a bar shaped die was used, where the long axis was perpendicular to the pressing direction to minimize density gradients. Both sample types were iso-pressed at 200 MPa after removing the

organic processing aids by heating at 600°C for 12 h in air.

For tape casting, a slurry was prepared by ball milling 26 vol.% alumina powder with 29.7 vol.% xylene (ACS Reagent grade, Avantor Performance Materials, Inc., Center Valley, PA, USA), 32.3 vol.% ethanol (200 proof), and 2.1 vol.% blown menhaden fish oil (Grade Z-3, Tape Casting Warehouse, Morrisville, PA, USA). After 24 h, 5.2 vol.% polyvinyl butyral (PVB B-98, Tape Casting Warehouse, Morrisville, PA, USA), 2.3 vol.% polyalkylene glycol (PAG, UCON50HB2000, Tape Casting Warehouse, Morrisville, PA, USA) and 2.5 vol.% butyl benzyl phthalate (BBP S-160, Tape Casting Warehouse, Morrisville, PA, USA) were added and the mixture was ball milled for another 24 h. Subsequently 1 drop of cyclohexane (99+, Alfa Aesar, Ward Hill, MA, USA) per 20 g of alumina powder was added and the slurry was stirred for an additional 45 min. The slurry was tape cast on a silicone-coated MylarTM carrier tape using a doctor blade gap height of 305 µm. After drying, the tape was cut, stacked, uniaxially pressed at 70°C for 10 min at minimal pressure to tack the layers together, and then isostatically laminated at 74°C and 20 MPa for 30 min.

For non-aqueous slip casting, 28.9 vol.% powder was dispersed in xylene with 3.8 vol.% Menhaden fish oil, ball milled for 24 h, and slip cast. For aqueous slip casting 44.6 vol.% alumina powder was dispersed in deionized water with 6.3 vol.% Darvan C (R. T. Vanderbilt Company, Inc., Norwalk, CT, USA). The pH of the Darvan and water mixture was adjusted to 11 using 5 M NH₄OH before the alumina powder was added. The slurry was ball milled for 24 h and then slip cast. In both cases the mold consisted of a PVC tube (20 mm diameter) on a plaster of Paris plate.

The polymer processing aids were burned out of all samples by heating at 600°C for 12 h in air. All samples were cold isostatically pressed at 200 MPa (CIP, Autoclave Engineers, Erie, PA). The samples were subsequently cut and ground into 3 x 3 x 15 mm³ bars for dilatometry studies. The long axis of the dilatometry samples is perpendicular to the casting direction during slip casting and parallel to the casting direction for tape cast samples. The bars were heated to 1525°C or 1595°C at 5, 10, and 20°C/min in a thermomechanical analyzer (TMA; Linseis PT1600, Robbinsville, NJ) and held at temperature for 5 min to record the linear shrinkage of the samples. The thermal expansion of the test fixture was removed by blank experiments, and the thermal expansion contribution of the samples to the

dilatometry curves was subtracted from the dimensions measured in-situ using the cooling curves of the samples measured in the TMA. To ensure accurate shrinkage values the initial nonzero value of the dilatometry data was eliminated, as described in the literature [106].

To examine how changes in chemistry affect the MSC analysis, we studied a series of non-aqueous slip cast Na₂O-doped aluminas. The alumina powder was doped with up to 1000 ppm Na₂O using sodium acetate (NaC₂H₃O₂*3H₂O, ACS grade, BDH, West Chester, PA). The detailed doping procedure is reported in chapter 2.

6.3 Results and Discussion

6.3.1 The effect of forming on Q

During initial studies, we observed different degrees of anisotropic shrinkage as a function of the forming method. For example, the dilatometry curves of the non-aqueous slip cast samples during heating to 1525°C at 5, 10, and 20°C/min are shown in Figure 16.1. The shrinkage was measured in the z-direction, i.e., the direction parallel to the capillary (i.e. shear) force of the plaster of Paris mold during slip casting, and in the x/y-direction, perpendicular to the capillary force. Anisotropic shrinkage was observed for all heating rates. Samples heated at 5°C/min have a higher shrinkage in the z-direction than in the x/y-direction throughout the entire sintering process, whereas samples heated at 10 and 20°C/min show slightly more shrinkage in the x/y-direction in the initial stage of densification followed by a crossover in the shrinkage and much more shrinkage in the z-direction at higher densities. The anisotropic shrinkage was quantified with a shrinkage anisotropy factor k , which is the ratio of the shrinkage in x/y-direction to the shrinkage in z-direction. Figure 6.2 shows how k changes as a function of relative density and heating rate for the non-aqueous slip cast samples heated at different heating rates during densification. Interestingly, the shrinkage anisotropy factor changes significantly as a function of heating rate during densification and there is much less change in k at the slowest heating rate. Relative density was calculated using the shrinkage anisotropy factor and is plotted as a function of temperature in Figure 6.3. The mean residuals were calculated as a function of Q (Eq. 6.6), and

the minimum is at $Q = 550$ kJ/mol (Figure 6.4). The relatively sharp minimum provides evidence that a single MSC curve is a good fit for the measured TMA data.

When shrinkage in the z-direction is assumed to represent isotropic shrinkage (i.e. $k=1$), then Q increases to 625 kJ/mol. Figure 6.5 compares the MSCs obtained when the shrinkage anisotropy was accounted for (550 kJ/mol) or by assuming isotropic shrinkage (no correction for anisotropy). This example demonstrates the importance of determining whether the sample shrinks anisotropically during the density measurements used to construct the MSC, and the need to correct for anisotropic shrinkage to determine an accurate value Q and MSC. Note that the curves at all three heating rates coincide.

Figure 6.6 shows the corresponding MSC curves of samples formed by various techniques and heated to 1525°C. The measurements were corrected for shrinkage anisotropy as described above. The total shrinkage anisotropy was ~ 0.75 for slip cast and tape cast samples, and ~ 0.92 for dry pressed samples. It is clear that Q changes as a function of forming technique, which is, in part, due to different green densities. The sample prepared by non-aqueous slip casting has a green density of 59% and the lowest Q (550 kJ/mol), followed by the sample prepared by aqueous slip casting with a green density of 58% and a Q of 650 kJ/mol. The samples prepared by dry pressing (no PEG) and tape casting have green densities of 57% and 55%, respectively, and both samples have a Q of 730 kJ/mol. The dry pressed sample with 5 wt.% PEG has a green density of 55% and the highest activation energy with 810 kJ/mol. It can thus be observed that Q decreases as the green density increases and that the shape and position of the MSC changes as a function of forming technique (Figure 6.6). Aminzare et al. [109] also observed that Q is sensitive to the forming technique and concluded that samples prepared by pressure filtration have a lower Q than dry pressed samples as a result of better sample homogeneity as evidenced by the higher green density. As shown in this work, the effect of green density on Q is complicated. For example, the samples prepared by tape casting and dry pressing with 5 wt.% PEG have the same green density of 55%, but different Q values of 730 kJ/mol and 810 kJ/mol, respectively, and different MSC shapes. This suggests that other sample characteristics, in addition to green density, influence Q , such as pore size, pore size distribution, and particle/pore orientation. Given that the curves shown in Figure 6.6 diverge at

very low density it can be assumed that additional factors, i.e. factors that are assumed to be constant in MSC analysis such as D_0 , are highly variable and depend strongly on process history. The magnitude of differences observed suggest that these variables are extremely important in understanding differences in sintering behavior. Such changes are not related to activation energy and have been largely overlooked or ignored in prior literature.

6.3.2 MSC at high densities

The final densities used in the MSC analysis of the samples discussed above are $\leq 90\%$. Above 90% density we observed that the MSC curves for different heating rates diverge and thus dramatically influences the value of Q . Figure 6.7a shows the densification curves of dry pressed samples sintered to $>95\%$ density when heated to 1595°C at different heating rates and held for 5 min. The minimum mean residual analysis yielded $Q = 700 \text{ kJ/mol}$ (Figure 6.7b) and Figure 6.7c shows the resulting MSC. It can be seen that $Q = 700 \text{ kJ/mol}$ gives a good fit at low densities, but the trajectories begin to diverge at densities $>90\%$ (see Fig 6.7c insert).

To account for the effect of bulk density on densification we determined the activation energy at some relative densities by plotting $\ln(-T \cdot d\rho/dt)$ vs. $1/T$ and determining the slopes of the resulting linear curves of the isodensities. Figure 6.8 shows the development of the apparent activation energy obtained from iso-density analysis, Q_{iso} , and it can be seen that Q_{iso} is $\sim 700 \text{ kJ/mol}$ and increases slightly with increasing relative density. At densities $>85\%$ Q_{iso} increases somewhat more rapidly, and at densities $>95\%$ Q_{iso} increases drastically to $>1800 \text{ kJ/mol}$. This change in Q_{iso} explains the divergence of the MSC trajectories obtained from the different heating rates using $Q_{MSC} = 700 \text{ kJ/mol}$.

At densities $<90\%$ the activation energy obtained from the minimum mean residuals Q_{MSC} , which is used to obtain the MSC, is reasonably close to the activation energies obtained from the iso-density analysis, Q_{iso} , resulting in a good fit at all heating rates. However, at densities $>90\%$ where we observe divergence in the MSCs, the values of Q_{iso} are $>100 \text{ kJ/mol}$ greater than the Q_{MSC} value used to construct the MSC. Although the idea of variable activation energy is understandable, it is not physically realistic to consider that the activation energy for sintering is intrinsically a function of ρ . It is more likely that this increase in

Q_{iso} and the divergence of the MSC at high densities is caused by microstructural or mechanistic changes that are not accounted for in the MSC model.

6.3.3 Quantification of the MSC shape

A way to account for microstructural changes is analyzing the shape of the MSC, since it is determined by the evolution of the microstructural parameters in the left hand side of Eq. 5. Microstructural evolution can be described quantitatively by:

$$C = \frac{k_B G^n}{3\gamma\Omega\Gamma D_0} \quad (6.7)$$

By rearranging Eq. 6.4, C can be determined as a function of relative density:

$$C = \rho \frac{d\Theta}{d\rho} \quad (6.8)$$

In Figure 6.9 it can be seen that C increases by more than 5 orders of magnitude between 57% and 98% relative density. The increase in C is partially due to the 8-fold increase in grain size from 0.3 to 2.4 μm during sintering of the sample to 98% relative density. Assuming that grain boundary diffusion controls densification ($n=4$), the coarsening of the microstructures accounts for an increase in C of ~ 3.5 orders of magnitude. The remaining ~ 2 orders of magnitude increase in C are most likely due to an increase in the geometric factor Γ , since it is a function of relative density and the only parameter that is expected to change considerably with temperature. Note that the obtained trajectories for C also diverge above 90% relative density, similar to the MSCs.

While we can hypothesize about the factors that influence the MSC shape, the actual shape of the MSC cannot be understood based on the existing MSC analysis methodology, because one or more parameters in Eq. 6.7 vary with time and temperature in a complex manner. To gain insight into the development of the shape of the MSC the individual parameters in Eq. 6.7 need to be investigated. For example, grain size evolution could be tracked as a function of density and extracted from the C parameter. Assuming that the divergence of the MSCs at densities $>90\%$ is caused by differences in grain size as a result of different heating rates only, this divergence in MSC shape at densities $>90\%$ could be corrected. If the development of the geometry factor Γ could be quantified and separated from

the C parameter, we should be able to assign a constant value for C , and the Q value that results from MSC analysis should represent the true activation energy for sintering. However, such an analysis would assume that Γ can be quantified on a sufficiently accurate level, and that grain size and Γ are the only factors in Eq. 6.7 that change as a function of relative density.

6.3.4 Influence of powder chemistry

Figure 6.10 shows the MSCs of Na_2O -doped samples formed by non-aqueous slip casting. It can be seen that Q changes as a function of Na_2O concentration and increases from 550 kJ/mol for samples with no Na_2O dopant to 700 and 730 kJ/mol for samples doped with 250 and 500 ppm Na_2O , respectively. Q decreases to 690 kJ/mol when the concentration is further increased to 1000 ppm Na_2O . The position of the MSC changes as a function of Na_2O concentration as well and the effect of Na_2O concentration on the MSC is complicated.

6.3.5 Limitations of the MSC analysis

Anisotropic shrinkage is commonly observed in slip cast parts since the capillary force cause particles in the slurry to align during slip casting. It should be noted that the degree of shrinkage anisotropy strongly depends on the particle morphology and forming technique (i.e. magnitude of shear force exerted on the particles and ease of reorientation). For samples that were prepared by colloidal forming techniques, such as slip casting and tape casting, the degree anisotropic shrinkage has to be taken into account during the MSC analysis, otherwise the densities calculated from the dilatometry data alone are inaccurate and thus the calculated value of Q and the shape of the MSC are incorrect. Likewise, samples formed by uniaxial pressing are often anisotropic but not to the same degree as slurry processed ceramics.

The above results show that a variety of factors such as forming technique and powder chemistry affect the value of Q and the shape of the MSC in a complicated way, and the reason for this complicated relation lies in the assumption in MSC analysis that sintering is influenced by only one single mechanism. Making this assumption allows MSC analysis to assign an activation energy for sintering that corresponds to this specific sintering mechanism. If this assumption held true, variations in forming technique or chemistry could be analyzed using the MSC

approach and using Q as an indicator for how the sinterability of a powder changes as a function of powder chemistry and forming technique. However, sintering is typically divided into different stages, all of which are governed by different sintering mechanisms. When multiple mechanisms are involved, each mechanism can be affected differently by such changes and Q loses its physical meaning as an activation energy for a specific sintering mechanism. As a result, Q appears to be a function of relative density (Figure 6.8) and the changes in Q and MSC shape as a function of powder chemistry and forming technique are complicated (Figures 6.9 and 6.10).

For example, we know that initial pore size, pore size distribution, and pore/particle orientation in a green body are highly dependent on the forming technique. Changes in these parameters affect different sintering stages in different ways. During initial stage sintering the sinter undergoes a particle rearrangement process that is driven by capillary forces and therefore highly sensitive to the aforementioned parameters. During final stage sintering the concentration of large pores that can only slowly be eliminated is determined by the forming technique. Mechanistic changes as such can affect Q in different ways.

Similarly, powder chemistry affects initial stage sintering and intermediate stage sintering in different ways. In previous chapters, it was observed that the onset temperature of sintering increases with higher Na_2O concentration, which has the effect of increasing Q . The further development of densification was shown to depend heavily on additional factors. For example, samples with $\text{Na}_2\text{O}/\text{SiO}_2$ ratios ~ 1.0 densify faster during intermediate stage sintering than samples with $\text{Na}_2\text{O}/\text{SiO}_2$ ratios ~ 0.1 for the same SiO_2 concentration because Na_2O decreases the viscosity of the siliceous liquid grain boundary phase, and, therefore, enhances diffusion, which would decrease Q . This demonstrates that powder chemistry influences fundamental sintering mechanisms at different sintering stages and in different ways.

Since the processes and mechanisms of all sintering stages are lumped into one Q value during MSC analysis, forming technique and powder chemistry may affect the value of Q and the shape of the MSC, but the changes in sintering behavior and mechanisms cannot be sufficiently described using Q and the MSC. Therefore, the MSC approach is judged to be insufficient to evaluate forming and powder chemistry effects on sintering. It is recommended that Q values obtained by MSC

analysis for different powder grades (i.e. chemistries, forming techniques, particle size, etc.) should not be compared or used to draw conclusions about sintering mechanisms.

6.3.6 Practical use of the MSC analysis

Even though MSC analysis is insufficient to analyze fundamental differences in sintering behavior due to differences in powder chemistry and forming technique, choosing an appropriate Q value converges the trajectories of samples obtained from different heating rates onto one MSC, and this Q value and the obtained MSC can be used to predict densification. As explained in the literature [113, 114], the Q value obtained is an apparent activation energy for the entire sintering process of a sinter and accounts for densification (regardless of mechanism), the retardation of densification due to grain growth, surface diffusion in the early sintering stages, and other processes that potentially influence densification. Consequently, Q is a fitting parameter that is composed of a variety of factors that influence densification, including the activation energies for sintering of all involved mechanisms.

One of the practical objectives of MSC analysis is to predict the sintered density of samples prepared from a given powder for an arbitrary time/temperature condition. The MSC data provided above and Eq. 6.5 can be used to construct equivalent time/temperature diagrams to predict the density of samples for known heating conditions [109]. Fig. 6.11 is an example of the equivalent time/temperature conditions leading to equivalent densities for non-aqueous processed powder dry pressed samples heated at 10°C/min. The contours shown in Figure 6.11 indicate the equivalent relationships between particular time/temperature treatments and relative densities of 80, 85, 90, and 95%. For example, a relative density of 85% is reached after heating a dry pressed sample at 10°C/min to 1460°C with no hold time. The same density is reached after heating a dry pressed sample from the same powder at 10°C/min to 1400°C and holding for 29 min. It should be noted that the predicted MSC response for >90% sintered density has some inaccuracy due to the discrepancies we noted above for MSC data analysis at >90% density. Despite earlier reservations and limitations, the predictions for equivalent time/temperature conditions leading to 95% density are insightful and, at least, give a semiquantitative measure of the effect of time and temperature on sintering. In the literature it was

proposed to divide the MSC into two regimes of "low density" and "high density" (i.e., <75% and >85%), respectively with two individual Q values to account for the changes in Q during densification [108, 115]. While the fundamental reasoning behind assigning two separate Q values is questionable, considering our conclusion that Q is a fitting parameter without physical meaning, this could be an useful approach to obtain more accurate density predictions at high densities.

6.4 Summary

MSC analysis results in two pieces of information; a Q value and the MSC curve itself. Q should not be interpreted as the activation energy for sintering, since multiple mechanisms contribute to its value and processing history and powder chemistry can drastically affect the Q value and the shape of the MSC. Therefore, comparing Q between different chemistries is not an appropriate means to interpret fundamental, mechanistic changes in sintering behavior.

It is evident that the MSC is only useful for characterizing the sintering behavior of the specific ceramic powder studied. A number of factors need to be accounted for to obtain accurate Q values and MSCs including sample shrinkage anisotropy, and limiting the density range to < 90% density to avoid microstructural changes that are not accounted for in the MSC analysis. With more accurate Q values the MSC approach is a useful tool and "a practical approach to sintering" as originally proposed by Su and Johnson, but is not sufficient to explain fundamental changes in sintering behavior, or to determine the "activation energy" for sintering since basic assumptions made for MSC analysis are insufficient to describe the entire sintering process.

Table 6.1. Q values obtained by MSC analysis for different alumina powders.

Alumina grade	Forming technique	Heat rates (°C/min)	Q (kJ/mol)	Ref.
AKP-50 Sumitomo Chemicals	CIP (270 MPa)	60 to 750°C, 8-45 to 1500°C	440	[101]
AKP-50 Sumitomo Chemicals	Uniaxial pressing (50 MPa) CIP (200 MPa)	3-20 to 1400°C	555	[107]
AKP-50 + 2000 ppm MgO Sumitomo Chemicals	Uniaxial pressing (50 MPa) CIP (200 MPa)	3-20 to 1400°C	880	[107]
Taimicron TM-DAR Taimei Chemicals	CIP (300 MPa)	2-20 to 1500°C	770	[108]
RC-HP DBM Reynolds Chemicals	CIP (300 MPa)	2-20 to 1500°C	640	[108]
Taimicron TM-DAR Taimei Chemicals	Uniaxial pressing (50 MPa) CIP (200 MPa)	2-25 to 1400°C	700	[109]
Taimicron TM-DAR Taimei Chemicals	Pressure filtration (40 MPa)	2-25 to 1400°C	605	[109]
Taimicron TM-DAR Taimei Chemicals	SPS (50 MPa)	35-150 to 1200°C	290	[110]
99.9%, Dalian Luming Nanometer Materials	Uniaxial pressing (80 MPa) CIP (250 MPa)	0.5-5 to 1640°C	1064	[111]

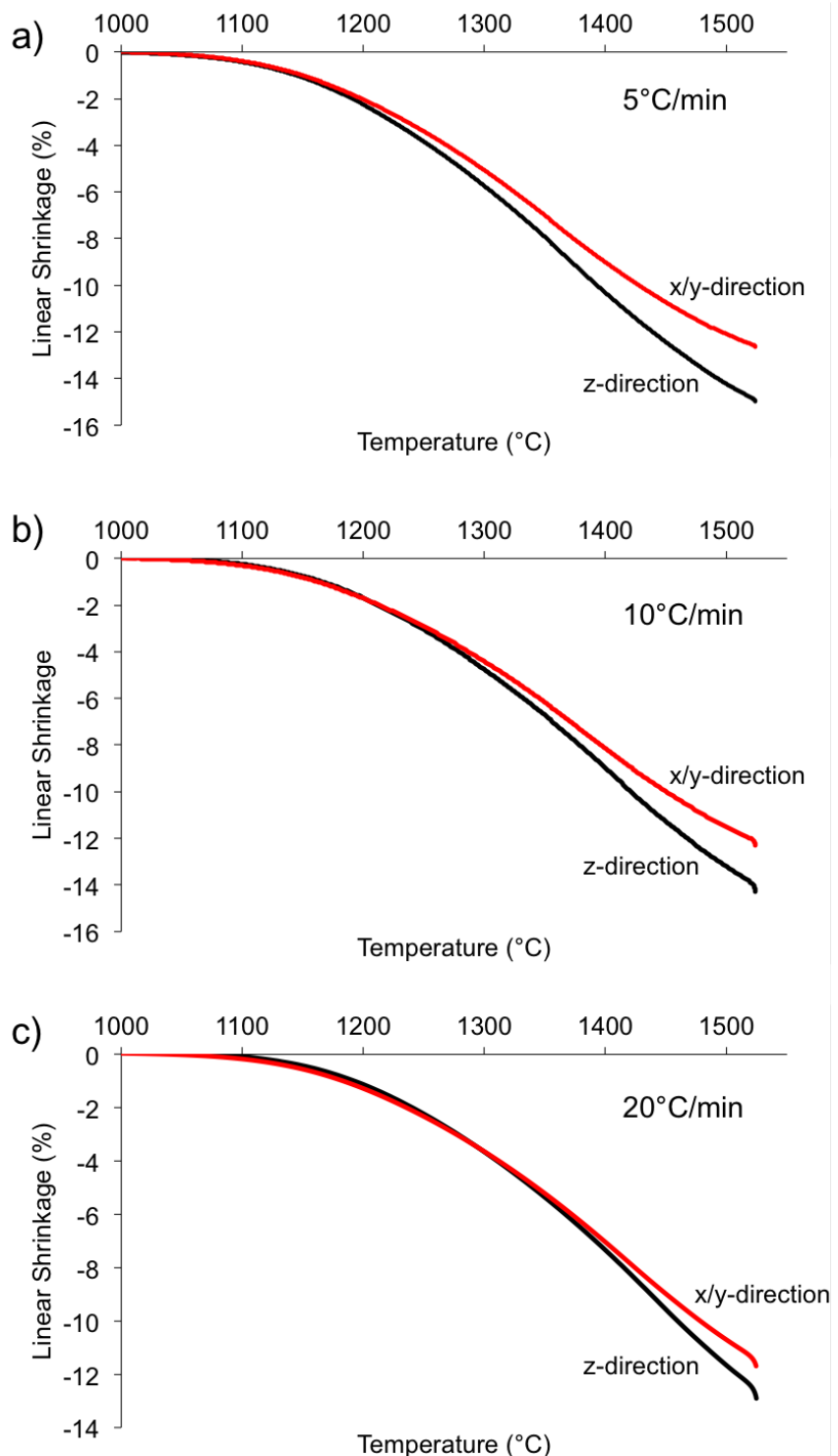


Figure 6.1. Dilatometry curves of non-aqueous slip cast CT3000 LS SG samples heated at a) 5°C/min, b) 10°C/min, and c) 20°C/min to 1525°C measured parallel to (z-direction) and perpendicular to (x/y-direction) the capillary force acting during slip casting.

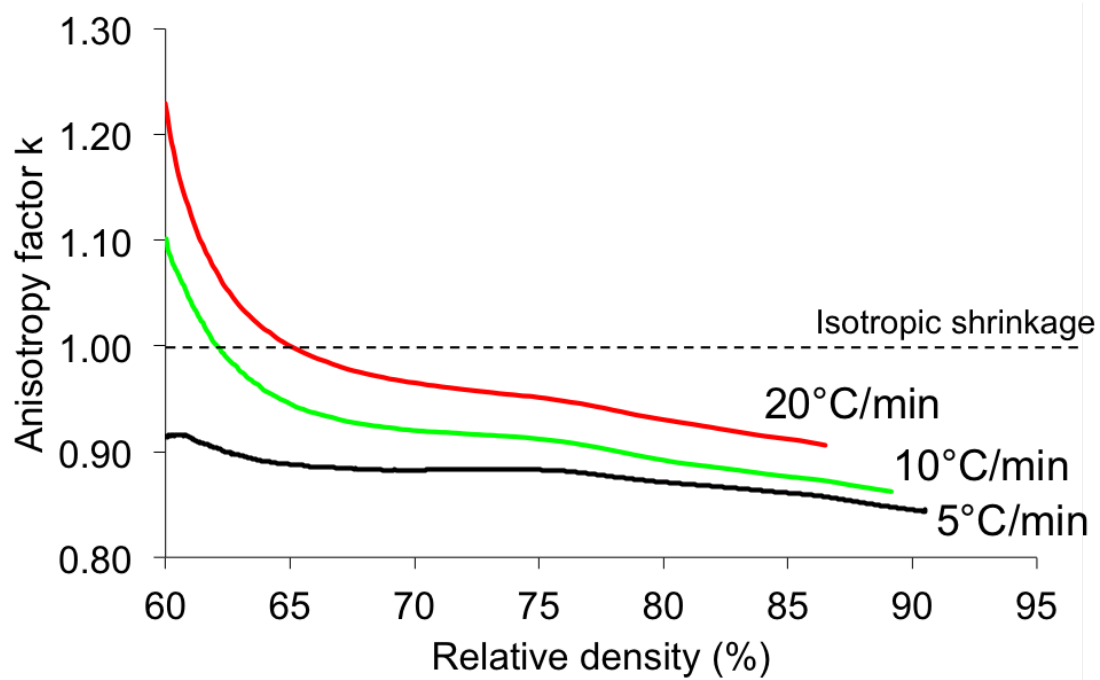


Figure 6.2. Development of the shrinkage anisotropy factor for shrinkage, k , during densification of non-aqueous slip cast samples as a function of relative density for CT3000 LS SG samples heated at different rates.

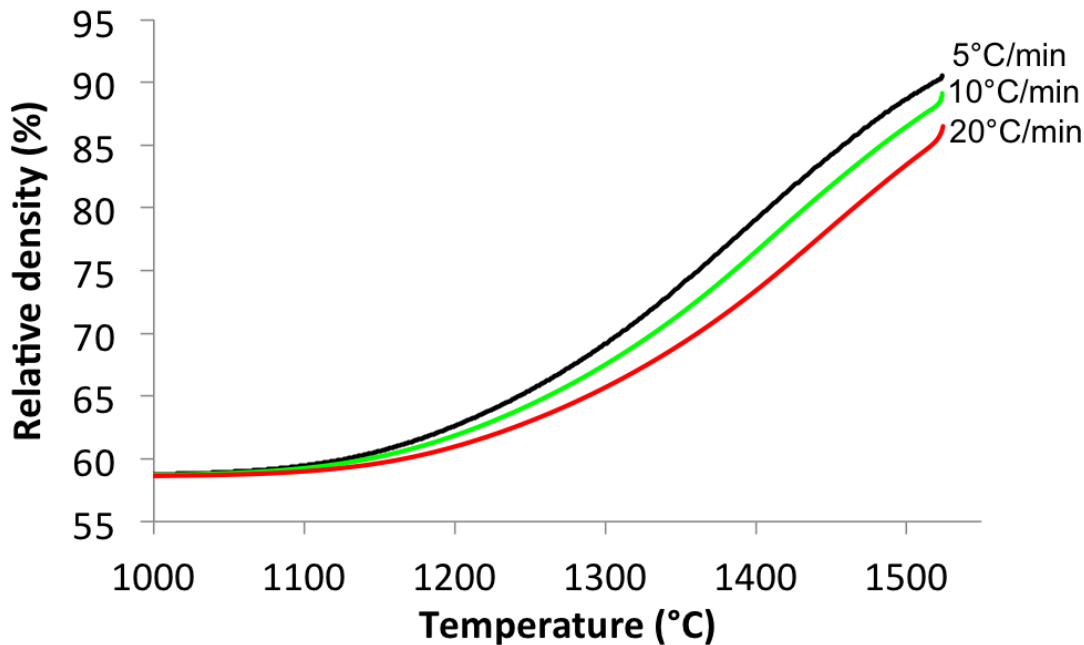


Figure 6.3. Development of the relative density corrected for shrinkage anisotropy as a function of temperature for non-aqueous slip cast CT3000 LS SG samples heated at different rates.

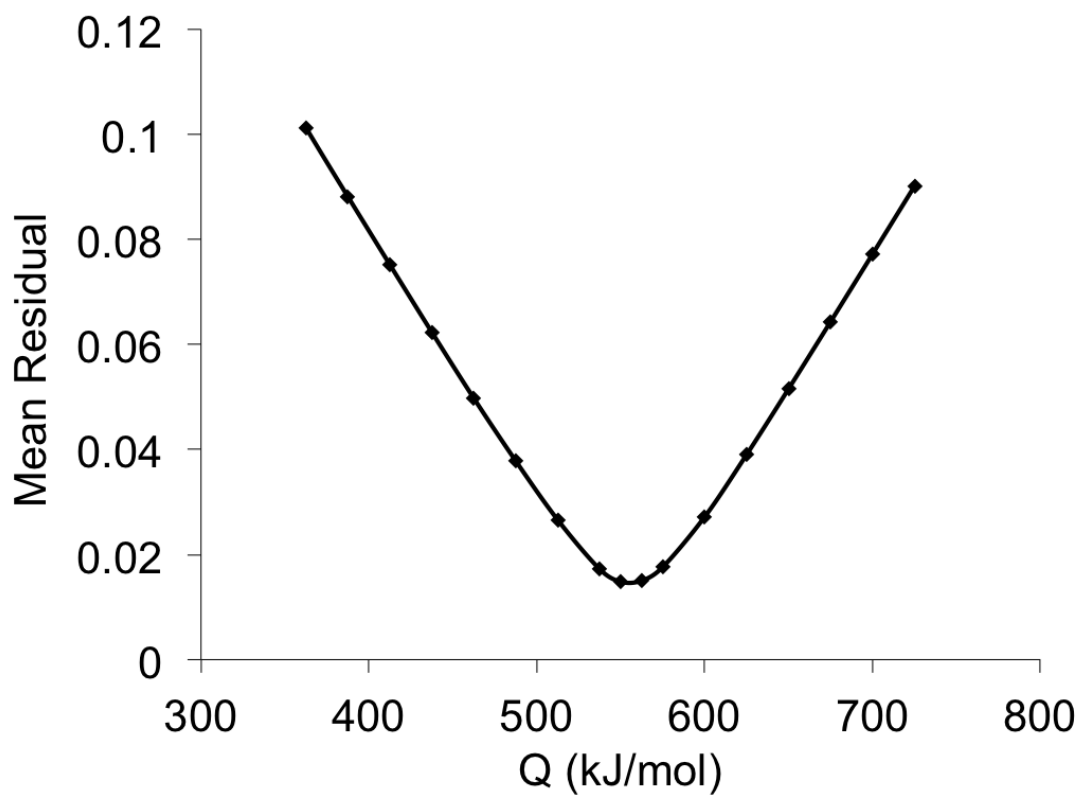


Figure 6.4. Mean residuals of the MSCs assuming different values for Q for non-aqueous slip cast CT3000 LS SG samples.

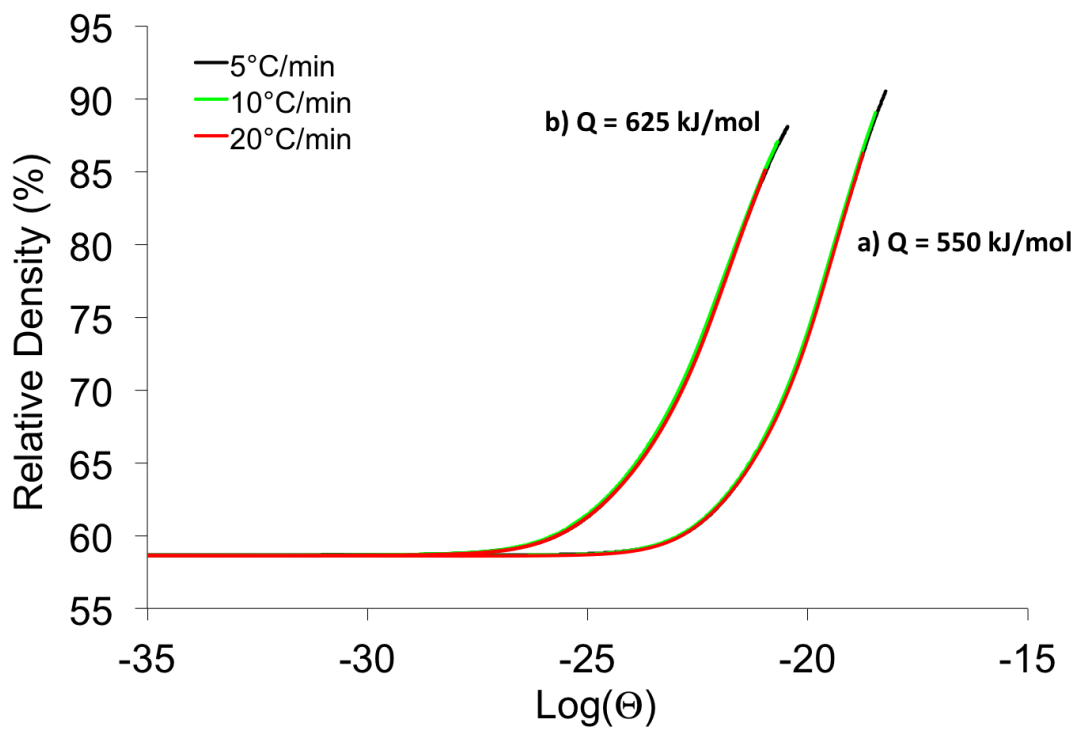


Figure 6.5. MSCs of CT3000 LS SG samples prepared by non-aqueous slip casting using a) the Q -value obtained by accounting for shrinkage anisotropy ($Q=550 \text{ kJ/mol}$) and b) using Q -value when shrinkage anisotropy was uncorrected for ($Q = 625 \text{ kJ/mol}$).

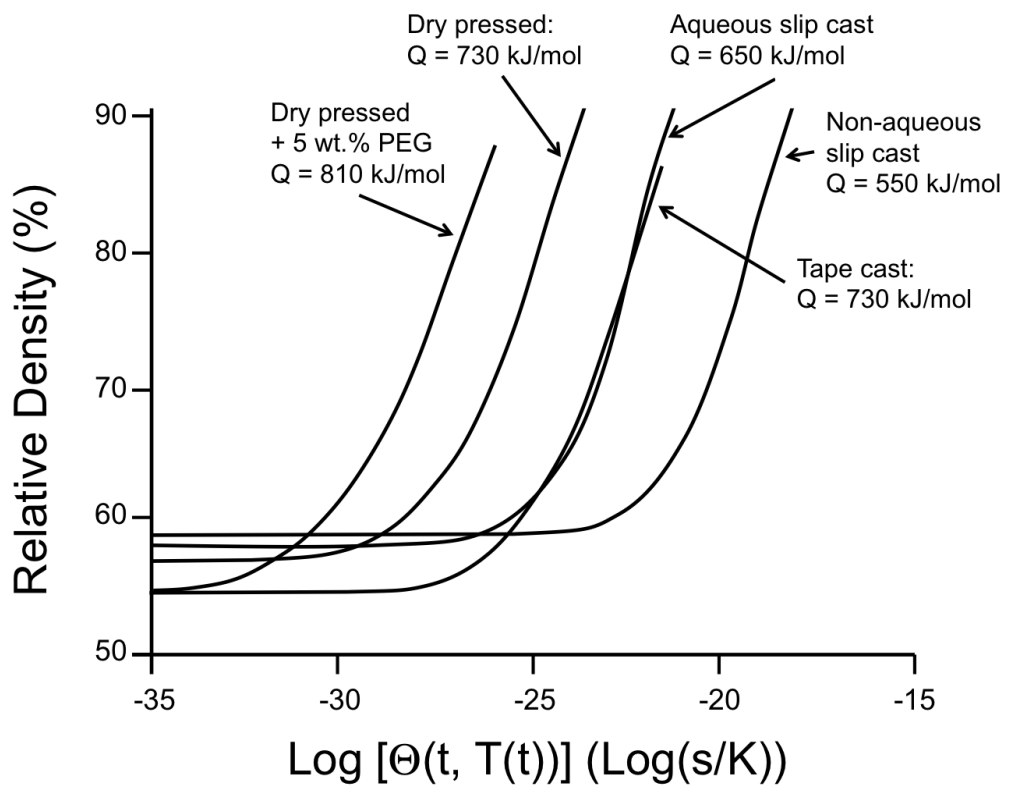


Figure 6.6. MSCs and Q -values of CT3000LS-SG samples obtained from the minimum mean residuals for samples prepared by different forming techniques and accounting for shrinkage anisotropy.

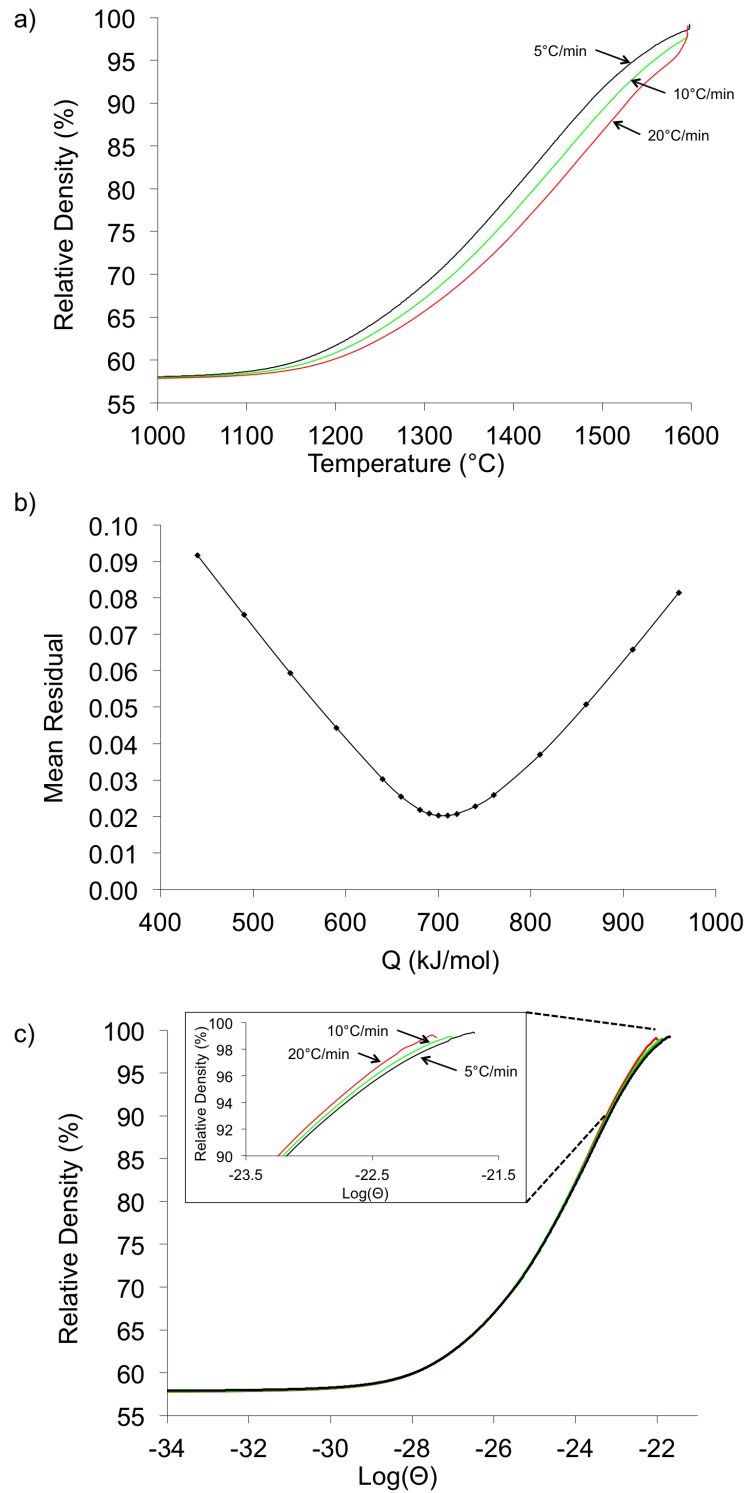


Figure 6.7. a) Densification of dry pressed CT3000 LS SG samples at different heating rates, b) mean residuals as a function of Q , and c) MSC for $Q = 700$ kJ/mol obtained from the minimum mean residuals, showing divergence at densities $>90\%$.

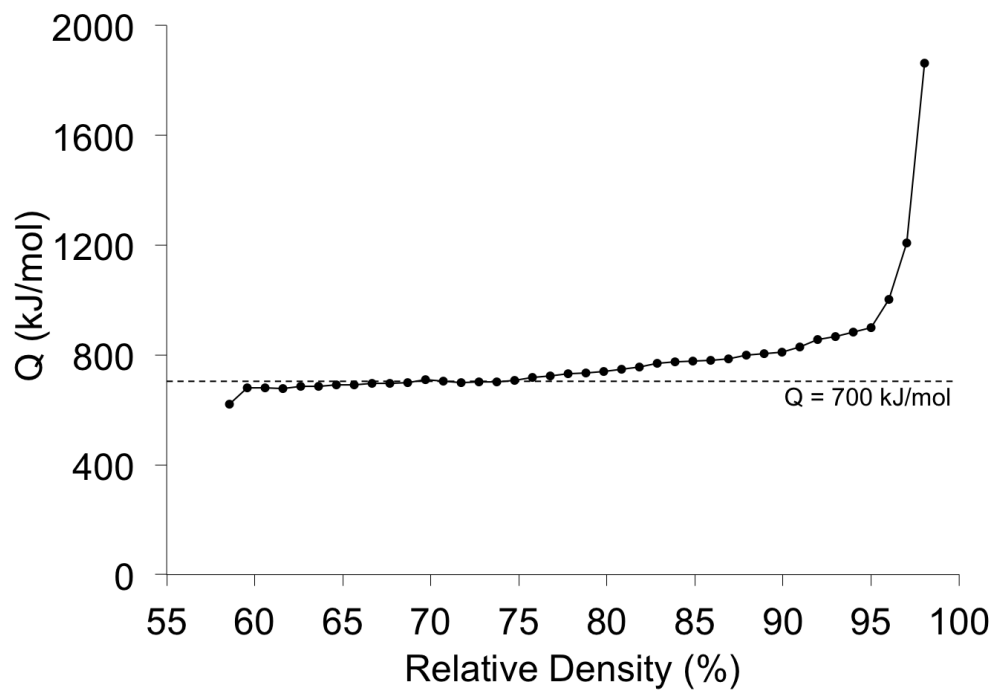


Figure 6.8. Q -values for dry pressed CT3000 LS SG samples as a function of relative density obtained from iso-density analysis.

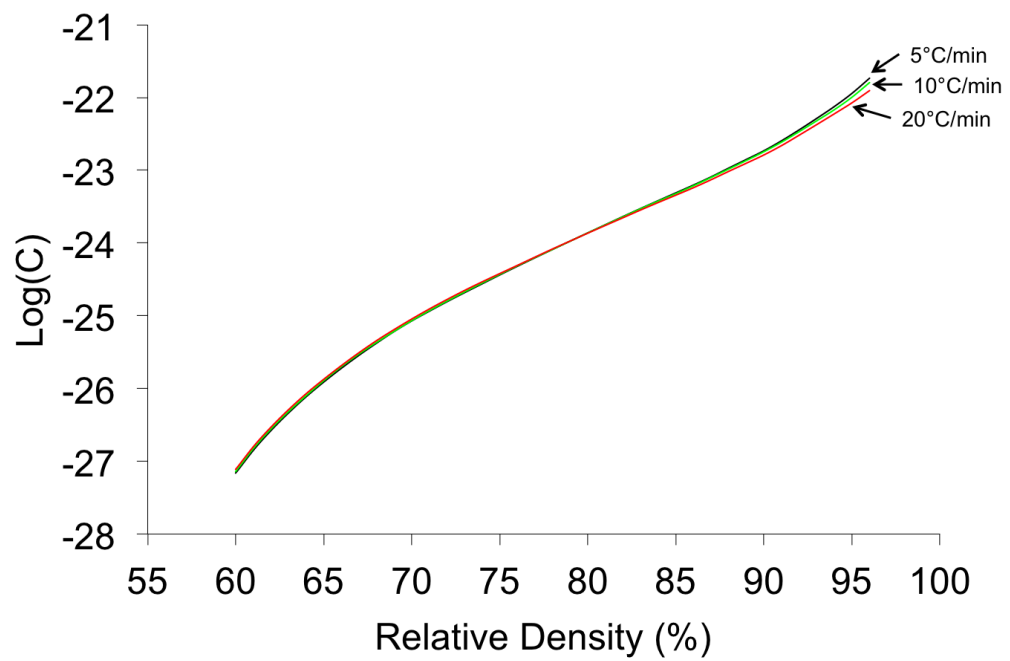


Figure 6.9. Development of the microstructural parameters, summarized in the C parameter, as a function of relative density for dry pressed CT3000 LS SG samples.

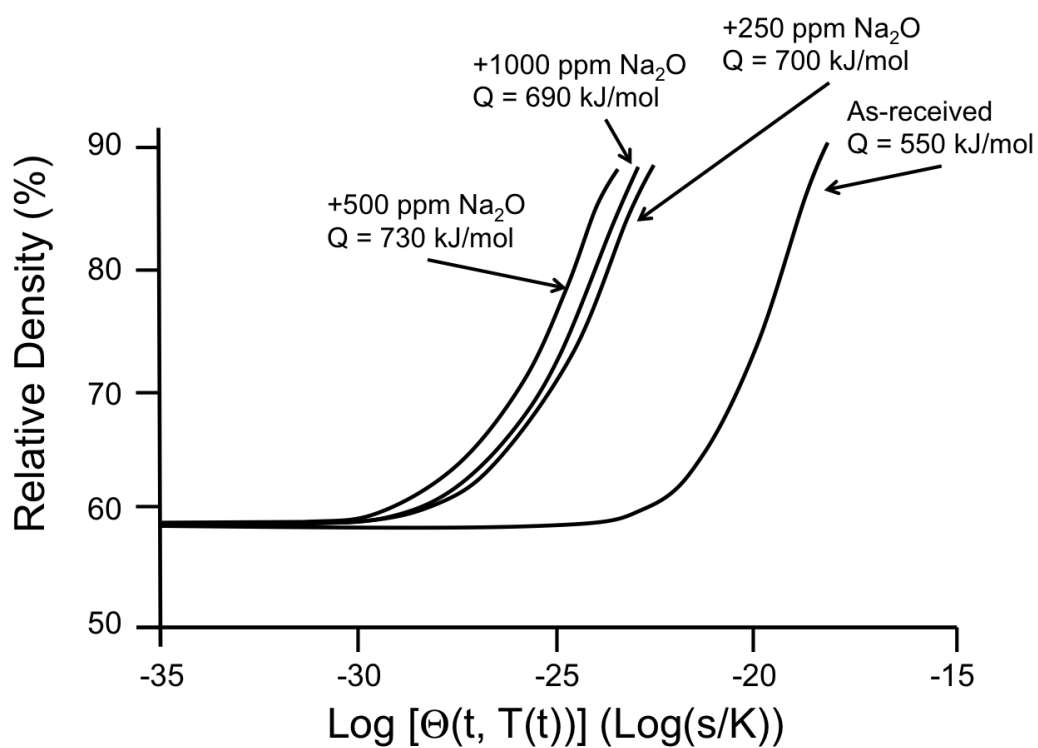


Figure 6.10. MSCs and Q -values for CT3000 LS SG samples prepared by non-aqueous slip casting with different Na_2O concentrations.

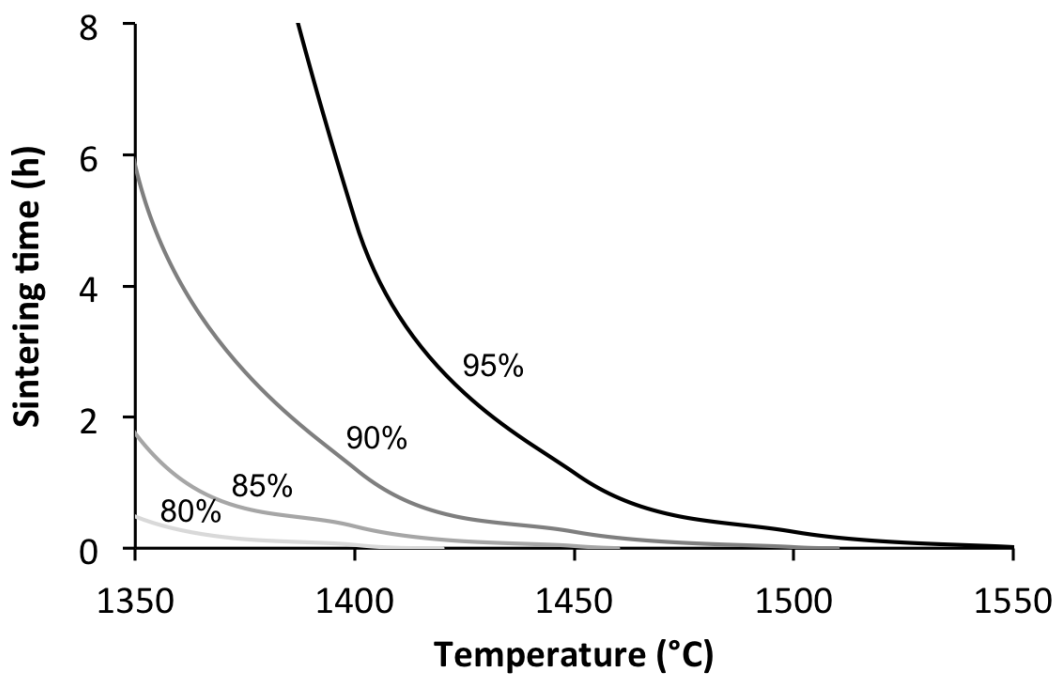


Figure 6.11. Equivalent time/temperature diagram for CT3000 LS SG samples prepared by non-aqueous slip casting heated at 10°C/min. The contours may be used to predict heat treatments requirements to achieve a desired density.

Chapter 7 |

Summary and Future Work

7.1 Summary

The goal of this work was to gain fundamental understanding on how powder chemistry of commercial Bayer alumina affects densification, microstructural evolution, and sintering mechanisms. A large number of investigations has dealt with the effect of impurities and dopants on the sintering of ultrahigh purity alumina. However, there is little research about the effects of impurities that are characteristic of Bayer alumina, such as Na₂O, specifically in the presence of other impurities and dopants that are known to affect sintering of alumina, such as SiO₂ and MgO. This work systematically investigated cross effects of some impurities and dopants that are characteristic to commercial grade Bayer alumina on densification, microstructural evolution, and fundamental sintering mechanisms.

7.1.1 The Effects of Na₂O and SiO₂ on Liquid Phase Sintering of Bayer Al₂O₃

To investigate the effect of Na₂O and SiO₂ on sintering of MgO-free Bayer alumina samples with up to 1029 and 603 ppm, respectively, were prepared. Dilatometry and sintering kinetics experiments showed that increasing Na₂O concentrations led to an increased onset temperature of sintering and results in a lower density up to final stage sintering, but no difference in relative density for sintering times of 3 h or longer at 1525°C was observed. Increasing SiO₂ concentrations leads to a significant retardation of densification starting at ~1250°C and after 8 h at 1525°C samples with 603 ppm SiO₂ have 4% lower density than samples with 103 ppm

SiO_2 . In samples with increased SiO_2 concentrations, such as 603 ppm, the addition of Na_2O increases the density by 1 - 2.5% compared to samples with low Na_2O concentrations.

The observed sintering behavior was explained by a liquid phase sintering model, where the viscosity of the liquid grain boundary phase, and therefore the diffusion coefficient, are determined by the chemical composition of the liquid grain boundary phase. The viscosity of the grain boundary phase is 2 orders of magnitude lower for samples with high $\text{Na}_2\text{O}/\text{SiO}_2$ ratios, e.g. 0.9 for samples with 529/603 ppm $\text{Na}_2\text{O}/\text{SiO}_2$, than the viscosity of the liquid grain boundary phase of samples with low $\text{Na}_2\text{O}/\text{SiO}_2$ ratios, e.g. 0.1 for samples with 29/603 ppm $\text{Na}_2\text{O}/\text{SiO}_2$. Additionally, the solubility of Al_2O_3 in the liquid grain boundary phase is increased for samples with higher Na_2O concentrations. Both of these factors lead to enhanced densification in samples with higher $\text{Na}_2\text{O}/\text{SiO}_2$ ratios. It is concluded that Bayer Al_2O_3 densification is controlled by the Na_2O to SiO_2 ratio.

7.1.2 Powder Chemistry Effects on the Sintering of MgO-doped Specialty Al_2O_3

MgO is typically added to commercial alumina powder due to its beneficial effect on sintering. To identify the mechanisms responsible for this beneficial effect, 380 ppm MgO-doped Bayer alumina powder with chemical and physical characteristics similar to the MgO-free powder studied in the first part of this dissertation was used and doped to similar chemistries as the MgO-free Bayer alumina. Dilatometry measurements and sintering kinetics of the MgO-free powder and the MgO-doped powder were compared to identify differences in sintering behavior as a result of MgO-doping. In both powders higher SiO_2 concentrations retard densification significantly, however, this effect is less severe in the MgO-doped powder than in the MgO-free powder. For example the addition of 500 ppm SiO_2 results in 4% lower relative density in MgO-free powder samples after sintering at 1525°C for 8 h, but only 2% lower relative density in MgO-doped powder samples. While the $\text{Na}_2\text{O}/\text{SiO}_2$ ratio has a similar effect in both powders during initial and intermediate stage sintering, i.e. higher $\text{Na}_2\text{O}/\text{SiO}_2$ ratios increase densification, no effect of the $\text{Na}_2\text{O}/\text{SiO}_2$ ratio was observed for 380 ppm MgO-doped Bayer alumina samples

during final stage sintering at densities $\geq 92\%$.

High resolution TEM showed the presence of a liquid phase in the grain boundaries of MgO-free powder samples and in MgO-doped powder samples during intermediate stage sintering ($< 92\%$). During final stage ($> 92\%$) sintering the thickness of the grain boundary phase in the MgO-doped powder samples is significantly reduced compared to MgO-free powder. EDS analysis showed that MgO and SiO₂ have an increased co-solubility in the alumina lattice where Mg²⁺ and Si⁴⁺ compensate for each size and charge difference relative to Al³⁺ in the alumina lattice. The thermodynamic stability of such a mechanism was shown by DFT-based first-principles calculations. The reduced amount of SiO₂ on the grain boundaries of MgO-doped alumina leads to enhanced densification compared to MgO-free alumina because SiO₂ has been shown to retard densification.

7.1.3 Dynamic development of nanometer scale grain boundaries during liquid phase sintering

It was shown that grain boundary chemistry and structure drastically affect fundamental sintering mechanisms and, therefore, it is crucial to understand how grain boundaries change during densification. A physical model was developed to describe the dynamic development of grain boundaries in Bayer alumina during densification. The liquid glass phase concentration that forms during sintering is a function of powder chemistry and the glass phase concentration changes during densification because the temperature of the sample changes during heating. The liquid glass phase initially accumulates in the particle contacts due to capillarity, and then the distribution of the glass phase changes during sintering due to the formation of grain boundaries and grain growth, which leads to the observed dynamic change in grain boundary thickness. The model predicts that the grain boundary thickness can be governed by either the glass phase concentration or by an equilibrium grain boundary thickness. If sufficient glass phase is present to form an intergranular film of equilibrium thickness, then the balance between attractive and repulsive colloidal forces determines the grain boundary thickness, and for grain boundary films > 1 nm the main contributions to this force balance are attractive capillary forces and repulsive structural disjoining forces.

Changes in Na₂O/SiO₂ ratio and/or the addition of MgO changes the concentra-

tion of liquid phase in the sample and the interparticle force balance, and, therefore, changes the grain boundary thickness. It was shown that grain boundary thicknesses measured by high resolution TEM agree well with predicted film thicknesses as a function of powder chemistry.

7.1.4 Second phase formation in Bayer alumina

Bayer alumina has higher impurity concentrations than ultrahigh purity aluminas, which makes these powders more prone to second phase formation, and thus the conditions of formation and the formation process of second phases in Bayer alumina were explored as a function of powder chemistry. XRD showed that β -Al₂O₃ was the only second phase that forms for the range of chemistries explored in this dissertation. No β -Al₂O₃ was observed in samples with low Na₂O and MgO concentrations such as 29 and 2 ppm, respectively. Only a small number of β -Al₂O₃ grains form when the Na₂O concentration is \leq 529 ppm. However, there was a significant increase in the amount of β -Al₂O₃ observed when the Na₂O concentration was increased to 1029 ppm. Increasing the MgO concentration in samples with 29 ppm Na₂O increases the number of β -Al₂O₃ grains up to 502 ppm, but no further increase in number density of β -Al₂O₃ grains is observed when the MgO concentration is increased to 1002 ppm. In general, increasing Na₂O and MgO concentrations leads to an increase in number density and a decrease in β -Al₂O₃ grain size, but increasing the SiO₂ concentration results in a decrease in number density and increase in β -Al₂O₃ grain size.

It was shown that SiO₂ and Na₂O form a liquid grain boundary phase during sintering of alumina, and the amount of β -Al₂O₃ that forms is determined by the Na₂O-supersaturation of the liquid grain boundary phase, i.e. the Na₂O/SiO₂ ratio in the sample. Formation kinetics showed that the majority of beta alumina form within the first hour at 1525°C, which is within the same time as when the grain boundary thickness decreases due to the proposed MgO- and SiO₂ co-dissolution mechanism into the alumina grain. It was concluded that MgO increases the amount of β -Al₂O₃ because the co-dissolution of MgO and SiO₂ into the alumina grain lowers the SiO₂ concentration in the glassy grain boundaries during final stage sintering. As a result, the Na₂O/SiO₂ ratio in the grain boundaries increases, which leads to a higher Na₂O-supersaturation and to an enhanced formation of

β -Al₂O₃.

7.1.5 A Critique of Master Sintering Curve Analysis of Sintering Processes

The objective of this work was to explore if the Master Sintering Curve (MSC) approach can be used as a tool to identify powder chemistry effects on the sintering of Bayer alumina in a fundamental, predictive way. MSC analysis results in an apparent activation energy Q and the MSC itself. It was shown that processing history and powder chemistry drastically affect the value of Q and the shape of the MSC but no direct correlation was found between powder chemistry and the MSC shape or Q since changes in powder chemistry can cause complex variations in sintering mechanisms. Likewise, no direct correlation was found between forming technique, the resulting green density, and Q or the shape of the MSC because factors such as pore size and pore size distribution, which are known to influence densification, are not accounted for in MSC analysis. Finally, the applicability of MSC at high densities (>90%) is limited by changes in microstructural evolution that occur as a function of densification rate, but are not accounted for in MSC analysis.

It was shown that MSC analysis can be a useful tool for predicting the sintering behavior of a specific powder after its Q and MSC are accurately determined. For example, shrinkage anisotropy has to be accounted for to determine accurate Q values and MSCs. Under these conditions MSC analysis is only a useful and practical tool to predict sintering behavior, but again fails to analyze fundamental sintering processes or changes that result from differences in chemical or physical variations of the sintering material.

7.2 Future work

This work focused on the effects and cross effects of Na₂O, SiO₂, and MgO on the sintering of commercial Bayer alumina and is therefore a step towards a fundamental understanding of the interplay of multiple dopants and impurities during sintering of commercial Bayer alumina. Several paths for future research are proposed below.

The effects of additional impurities that can be found in commercial powders,

specifically CaO, should be investigated. Multiple studies have investigated the effect of CaO on the sintering of ultra-high purity alumina, however, it is crucial to consider the presence of other impurities and dopants. The importance of considering the presence of other impurities and dopants was shown in this work; for example, the effect of Na₂O on the sintering of Bayer alumina strongly depends on the SiO₂ concentration and the Na₂O/SiO₂ ratio, and the effect of MgO depends on the SiO₂ concentration. Similar relations could exist between CaO and other impurities and dopants, and it is of great interest to identify such effects. Based on the present investigation and literature reports a variety of hypotheses of the effect of CaO on the sintering of Bayer alumina are reasonable. Initial and intermediate stage sintering in Bayer alumina are governed by a liquid phase sintering mechanism, due to the presence of SiO₂, which forms a siliceous glass phase in the grain boundaries. At these sintering stages Na₂O and MgO were shown to affect the properties of the liquid grain boundary phase by acting as a network modifier. It is likely that CaO behaves in a similar manner. However, calcium silicate glass melts are known to exhibit liquid-liquid miscibility gaps that are influenced by the MgO, Na₂O, and Al₂O₃ concentrations [116]. This suggests that glass phases of different compositions can be present at the same time, which could significantly affect sintering, since diffusion is controlled by viscosity and, therefore, the composition of the liquid phase. Furthermore, different concentrations in CaO can affect second phase formation. For example, CaO by itself forms calcium hexaluminate (CaO·6Al₂O₃) in alumina, which can form a solid solution with β -Al₂O₃ in the high alumina region of the Na₂O-SiO₂-CaO-Al₂O₃ system [49]. Different ratios and concentrations of impurities and dopants might lead to different amounts and types of second phases, and, therefore, the influence of CaO on the formation of second phases should be investigated.

Grain boundaries of ceramics have been extensively researched over the past decades because their structure and chemistry determine sintering mechanisms and many properties of ceramics, such as corrosion, mechanical, and electrical properties. In this work the chemical composition and structure of grain boundaries was investigated to gain insight into sintering mechanisms and to explain the observed sintering behavior. Therefore, samples were quenched from the sintering temperature to room temperature to "freeze" the chemistry and structure at the sintering temperature. However, ceramic parts for most applications are cooled at

much slower rates, which can drastically affect grain boundary structure, thickness, and chemistry, and the grain boundaries investigated in this work may not be representative for grain boundaries in slow cooled Bayer alumina ceramic parts. The influence of cooling rate on the chemistry and structure of grain boundaries of Bayer alumina should be investigated to gain insight into how properties are affected by different powder chemistries and grain boundary characteristics. The development of time-temperature-transformation (TTT) diagrams for grain boundaries [117] as a function of powder chemistry could be a powerful tool to design grain boundaries and tailor the properties of alumina ceramics.

In this dissertation a physical model was developed to predict the dynamic development of grain boundaries during densification. A potential application for such predictions is to determine the applicability of different sintering models, i.e. solid-state sintering or liquid phase sintering. For samples with high SiO₂ concentrations, such as 603 ppm, it was demonstrated that sintering at 1525°C can be analyzed using a liquid phase sintering model, and for samples with low SiO₂ concentrations, such as 103 ppm, the grain boundary structure and chemistry at 1525°C suggests that a solid state sintering model is more appropriate to analyze sintering. However, it was also demonstrated that the structure and chemistry of the grain boundaries are a function of additional parameters, such as temperature, relative density, powder chemistry, and grain size. For example, the grain boundary thickness first decreases and then increases as a function of relative density, which implies that for certain glass phase concentrations there can be a transition from liquid phase sintering to solid state sintering and vice versa. Another example is the effect of MgO on final stage sintering of Bayer alumina. It was shown that during initial and intermediate stages alumina with 582 ppm SiO₂ densifies by a liquid phase sintering mechanism. However, if MgO is present then MgO and SiO₂ form a solid solution in the alumina grains during final stage sintering, which reduces the amount of SiO₂ in the grain boundaries, and, depending on the MgO concentration, sintering should be analyzed using a solid state sintering model. This described mechanism suggests that transitions from liquid phase sintering to solid state sintering and vice versa are possible during densification. It would be interesting to investigate in greater detail the effects of such transitions on the sintering process.

Bibliography

- [1] ZUO, F., C. CARRY, S. SAUNIER, S. MARINEL, and D. GOEURIOT (2013) “Comparison of the microwave and conventional sintering of alumina: effect of MgO doping and particle size,” *Journal of the American Ceramic Society*, **96**(6), pp. 1732–1737.
- [2] GAVRILOV, K. L., S. J. BENNISON, K. R. MIKESKA, J. M. CHABALA, and R. LEVI-SETTI (1999) “Silica and magnesia dopant distributions in alumina by high-resolution scanning secondary ion mass spectrometry,” *Journal of the American Ceramic Society*, **82**(4), pp. 1001–1008.
- [3] FRUEH, T., E. KUPP, C. COMPSON, J. ATRIA, and G. MESSING (2016) “The effects of Na₂O and SiO₂ in liquid phase sintering of Bayer Al₂O₃,” *Journal of the American Ceramic Society*, **99**(7), pp. 2267–2272.
- [4] KANG, S. J. L. (2004) *Sintering*, Elsevier Butterworth-Heinemann, Oxford.
- [5] COBLE, R. L. (1962), “Transparent alumina and method of preparation,” .
- [6] ——— (1962) “Sintering alumina: effect of atmospheres,” *Journal of the American Ceramic Society*, **45**(3), pp. 123–127.
- [7] ——— (1961) “Sintering crystalline solids,” *Journal of applied physics*, **32**(5), pp. 787–799.
- [8] BENNISON, S. J. and M. P. HARMER (1990) “A history of the role of MgO in the sintering of α -Al₂O₃,” in *Ceramic Transactions 7, Sintering of Advanced Ceramics* (C. A. Handwerker, J. E. Blendell, and W. A. Kaysser, eds.), Am. Ceram. Soc., Westerville, pp. 13–49.
- [9] JORGENSEN, P. J. and J. H. WESTBROOK (1964) “Role of Solute Segregation at Grain Boundaries During Final-Stage Sintering of Alumina,” *Journal of the American Ceramic Society*, **47**(7), pp. 332–338.
- [10] JORGENSEN, P. J. (1965) “Modification of sintering kinetics by solute segregation in Al₂O₃,” *Journal of the American Ceramic Society*, **48**(4), pp. 207–210.

- [11] JOHNSON, W. C. and R. L. COBLE (1978) “A Test of the Second-Phase and Impurity-Segregation Models for MgO-Enhanced Densification of Sintered Alumina,” *Journal of the American Ceramic Society*, **61**(3-4), pp. 110–114.
- [12] HEUER, A. H. (1979) “The role of MgO in the sintering of alumina,” *Journal of the American Ceramic Society*, **62**, pp. 317–318.
- [13] BAE, S. I. and S. BAIK (1993) “Determination of critical concentrations of silica and/or calcia for abnormal grain growth in alumina,” *Journal of the American Ceramic Society*, **76**(4), pp. 1065–1067.
- [14] BAE, I.-J. and S. BAIK (1997) “Abnormal grain growth of alumina,” *Journal of the American Ceramic Society*, **56**, pp. 1149–1156.
- [15] BAE, S. I. and S. BAIK (1994) “Critical concentration of MgO for the prevention of abnormal grain growth in alumina,” *Journal of the American Ceramic Society*, **77**(10), pp. 2499–2504.
- [16] HANDWERKER, C. A., P. A. MORRIS, and R. L. COBLE (1989) “Effects of chemical inhomogeneities on grain growth and microstructure in Al_2O_3 ,” *Journal of the American Ceramic Society*, **72**(1), pp. 130–136.
- [17] HANSEN, S. C. and D. S. PHILLIPS (1983) “Grain boundary microstructures in a liquid-phase sintered alumina ($\alpha\text{-Al}_2\text{O}_3$),” *Philosophical Magazine A*, **47**(2), pp. 209–234.
- [18] HARMER, M. P. (1984) “Use of solid-solution additives in ceramic processing,” *Advances in ceramics*, **10**, p. 679.
- [19] BATEMAN, C. A., S. J. BENNISON, and M. P. HARMER (1989) “Mechanism for the role of magnesia in the sintering of alumina containing small amounts of a liquid phase,” *Journal of the American Ceramic Society*, **72**(7), pp. 1241–1244.
- [20] SONI, K. K., A. M. THOMPSON, M. P. HARMER, D. B. WILLIAMS, J. M. CHABALA, and R. LEVI-SETTI (1995) “Solute segregation to grain boundaries in MgO-doped alumina,” *Applied physics letters*, **66**(21), pp. 2795–2797.
- [21] BENNISON, S. J. and M. P. HARMER (1983) “Effect of MgO solute on the kinetics of grain growth in Al_2O_3 ,” *Journal of the American Ceramic Society*, **66**(5).
- [22] ROY, S. K. and R. L. COBLE (1968) “Solubilities of magnesia, titania, and magnesium titanate in aluminum oxide,” *Journal of the American Ceramic society*, **51**(1), pp. 1–6.

- [23] DILLON, S. J. and M. P. HARMER (2007) "Multiple grain boundary transitions in ceramics: a case study of alumina," *Acta Materialia*, **55**(15), pp. 5247–5254.
- [24] DILLON, S. J., M. P. HARMER, and G. S. ROHRER (2010) "Influence of interface energies on solute partitioning mechanisms in doped aluminas," *Acta Materialia*, **58**(15), pp. 5097–5108.
- [25] DILLON, S. J., M. TANG, W. C. CARTER, and M. P. HARMER (2007) "Complexion : A new concept for kinetic engineering in materials science," **55**, pp. 6208–6218.
- [26] CANTWELL, P. R., M. TANG, S. J. DILLON, J. LUO, G. S. ROHRER, and M. P. HARMER (2014) "Grain boundary complexions," *Acta Materialia*, **62**, pp. 1–48.
- [27] DILLON, S. J. and M. P. HARMER (2008) "Demystifying the role of sintering additives with "complexion"," *Journal of the European Ceramic Society*, **28**(7), pp. 1485–1493.
- [28] KANG, S.-J. L., M.-G. LEE, and S.-M. AN (2009) "Microstructural Evolution During Sintering with Control of the Interface Structure," *Journal of the American Ceramic Society*, **92**(7), pp. 1464–1471.
- [29] KANG, S.-J. L., S.-Y. KO, and S.-Y. MOON (2016) "Mixed control of boundary migration and the principle of microstructural evolution," *Journal of the Ceramic Society of Japan*, **124**(4), pp. 259–267.
- [30] JO, W., D.-Y. KIM, and N.-M. HWANG (2006) "Effect of Interface Structure on the Microstructural Evolution of Ceramics," *Journal of the American Ceramic Society*, **89**(8), pp. 2369–2380.
- [31] COMPSON, C., N. ROSENBERGER, and M. SPREIJ (2013) "The Effect of SiO₂ and Na₂O content on the Sintering Behavior of Calcined Specialty Aluminas for the Ceramics Industry," *CFI-Ceramic Forum International*, **90**(3), pp. E17–E22.
- [32] SUMITA, S. and H. K. BOWEN (1988) "Effects of foreign oxides on grain growth and densification of sintered Al₂O₃," *Ceramic Powder Science II. Transactions*, **1**, pp. 840–847.
- [33] SMOTHERS, W. J. and H. J. REYNOLDS (1954) "Sintering and grain growth of alumina," *Journal of the American Ceramic Society*, **37**(12), pp. 588–595.
- [34] CAHOON, H. P. and C. J. CHRISTENSEN (1956) "Sintering and Grain Growth of α -Alumina," *Journal of the American Ceramic Society*, **39**(10), pp. 337–344.

- [35] LOUET, N., M. GONON, and G. FANTOZZI (2005) "Influence of the amount of Na₂O and SiO₂ on the sintering behavior and on the microstructural evolution of a Bayer alumina powder," *Ceramics International*, **31**(7), pp. 981–987.
- [36] *ASTM B962-15, Standard test methods for density of compacted or sintered powder metallurgy (PM) products using Archimedes' principle, ASTM International, West Conshohocken, PA, 2015, www.astm.org.*
- [37] *ASTM E112-13, Standard test methods for determining average grain size, ASTM International, West Conshohocken, PA, 2013, www.astm.org.*
- [38] JUDD, M., B. PLUNKETT, and M. POPE (1974) "The thermal decomposition of calcium, sodium, silver and copper (II) acetates," *Journal of Thermal Analysis and Calorimetry*, **6**(5), pp. 555–563.
- [39] LAMBOTTE, G. and P. CHARTRAND (2013) "Thermodynamic modeling of the (Al₂O₃+Na₂O), (Al₂O₃+Na₂O+SiO₂), and (Al₂O₃+Na₂O+AlF₃+NaF) systems," *The Journal of Chemical Thermodynamics*, **57**, pp. 306–334.
- [40] BROWNMILLER, L. and R. BOGUE (1932) "System CaO-Na₂O-Al₂O₃," *Bureau of Standards Journal of Research*, **8**, pp. 289–307.
- [41] PABLO-GALAN, L. and W. R. FOSTER (1959) "Investigation of Role of Beta Alumina in the System Na₂O-Al₂O₃-SiO₂," *Journal of the American Ceramic Society*, **42**(10), pp. 491–498.
- [42] RANKIN, G. A. and H. E. MERWIN (1916) "THE TERNARY SYSTEM CaO-Al₂O₃-MgO." *Journal of the American Chemical Society*, **38**(3), pp. 568–588.
- [43] RIDGWAY, R. R., A. A. KLEIN, and W. J. O'LEARY (1936) "The Preparation and Properties of So-Called "Beta Alumina"," *Transactions of the Electrochemical Society*, **70**(1), pp. 71–88.
- [44] DUNCAN, J. H. and W. E. C. CREYKE (1969) "The formation and stability of β -Al₂O₃ in α -Al₂O₃ Ceramics," *Trans. Brit. Ceram. Soc.*, pp. 137–144.
- [45] SUTORIK, A. C., S. S. NEO, D. R. TREADWELL, and R. M. LAINE (1998) "Synthesis of Ultrafine β "-Alumina Powders via Flame Spray Pyrolysis of Polymeric Precursors," *Journal of the American Ceramic Society*, **81**(6), pp. 1477–1486.
- [46] STEVENS, R. and J. G. P. BINNER (1984) "Structure, properties and production of β -alumina," *Journal of materials science*, **19**(3), pp. 695–715.

- [47] CHRISTIE, J. R., A. J. DARNEll, and D. F. DUSTIN (1978) “Reaction of molten sodium carbonate with aluminum oxide,” *J. Phys. Chem.;(United States)*, **82**(1).
- [48] KUMMER, J. T. (1972) “Beta-alumina electrolytes,” in *Prog. Solid State Chemistry* (H. Reiss and J. O. McCaldin, eds.), 7 Pergamon Press, New York, pp. 141–175.
- [49] VRIES, R. C. and W. L. ROTH (1969) “Critical Evaluation of the Literature Data on Beta Alumina and Related Phases: I, Phase Equilibria and Characterization of Beta Alumina Phases,” *Journal of the American Ceramic Society*, **52**(7), pp. 364–369.
- [50] TERAI, R. and R. HAYAMI (1975) “Ionic diffusion in glasses,” *Journal of Non-Crystalline Solids*, **18**(2), pp. 217–264.
- [51] KWON, O.-H. and G. L. MESSING (1990) “Kinetic Analysis of Solution-Precipitation During Liquid-Phase Sintering of Alumina,” *Journal of the American Ceramic Society*, **73**(2), pp. 275–281.
- [52] ——— (1991) “A theoretical analysis of solution-precipitation controlled densification during liquid phase sintering,” *Acta metallurgica et materialia*, **39**(9), pp. 2059–2068.
- [53] PARK, C. W. and D. Y. YOON (2000) “Effects of SiO₂, CaO₂, and MgO additions on the grain growth of alumina,” *Journal of the American Ceramic Society*, **83**(10), pp. 2605–2609.
- [54] DAY, D. E. and G. E. RINDONE (1962) “Properties of soda aluminosilicate glasses: I, refractive index, density, molar refractivity, and infrared absorption spectra,” *Journal of the American Ceramic Society*, **45**(10), pp. 489–496.
- [55] WU, G., E. YAZHENSKIKH, K. HACK, and M. MÜLLER (2015) “Viscosity model for oxide melts relevant to fuel slags. Part 2: The system SiO₂-Al₂O₃-CaO-MgO-Na₂O-K₂O,” *Fuel Processing Technology*, **138**, pp. 520–533.
- [56] POPOVIC, A., L. BENCZE, J. KORUZA, B. MALIC, and M. KOSEC (2012) “Knudsen effusion mass spectrometric approach to the thermodynamics of Na₂O-Nb₂O₅ system,” *International Journal of Mass Spectrometry*, **309**, pp. 70–78.
- [57] GALLUP, J. (1935) “The transformation of aluminum oxide from the beta to the alpha form,” *Journal of the American Ceramic Society*, **18**(1-12), pp. 144–148.

- [58] BAE, S. I. and S. BAIK (1993) “Sintering and grain growth of ultrapure alumina,” *Journal of Materials Science*, **28**(15), pp. 4197–4204.
- [59] PARK, C. W. and D. Y. YOON (2000) “Grain growth of alumina,” **609**(3), pp. 2605–2609.
- [60] MAO, H., O. FABRICHNAYA, M. SELLEBY, and B. SUNDMAN (2005) “Thermodynamic assessment of the MgO-Al₂O₃-SiO₂ system,” *Journal of Materials Research*, **20**(04), pp. 975–986.
- [61] SHANG, S., Y. WANG, D. KIM, and Z.-K. LIU (2010) “First-principles thermodynamics from phonon and Debye model: Application to Ni and Ni₃Al,” *Computational Materials Science*, **47**(4), pp. 1040–1048.
- [62] WANG, Y., Z.-K. LIU, and L.-Q. CHEN (2004) “Thermodynamic properties of Al, Ni, NiAl, and Ni₃Al from first-principles calculations,” *Acta Materialia*, **52**(9), pp. 2665–2671.
- [63] LIU, X. L., B. K. VANLEEUWEN, S. SHANG, Y. DU, and Z.-K. LIU (2015) “On the scaling factor in Debye-Grüneisen model: A case study of the Mg-Zn binary system,” *Computational Materials Science*, **98**, pp. 34–41.
- [64] SHANG, S., Y. WANG, and Z.-K. LIU (2007) “First-principles elastic constants of α - and θ -Al₂O₃,” *Applied Physics Letters*, **90**(10), pp. 101909–1–101909–3.
- [65] KRESSE, G. and J. FURTHMÜLLER (1996) “Efficiency of ab-initio total energy calculations for metals and semiconductors using a plane-wave basis set,” *Computational Materials Science*, **6**(1), pp. 15–50.
- [66] KRESSE, G. and D. JOUBERT (1999) “From ultrasoft pseudopotentials to the projector augmented-wave method,” *Physical Review B*, **59**(3), pp. 1758–1775.
- [67] BLÖCHL, P. (1994) “Projector augmented-wave method,” *Physical Review B*, **50**(24), p. 17953.
- [68] PERDEW, J. and Y. WANG (1992) “Accurate and simple analytic representation of the electron-gas correlation energy,” *Physical Review B*, **45**(23), p. 13244.
- [69] MONKHORST, H. and J. PACK (1976) “Special points for Brillouin-zone integrations,” *Physical Review B*, **13**(12), pp. 5188–5192.
- [70] ATKINSON, K. J. W., R. W. GRIMES, M. R. LEVY, Z. L. COULL, and T. ENGLISH (2003) “Accommodation of impurities in α -Al₂O₃, α -Cr₂O₃ and α -Fe₂O₃,” *Journal of the European Ceramic Society*, **23**(16), pp. 3059–3070.

- [71] GRIMES, R. W. (1994) “Solution of MgO, CaO, and TiO₂ in α -Al₂O₃,” *Journal of the American Ceramic Society*, **77**(2), pp. 378–384.
- [72] LAGERLÖF, K. P. D. and R. W. GRIMES (1998) “The defect chemistry of sapphire (α -Al₂O₃),” *Acta materialia*, **46**(16), pp. 5689–5700.
- [73] XIANG, X., G. ZHANG, X. WANG, T. TANG, and Y. SHI (2015) “A new perspective on the process of intrinsic point defects in α -Al₂O₃,” *Physical Chemistry Chemical Physics*, **17**(43), pp. 29134–29141.
- [74] SARSAM, J., M. W. FINNIS, and P. TANGNEY (2013) “Atomistic force field for alumina fit to density functional theory,” *The Journal of chemical physics*, **139**(20), p. 204704.
- [75] SUBRAMANIAM, A., C. T. KOCH, R. M. CANNON, and M. RÜHLE (2006) “Intergranular glassy films: An overview,” *Materials Science and Engineering A*, **422**(1-2), pp. 3–18.
- [76] LOUET, N., H. REVERON, and G. FANTOZZI (2008) “Sintering behaviour and microstructural evolution of ultrapure α -alumina containing low amounts of SiO₂,” **28**, pp. 205–215.
- [77] JAIN, A., S. ONG, G. HAUTIER, W. CHEN, W. RICHARDS, S. DACEK, S. CHOLIA, D. GUNTER, D. SKINNER, and G. CEDER (2013) “The Materials Project: A materials genome approach to accelerating materials innovation,” *Apl Materials*, **1**(1), p. 11002.
- [78] “Materials Project,” .
URL <http://www.materialsproject.org>
- [79] GRAHAM, J. (1960) “Lattice spacings and colour in the system alumina - chromic oxide,” *Journal of Physics and Chemistry of Solids*, **12**, pp. 349–350.
- [80] BERGERHOFF, G., R. HUNDT, R. SIEVERS, and I. D. BROWN (1983) “The inorganic crystal structure data base,” *Journal of Chemical Information and Computer Sciences*, **23**(2), pp. 66–69.
- [81] KARLSRUHE, F. I. Z., “Inorganic Crystal Structure Database,” .
- [82] RAGHAVAN, V. (2010) “Al-Fe-O (Aluminum-iron-oxygen),” *Journal of Phase Equilibria and Diffusion*, **31**(4), p. 367.
- [83] CLARKE, D. R., T. M. SHAW, A. P. PHILIPSE, and R. G. HORN (1993) “Possible electrical double-layer contribution to the equilibrium thickness of intergranular glass films in polycrystalline ceramics,” *Journal of the American Ceramic Society*, **76**(5), pp. 1201–1204.

- [84] CLARKE, D. R. (1987) “On the equilibrium thickness of intergranular glass phases in ceramic materials,” *Journal of the American Ceramic Society*, **70**(1), pp. 15–22.
- [85] KINGERY, W. D. (2004) “Densification during sintering in the presence of a liquid phase. I. Theory,” *Journal of Applied Physics*, **30** (1959).
- [86] LEE, S.-M. and S.-J. L. KANG (1998) “Theoretical analysis of liquid-phase sintering: Pore filling theory,” *Acta Materialia*, **46**(9), pp. 3191–3202.
- [87] SHAW, T. M. (1986) “Liquid redistribution during liquid-phase sintering,” *Journal of the American Ceramic Society*, **69**(1), pp. 27–34.
- [88] SVOBODA, J., H. RIEDEL, and R. GAEBEL (1996) “A model for liquid phase sintering,” *Acta Materialia*, **44**(8), pp. 3215–3226.
- [89] GERMAN, R. M. (2016) “Sintering trajectories: Description on how density, surface area, and grain size change,” *JOM*, **68**(3), pp. 878–884.
- [90] ISRAELACHVILI, J. (2011) *Intermolecular and Surface Forces*.
- [91] HSIEH, C., H. JAIN, and E. I. KAMITSOS (1996) “Correlation between dielectric constant and chemical structure of sodium silicate glasses,” *Journal of Applied Physics*, **80**(3), pp. 1704–1712.
- [92] LYON, K. (1942) “Calculation of surface tensions of glasses,” *Journal of The American Ceramic Society*, **27**(6), pp. 25–28.
- [93] ZHANG, S. and S. H. GAROFALINI (2005) “Molecular dynamics computer simulations of the interface structure of calcium-alumino-silicate intergranular films between combined basal and prism planes of $\alpha\text{-Al}_2\text{O}_3$,” *Journal of the American Ceramic Society*, **88**(1), pp. 202–209.
- [94] TANAKA, I., H.-J. KLEEBE, M. K. CINIBULK, J. BRULEY, D. R. CLARKE, and M. RÜHLE (1993) “Calcium concentration dependence of the intergranular film thickness in silicon nitride,” *Journal of the American Ceramic Society*, **77**(4), pp. 911–914.
- [95] TOPLIS, M. J., D. B. DINGWELL, and T. LENCI (1997) “Peraluminous viscosity maxima in Na_2O Al_2O_3 SiO_2 liquids: The role of triclusters in tectosilicate melts,” *Geochimica et Cosmochimica Acta*, **61**(13), pp. 2605–2612.
- [96] LITTON, D. A. and S. H. GAROFALINI (1999) “Atomistic structure of sodium and calcium silicate intergranular films in alumina,” *Journal of Materials Research*, **14**(4), pp. 1418–1429.

- [97] CINIBULK, M. (1995) "Thermal stability of some hexaluminates at 1400°C," *Journal of Materials Science Letters*, **14**, pp. 651–654.
- [98] STILLWELL, C. V. (1926) "The Color of the Ruby," *J. Phys. Chem.*, **30**, pp. 1441–1466.
- [99] RAY, A. K. and E. C. SUBBARAO (1975) "Synthesis of sodium beta and beta" alumina," **10**(6), pp. 583–590.
- [100] UNDERWOOD, E. E. (1972) "The Mathematical Foundations of Quantitative Stereology," in *Stereology and Quantitative Metallography* (G. Pellissier and S. Purdy, eds.), ASTM International, West Conshohocken, pp. 3–38.
- [101] SU, H. and D. L. JOHNSON (1996) "Master Sintering Curve: a practical approach to sintering," *Journal of American Ceramics Society*, **79**(12), pp. 3211 – 3217.
- [102] HANSEN, J. D., R. P. RUSIN, M.-H. TENG, and D. L. JOHNSON (1992) "Combined-Stage Sintering Model," *Journal of the American Ceramic Society*, **75**(5), pp. 1129–1135.
- [103] PARK, S. J., J. M. MARTIN, J. F. GUO, J. L. JOHNSON, and R. M. GERMAN (2006) "Grain Growth Behavior of Tungsten Heavy Alloys Based on the Master Sintering Curve Concept," *Metallurgical and Materials Transactions A*, **37**, pp. 9–16.
- [104] DIANTONIO, C. B., K. G. EWSUK, and D. BENCOE (2005) "Extension of Master Sintering Curve Theory to Organic Decomposition," *Journal of the American Ceramics Society*, **2728**, pp. 2722–2728.
- [105] AGGARWAL, G., S.-J. PARK, I. V. I. SMID, and R. M. GERMAN (2007) "Master Decomposition Curve for Binders Used in Powder Injection Molding," *Metallurgical and Materials Transactions A*, pp. 606–614.
- [106] BLAINE, D. C., S. J. PARK, P. SURI, and R. M. GERMAN (2006) "Application of work-of-sintering concepts in powder metals," *Metallurgical and Materials Transactions A: Physical Metallurgy and Materials Science*, **37**(9), pp. 2827–2835.
- [107] TATAMI, J., Y. SUZUKI, T. WAKIHARA, T. MEGURO, and K. KOMEYA (2006) "Control of Shrinkage during Sintering of Alumina Ceramics Based on Master Sintering Curve Theory," *Key Engineering Materials*, **317-318**, pp. 11–14.
- [108] POUCHLY, V. and K. MACA (2009) "Master sintering curves of two different alumina powder compacts," *Processing and Application of Ceramics*, **3**(4), pp. 177–180.

- [109] AMINZARE, M., F. GOLESTANI-FARD, O. GUILLON, M. MAZAHERI, and H. R. REZAIE (2010) “Sintering behavior of an ultrafine alumina powder shaped by pressure filtration and dry pressing,” *Materials Science and Engineering A*, **527**(16-17), pp. 3807–3812.
- [110] GUILLON, O. and J. LANGER (2010) “Master sintering curve applied to the Field-Assisted Sintering Technique,” *Journal of Materials Science*, **45**(19), pp. 5191–5195.
- [111] SHAO, W. Q., S. O. CHEN, D. LI, H. S. CAO, Y. C. ZHANG, and S. S. ZHANG (2009) “Prediction and control of microstructure evolution for sub-microscale α -Al₂O₃ during low-heating-rate sintering based on the master sintering curve theory,” *Journal of the European Ceramic Society*, **29**(1), pp. 201–204.
- [112] HARMER, M. P. and R. J. BROOK (1981) “Fast firing - Microstructural benefits,” *Trans. Brit. Ceram. Soc.*, **80**, p. 147.
- [113] WANG, S.-Y. and M.-H. TENG (2010) “Why a master sintering curve model can be applied to the sintering of nano-sized particles ?” *Journal of Alloys and Compounds*, **504**, pp. S336–S339.
- [114] REITERER, M. W. and K. G. EWSUK (2009) “An Analysis of Four Different Approaches to Predict and Control Sintering,” *Journal of the American Ceramic Society*, **92**, pp. 1419–1426.
- [115] MACA, K., V. POUCHLÝ, K. BODIŠOVÁ, P. ŠVANČÁREK, and D. GALUSEK (2014) “Densification of fine-grained alumina ceramics doped by magnesia, yttria and zirconia evaluated by two different sintering models,” *Journal of the European Ceramic Society*, **34**(16), pp. 4363–4372.
- [116] KINGERY, W. D., P. B. VANDIVER, I.-W. HUANG, and Y.-M. CHIANG (1983) “Liquid-liquid immiscibility and phase separation in the quaternary systems Ka₂O-Al₂O₃-CaO-SiO₂ and Na₂O-Al₂O₃-CaO-SiO₂,” *Journal of Non-Crystalline Solids*, **54**, pp. 163–171.
- [117] CANTWELL, P. R., S. MA, S. A. BOJARSKI, G. S. ROHRER, and M. P. HARMER (2016) “Expanding time temperature-transformation (TTT) diagrams to interfaces: A new approach for grain boundary engineering,” *Acta Materialia*, **106**, pp. 78–86.

Vita

Tobias Frueh

Tobias Frueh was born in Ellwangen/Jagst, Germany in 1990 and was raised in Ammelbruch, Germany. Tobias received his Bachelor of Science degree in Nanoscience and Technology in May 2013 and his Master of Science degree in Materials Science and Engineering in January 2015, both from the University of Erlangen-Nuremberg, Germany. During his Masters education, he studied for one year at The Pennsylvania State University, USA to conduct the research for his Masters Thesis and was co-advised by Professor Andreas Roosen and Professor Gary Messing. After completing his Mater of Science degree Tobias continued his graduate studies at The Pennsylvania State University and was advised by Professor Gary L. Messing. After graduation, Tobias joined Almatis GmbH in Ludwigshafen, Germany as Application and Market Development Engineer.

List of Publications:

- Tobias Frueh, Elizabeth R. Kupp, Charles Compson, Joe Atria, Nils Rosenberger and Gary L. Messing, "Modal interpretation of Sintering Kinetics Based on Dilatometry," chi/Ber. DKG, 92, E1-4 (2015).
- Tobias Frueh, Elizabeth R. Kupp, Charles Compson, Joe Atria and Gary L. Messing, "The Effect of Na₂O and SiO₂ on Liquid Phase Sintering of Bayer Al₂O₃," J. Am. Ceram. Soc., 99, 2267-2272 (2016).
- Gary L. Messing, Stephen Poterala, Yunfei Chang, Tobias Frueh, Elizabeth R. Kupp, Beecher H. Watson III, Rebecca L. Walton, Michael J. Brova, Anna-Katharina Hofer, Raul Bermejo, Richard J. Meyer, "Texture-engineered ceramics - Property enhancements through crystallographic tailoring" Journal of Materials Research, <https://doi.org/10.1557/jmr.2017.207> (2017).
- Tobias Frueh, Cassie Marker, Elizabeth R. Kupp, Charles Compson, Joe Atria, Jennifer L. Gray, Zi-Kui Liu, and Gary L. Messing, "Powder Chemistry Effects on the Sintering of MgO-doped Specialty Al₂O₃," accepted in J. Am. Ceram. Soc.
- Tobias Frueh, I. O. Ozer, S. F. Poterala, Elizabeth R. Kupp, Charles Compson, Joe Atria and Gary L. Messing, "A Critique of Master Sintering Curve Analysis of Sintering Processes," submitted for publication.
- Tobias Frueh, Elizabeth R. Kupp, Charles Compson, Joe Atria, and Gary L. Messing, "Dynamic development of nanometer scale grain boundaries during liquid phase sintering," preparing for submission.

- Tobias Frueh, Elizabeth R. Kupp, Charles Compson, Joe Atria, and Gary L. Messing, "Second phase formation in Bayer alumina," preparing for submission.